A COMPREHENSIVE STUDY ON A HEATSINK SUBJECTED TO AN AIRFLOW UTILIZING SHEAR STRESS TRANSPORT MODEL USING SU2, M.A.SC

by

SAMANEH JOUDAKI

THESIS PRESENTED TO ÉCOLE DE TECHNOLOGIE SUPÉRIEURE IN PARTIAL FULFILLMENT FOR A MASTER'S DEGREE WITH THESIS IN MECHANICAL ENGINEERING
M.A.SC.

MONTREAL, JUNE 22 2025

ÉCOLE DE TECHNOLOGIE SUPÉRIEURE
UNIVERSITÉ DU QUÉBEC

BOARD OF EXAMINERS (THESIS M.SC.A.)

THIS THESIS HAS BEEN EVALUATED

BY THE FOLLOWING BOARD OF EXAMINERS

Mr. François Morency, Thesis Supervisor
Département de génie mécanique at École de technologie supérieure

Mr. François Garnier, President of the Board of Examiners
Département de génie mécanique at École de technologie supérieure

Mr. Jesus David Gonzalez Llorente, Member of the jury
Département de génie aérospatial at École de technologie supérieure

THIS THESIS WAS PRENSENTED AND DEFENDED

IN THE PRESENCE OF A BOARD OF EXAMINERS AND PUBLIC

JUNE 10, 2025

AT ÉCOLE DE TECHNOLOGIE SUPÉRIEURE

ACKNOWLEDGMENT

I would like to express my deepest gratitude to my supervisor, Prof. François Morency, for his guidance, encouragement, and expertise throughout my research journey. His invaluable support and insights have been instrumental in shaping my understanding and approach to the field of computational fluid dynamics and heat transfer, and I am profoundly grateful for his mentorship.

I would also like to thank the École de technologie supérieure (ÉTS) for providing a stimulating academic environment and the necessary resources to pursue my research.

My heartfelt thanks go to my family – my parents for their unwavering support, both emotional and financial, and to my sister, whose encouragement has been a source of strength during the most challenging times. Their belief in my potential has been a constant motivator and a reminder of the importance of persistence and dedication.

Lastly, I wish to acknowledge Alliance Canada for their technical support, which has greatly contributed to the advancement of my research. Their commitment to academic research is truly commendable.

Thank you all for your invaluable support and encouragement throughout this journey.

UNE ETUDE COMPLÈTE SUR UN DISSIPATEUR THERMIQUE SOUMIS À UN FLUX D'AIR UTILISANT UN MODÈLE DE TRANSPORT DE CONTRAINTE DE CISAILLEMENT UTILISANT SU2

Samaneh JOUDAKI

RESUME

La présente étude utilise le modèle de transport des contraintes de cisaillement (SST) pour prévoir l'écoulement de fluide et le transfert de chaleur tout en fournissant un examen détaillé d'un dissipateur thermique exposé à un flux d'air. Éléments essentiels du refroidissement électronique, les dissipateurs thermiques sont conçus pour disperser la chaleur produite par l'électronique afin d'éviter la surchauffe et de garantir un fonctionnement optimal. L'objectif de cette étude est d'analyser l'effet de la vitesse, de la température et des caractéristiques d'écoulement qui ont un effet substantiel sur les performances des dissipateurs thermiques.

Connu pour sa capacité à prédire avec précision le transfert de chaleur et la séparation des flux dans les couches limites turbulentes, le modèle de transport des contraintes de cisaillement (SST) est utilisé pour représenter les relations complexes entre les surfaces du dissipateur thermique et le flux d'air. Ce modèle est particulièrement bien adapté pour imiter les zones turbulentes produites par la structure des ailettes circulaires du dissipateur thermique et pour capturer les subtilités des zones d'écoulement connectées et séparées, toutes deux importantes pour la dissipation de la chaleur.

L'étude examine différentes caractéristiques telles que la vitesse et la température. Pour effectuer une comparaison approfondie entre différentes configurations, des caractéristiques de performance clés telles que la résistance thermique, les coefficients de transfert de chaleur et les chutes de pression sont évaluées. De plus, des recherches sur la sensibilité de la grille sont menées pour évaluer la précision et la fiabilité des résultats. Les résultats démontrent à quel point les modèles de turbulence SST et Spalart-Allmaras peuvent représenter les gradients thermiques localisés et les caractéristiques d'écoulement. Les programmes open source SU2 et Paraview ont été utilisés pour mener l'étude. Cette étude fournie un cadre pour choisir des configurations de dissipateurs qui minimisent les pertes de pression et réduisent la résistance thermique.

Mots-clés : CFD, dissipateur thermique, modèle de transport de contrainte de cisaillement (SST), modélisation de la turbulence, gestion thermique, dissipation thermique, sensibilité de la grille, refroidissement électronique, SU2

A COMPREHENSIVE STUDY ON A HEATSINK SUBJECTED TO AN AIRFLOW UTILIZING SHEAR STRESS TRANSPORT MODEL USING SU2

SAMANEH JOUDAKI

ABSTRACT

Essential parts of electronic cooling, heatsinks are made to disperse heat produced by electronics to avoid overheating and guarantee safe operation. Optimizing a heartsink's design and increasing its efficiency requires an understanding of the complex thermal and flow properties surrounding it. The objective of this study is to analyze the effect of velocity, temperature, and flow characteristics that have a substantial effect on the performance of heat sinks.

The present study uses the Shear Stress Transport (SST) model to forecast fluid and thermal flow while providing a detailed examination of a heatsink exposed to airflow. Known for its ability to precisely predict heat transfer and flow separation in turbulent boundary layers, the Shear Stress Transport (SST) model is used to represent the relationships between pin-fin heatsink surfaces and airflow. This model is especially well-suited to mimic the turbulent areas produced by the fin structure of the heatsink and to capture the subtleties of both connected and separated flow zones, both of which are important for heat dissipation.

The study reviews different characteristics of heatsink such as flow rate and temperature. Effect of different flow criteria: inlet velocity, temperature are studied. To give a thorough comparison across various configurations, key performance characteristics: heat transfer coefficients, and pressure drops, thermal resistance are assessed. The study starts with a grid sensitivity conducted to evaluate the precision and dependability of the findings. The results demonstrate that the SST and Spalart-Allmaras turbulence models can represent localized thermal gradients and flow characteristics. By comparing different turbulence models, the paper demonstrates how dependent pressure drop and thermal performance estimates are on turbulence modelling assumptions. The open-source programs SU2 CFD and Paraview were used to conduct the study. This study provide a framework for choosing layouts that minimize pressure losses and optimize thermal efficiency.

Keywords: CFD, heatsink, Shear Stress Transport (SST) model, turbulence modeling, thermal management, heat dissipation, pressure drop, thermal resistance, grid sensitivity, electronic cooling, SU2

TABLE OF CONTENTS

Page

LIST OF TABLES

Page

LIST OF FIGURES

Page

LIST OF SYMBOLS

k	Turbulent kinetic energy
ω	Specific dissipation rate
Γ	Preconditioning matrix
$\bar{v}$	Flow velocity vector
p	Pressure
T	Temperature
$\bar{F}^c$	Convective flux
$\bar{F}^v$	Viscous flux
ρ	Density
$\bar{I}$	Identity matrix
$\bar{\tau}$	Viscous stress tensor
k_a	Effective thermal conductivity
P_o	Thermodynamic Pressure
μ_d	Dynamic viscosity
Pr_d	Prandtl number
Pr_t	Turbulent Prandtl number
μ_a	Effective viscosity
ρ_s	Solid density
c_{ps}	Specific heat of the solid
k_s	Thermal conductivity
Q	Heat dissipation

A_{hs}	The total heat transfer area
T_{hs}	The temperature at the heat sink base
T_{in}	The temperature at the wind tunnel inlet
R_{th}	Thermal resistance
Δp^*	Dimensionless pressure drops
ΔP	Pressure drops
y^+	Distance from the wall
ν	Kinematic viscosity
u_τ	Friction velocity
τ_ω	Wall shear stress
c_f	Friction coefficient
V_{ref}	reference velocity
Re	Reynolds number
D	Nozzle diameter
μ_j	Dynamic viscosity
d	Diameter
n	Number of elements
$\Delta\theta$	Angle difference
. n_c	Number of the nodes on Cylinder
Nu	Nusselt Number

INTRODUCTION

The importance of electronic devices in today's world is undeniable; virtually, every daily or professional task can be accomplished more efficiently using smart devices. As these devices are continually updated, their maintenance and efficiency must be studied from various perspectives. One of the most critical components of these devices is their cooling systems and heat dissipation mechanisms. While many parts contribute to the optimal functioning of these devices, the heat transfer component is arguably one of the most vital, and in some cases, the most crucial part of the system (Bhattacharyya, Vishwakarma, Roy, Biswas, & Ardekani, 2020). Proper management of heat dissipation is essential to ensure the longevity and performance of electronic devices, as excessive heat can lead to reduced efficiency, hardware damage, and system failure. Various methods, such as cooling pipes, fans, specialized circuit boards, and heatsinks, can be employed to reduce the heat of CPUs and electronic systems. Among these methods, heatsinks are particularly popular in the industry(Arshad, Ali, Yan, Hussein, & Ahmadlouydarab, 2018 ; Cartagenas, 2021). Many companies prefer heatsinks over other cooling options for their designs. Each characteristic plays an important role in the efficiency of heatsinks. The material of the heatsink, which can be metals such as copper or aluminum, graphite foam or a composite of different materials, significantly impacts its performance(Coursey et al.,2005)(Gallego & Klett, 2003). Each of these materials can be employed in different scenarios based on the design requirements and needs of the system.

Regarding the shape of the heatsinks, the most significant aspect is the fins (Jaffal, 2017). Although some perforated heatsinks do not require fins, the majority do. These fins can vary in shape and height and can be positioned at different intervals on the base plate of the heatsinks. Regarding the geometrical measurements, different dimensions for the base plates can be selected based on the system size and thermal performance goals.

When it comes to heatsinks, another important factor to consider is the inlet and outlet flow. While many designers prefer water cooling to cool down their systems, airflow remains one of the most common options in the industry (Bonnie, 2015 ; F. Wang, Lai, Huang, & Huang, 2013). Whether utilizing natural convection or employing a fan to create forced air movement,

the positioning of the inlet and outlet is a critical characteristic of heatsink design. The inlet air can be directed either parallel to or impinging upon the fins. The efficiency of each configuration can vary; while many designers prefer parallel flow, others implement impinging flow in their systems. The choice between these airflow patterns depends on the specific thermal management requirements and the design constraints of the system.

When a heatsink is employed in a system to improve thermal performance and optimize the overall efficiency, each of the characteristics should be studied individually as well as collectively. Many design constraints need to be explored while designing and manufacturing a heatsink such as: induced approach velocity, available pressure drop, amount of required heat dissipation, etc. (Lee, 1995).

In the academic field, researchers and engineers have investigated heatsinks through both experimental and numerical methods. In experimental studies, researchers have utilized various types of heatsinks with differing shapes and materials to examine the effects of each variable(Liang & Hung, 2010) (Yin et al., 2008). They have also investigated the impact of inlet and outlet airflow configurations in some cases. Numerical researchers have employed different computational methods to analyze heatsink characteristics, studying criteria such as pressure drop, thermal resistance, and the Nusselt number for various Reynolds numbers (Vasilev, Abiev, & Kumar, 2021) (Sikka, Torrance, Scholler, & Salanova, 2000). Additionally, studies have combined both experimental and numerical approaches to comprehensively investigate and enhance heatsink performance (Alpsan, 2008) (Qu & Mudawar, 2002).

Computational Fluid Dynamics (CFD) is a major numerical field used to study thermal conductivity and thermal performance. Various numerical models can be employed to analyze and enhance test cases. One of the most used models in CFD is the Reynolds-Averaged Navier–Stokes (RANS) approach, which has been adopted for decades. Menter's Shear Stress Transport (SST) turbulence model, introduced by Menter in 1994 (F. R. Menter, 1994), has gained significant popularity among CFD researchers for its accuracy in predicting turbulent flows.

Although heatsinks are widely utilized in the industry, a lack of comprehensive data can still be observed in several aspects despite previous studies. For instance, while there is extensive

research on the characteristics of heatsinks, the importance of airflow requires further investigation and effort. Moreover, in many cases, researchers have defined their models assuming laminar airflow (Chai, Xia, & Wang, 2016a) (Xie, Liu, He, & Tao, 2009) (Chai, Xia, & Wang, 2016b) , though turbulent flow can significantly influence results and lead to different outcomes. Computational studies can play a pivotal role in advancing our knowledge in this area, providing detailed insights and enhancing the overall understanding of thermal management in electronic systems.

The objective of this study is to systematically discover and analyze the key elements: velocity, temperature and flow characteristics that have a substantial effect on the performance of heatsinks. Heatsinks elements including fin geometry, material choice, and airflow dynamics, and the review will involve an examination of previous research that utilized both experimental and numerical approaches. Furthermore, the study will analyze flow parameters including Pressure coefficient, Nusselt Number, Thermal resistance and Pressure drop utilizing CFD methods for different meshes. Focus is given on determining the sensitivity of pressure drop and heat transfer findings to turbulence choices, particularly when comparing the SST and Spalart-Allmaras models. The obtained results will be validated by the results of earlier studies to gain valuable insights that will guide the creation and verification of a new optimization model for heatsink design. The first chapter of the work is dedicated to previous studies on heatsinks and their characteristics, covering aspects such as material selection, fin design, and dimensional measurements. The second chapter focuses on methodology of the study. Defining the case studies, detailing the case study measurements, mathematical model, computational domain and utilized tools. The third chapter, shows and analyzes the obtained results for different meshes from coarse to fine for different Reynolds= 4000, 6000, 7000, 10000, 12400, 23000 number from the suggested test cases and validate the results with literature. The Final chapter is a conclusion of the work and future research plan.

CHAPTER 1

Literature Review

This chapter concentrates on the previous research work of the fellow scholar. In this chapter the heatsinks characteristics: material, dimension, geometry, flow position in experimental and numerical studies will be reviewed. The review and the articles are chosen based on the most effective parameters of the heatsink for their design. The computational method and model were important criteria in the choice of numerical works. The quality of the article based on the publishing information was also considered. Specific keywords: heatsink, flow characteristics, CFD, Pin Fin were utilized.

Electronic devices' durability, dependability, and performance all depend on effective thermal management. It has grown increasingly difficult to dissipate excess heat as electronic components get smaller and more powerful. Because of their simplicity and efficiency, heatsinks continue to be one of the most popular options among the different techniques used for heat dissipation. Numerous elements, including as material characteristics, fin shape, and airflow dynamics, affect heatsink performance and design. These elements are all essential for maximizing heat transfer. To increase heatsink efficiency and guarantee the correct operation of electrical gadgets, it is imperative to comprehend these elements. This literature review will explore the main characteristics of heatsinks, including material choice, fin design, and airflow behavior, while critically evaluating the contribution of CFD and turbulence modeling in refining heatsink design.

The selection of materials for heatsinks is influencing their thermal efficiency. Copper and aluminum are typically preferred due to their excellent thermal conductivity, although alternative materials such as graphite foam and composites have been investigated for certain applications. Furthermore, the design characteristics of the heatsink fins, including their design, height, and layout, can greatly affect the dissipation of heat. While both material and design are vital, the setup of the incoming and outgoing airflow around the heatsink is also

crucial. The airflow, whether it is passive or actively forced, can be set parallel to the fins or hitting them directly, and this choice of setup can significantly affect the heat transfer effectiveness.

In recent years, Computational Fluid Dynamics (CFD) has emerged as a crucial tool for analyzing and enhancing heatsinks, specifically for simulating airflow and heat transfer under intricate conditions. The Reynolds-Averaged Navier–Stokes (RANS) equations, combined with the Shear Stress Transport (SST) turbulence model, have been widely utilized to model turbulent flows around heatsinks. Although much of the existing work has concentrated on laminar flow assumptions, turbulent flow frequently occurs in practical applications and can considerably influence heatsink performance.

1.1 Heatsink Characteristics

A heatsink serves as a thermal management tool in electronic systems, designed to disperse heat produced by components like CPUs, GPUs, or power transistors. It usually consists of a base plate that directly contacts the heat source and an array of fins that expand the available surface area for heat transfer to the surrounding air (Figure 1.1). A fin in a heatsink is an expanded surface that increases the area open to heat dissipation and is often constructed of conductive materials such as aluminium or copper. Fins assist transport heat from the heatsink's base to the surrounding environment, increasing cooling effectiveness via convection. Perforation is the purposeful creation of holes or apertures in fins to alter airflow patterns and improve heat transfer by enhancing turbulence and decreasing thermal boundary layers. Optimizing the size, shape, and distribution of these holes can boost thermal performance while potentially lowering material costs and weight. Heatsinks are often constructed from materials with high thermal conductivity to effectively conduct heat away from the electronic component and aid in its dissipation into the air (Kepekci & Asma, 2020). The most significant parameters concerning heatsinks include material, surface area, fin design, and inlet and outlet airflow configuration. Figure 1-1 shows a schematic of a Finned heatsink (Y. Wang & Ding, 2008). the Figure shows the surface area including the fin area and the base area, inlet and outlet flow direction and the position of the heatsink compared to the electronic component.

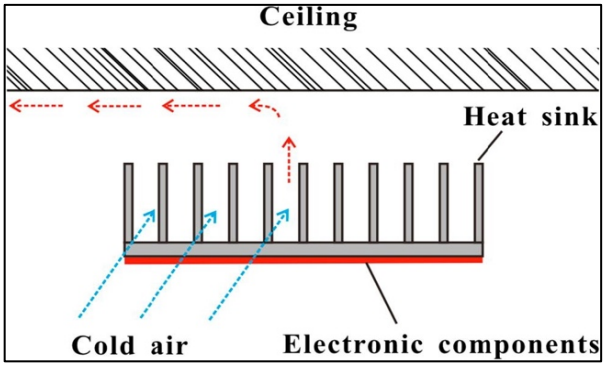

Figure 1.1 Schematic of a Finned heatsink
under a ceiling with a gap between the
heatsink and ceiling
Taken from Y. Wang & Ding (2008)

1.1.1 Materials

The material of the heatsink has been the subject of many studies (Kepekci & Asma, 2020) (You, 2015) (X.-Q. Wang, Yap, & Mujumdar, 2008). A heatsink's material choice should take at least four factors into account. The choice with the maximum heat conductivity is the most preferable, while when selecting an alternative, other factors like the material's cost and availability in the market should be considered.

In the 1980s, heatsinks gained popularity among researchers and designers in the electronics industry because of their efficiency. In 1988, Richard J Phillips (Phillips, 1988) experimented to compare the efficiency of the microchannel heatsinks with other electro-cooling techniques that were in use at the time. They carried out their experiments to design the heatsinks using materials like Indium Phosphate (InP) and aluminum. Copper was also utilized by them in part of their study. Different situations of thermal conductivity were examined for airflows and water flows. Compared to other methods of cooling microelectronic devices, the thermal performance of microchannel heat sinks is around two orders of magnitude greater. Although InP microchannel heat sinks had great thermal performance, aluminum was also a good material to use for mass manufacturing regarding the fabrication process (Phillips, 1988).

A team of scientists from Japan tried to create an original air-cooling heatsink for a high-density computer system in 1990. Takada et al. (1990) and their team experimented with several kinds of pin fins and surface perforation using Copper (Cu) as the foundation material for their fins and surface plate. Qu et al. (2000) and their team conducted an experimental investigation to contrast their experiment's results with the available numerical prediction. They created a microchannel heatsink for their experimental setup constructed of silicon with a trapezoid channel shape. They used water flow for cooling their system. While the experimental results demonstrated a lower Nusselt number compared to the expected amount from the numerical method, they could cover the numerical predictions with specific modifications to the relations (Qu, Mala, & Li, 2000).

Cuta et al. (1995) from the Pacific Northwest Laboratory, fabricated and tested 2 microchannel heatsinks. One of these test cases was made of a silicon substrate and the second model was made of copper substrate. While the number of channels was different in each model, distilled water was the working fluid in both cases. The silicon model was not used in some parts of the experiment due to the fragility of the test articles. They concluded material of the heatsink is important since it affects the thermal conductivity of the item (Cuta et al., 1995).

Zhang et al. (2004) examined silicon-based microchannel heatsinks for a range of experimental situations and analyzed the benefits, drawbacks, and limits of this kind of heatsink in the thermoelectric cooling process. Because of its heat conductivity, copper may be an excellent material even if it may be costly for the producer. The lotus-type porous copper is an ideal option for a heat sink because as the diameter of the pore decreases the thermal conductivity increases (Chiba, Ogushi, Nakajima, & Ikeda, 2004). Kumar et al. (2018) compared three microchannel heatsinks made from copper, silicon, and aluminum numerically. While the temperature rise for the coolant was the highest for the silicon model, the copper design was the second best in this category (Kumar et al., 2018). Lei et al. (2006) conducted an experimental and numerical study focusing on copper mini channel heatsinks. The effect of multilayering the heatsink was investigated during the research. Brendel et al. (2004) attempted to enhance the conductivity of heatsink material by creating a multi-phase fibre composed of silicon and copper, adding titanium as an interlayer.

Aluminum has been an ideal option for companies and researchers in designing heatsinks (Keller, 1998). Although it may not possess the highest thermal conductivity compared to other materials such as copper, aluminum is more cost-effective and readily available in the market. Its combination of adequate thermal performance, and lightweight properties makes it a preferred choice for a wide range of applications. Additionally, aluminum's corrosion resistance and mechanical strength further enhance its suitability for use in various thermal management solutions.

Shaukatullah et al. (1996) concentrated on optimizing the design of pin-fin heatsinks (PFHS) for low-velocity applications to enhance thermal performance. Different aluminum alloys with various fin designs were used to evaluate the effectiveness of each model based on thermal resistance. Additionally, commercial test cases, such as gold chromated and black anodized aluminum base heatsinks, were studied to assess their performance (Shaukatullah et al., 1996). Hirasawa et al. (2005) discussed the evolution of heatsinks from various perspectives. They examined how advancements in materials and design techniques have contributed to reducing the weight of heatsinks while maintaining or enhancing their thermal performance. While copper offers about 400 W/m.K thermal conductivity, its weight is a constraint as an electric device component. Although aluminum has a thermal conductivity of 240 W/m.K , the heatsink would be around 30% lighter even if an aluminum member twice as thick as a copper member is employed to achieve an identical heat transfer rate (Hirasawa et al., 2005). Kumaraguruparan & Sornakumar (2010) designed a micro-channel heatsink using aluminum due to its favorable thermal conductivity for their experimental setup. They studied various criteria, including the Nusselt number, for different water flow rates and heat inputs. Lotfizadeh et al. (2015) performed an experiment utilizing four designs of heatsinks: extruded uncoated and coated longitudinal fin heat sinks, a rectangular commercial aluminum metallic foam, and their innovative heat sink using water flow, aluminum nanocoated metallic foams, and uncoated metallic foams. They concluded that their innovative design utilizing aluminum nanoparticles had a better thermal performance compared to the other test cases. But, due to its high cost and dirt-absorbing ability, the metallic foam heat sink—which performed better than uncoated heat sinks—cannot be a cost-effective solution for industrial applications (Lotfizadeh et al., 2015).

Arifin et al. (2020) studied installing an aluminum heatsink with perforated fins on the thermal performance of photovoltaic (PV) panels during an air-cooling process. The study was conducted using both computational fluid dynamics (CFD) and experimental methods. The results demonstrated that the installed heatsink could effectively reduce the panel temperature. A properly designed heatsink can decrease the risk of panel overheating (Arifin et al., 2020). Phase Change Materials (PCM) have been utilized in experimental and recent numerical studies (Baby & Balaji, 2014) (Kalbasi, 2021). Hosseinizadeh et al. (2011) conducted experimental and numerical research to examine the impact of employing PCM-based heatsinks. They compared their results with test cases without PCM material. During their study, they noticed the temperature increase of the non-PCM heatsink is steady while it is lower for the PCM-based heatsink (Hosseinizadeh et al., 2011). Taghilou & Khavasi (2020) studied 3 aluminum heatsinks with different designs with n-octadecane as the PCM. During their research, they proposed a parameter: the design convective heat transfer coefficient, h_{d}. Lawag & Ali, (2022) overviewed the concept of utilizing PCM for thermal optimization purposes from different perspectives such as production, material choice and its role in thermal control. They concluded filling the heatsinks with metallic fins and embedding nanoparticles with a PCM-base heatsink can improve the thermal conductivity of heatsinks (Lawag & Ali, 2022).

1.1.2 Fin Profile

Fin design and fin shape can be considered as one of the most important criteria when studying a heatsink and its optimization. The thermal performance of the heatsink has a direct relation with the fin profile since it can be considered as a main part of the thermal surface of the component. The shape of the fin, thickness, length and number of the fins, scattered placement or inline placement, and distance between fins should be studied while designing an item. Depending on the intended heat transfer performance, different fin profiles can be offered. Plate channels and pin fins are two of the most practical and famous fin profiles in the industry. Figure 1-2 is an AI-generated illustration of a plate-fin heatsink. The figure shows the plate-fins with different surface areas with parallel inlet and outlet flows.

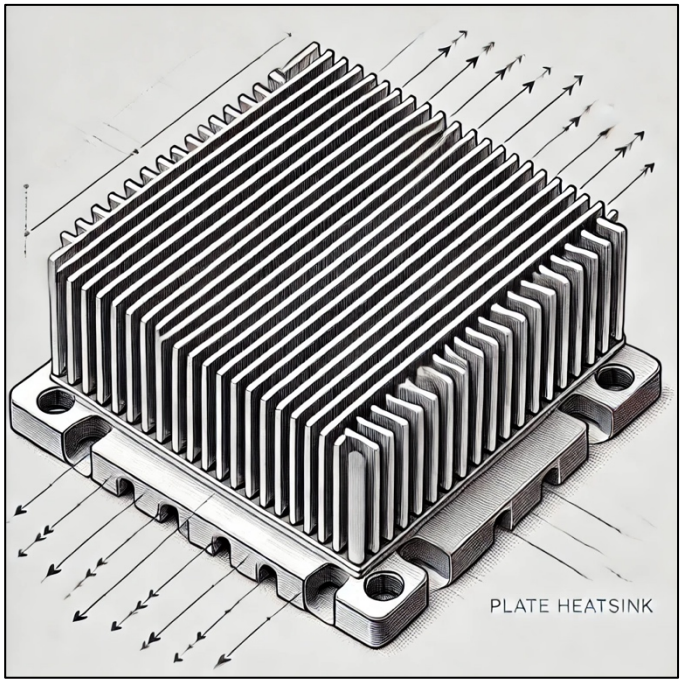

Figure 1.2 AI-generated illustration of a plate
Heatsink
Taken from « ChatGPT » s.d.

Finding the ideal fin profile has been the subject of researchers' and engineers' projects to find optimized options for their systems (Ping, Peng, Kong, Chen, & Wen, 2018) (Ahmed, Salman, Kherbeet, & Ahmed, 2018). Goldberg (1984) designed a copper-based narrow channel heatsink, which can be considered a plate fin heatsink subject to an airflow cooling system. It was tested with three different plate measurements to study the effect on thermal performance. They concluded thermal performance will be optimized by removing the substrate from the thermal path of the heatsink which leads to decrease of thermal resistance. To emphasize the efficiency, Phillips (1988) designed a microchannel heatsink as part of their experimental work while detailing the fabrication techniques. The compact heat exchanger known as a microchannel heatsink employs small channels to improve heat dissipation by maximizing surface area for heat transfer and encouraging fast coolant flow. Its effective thermal management abilities make it a popular choice for electronics cooling and other applications

with high heat flux. The study concluded microchannel heat sinks radiate a lot of heat with a minimal increase in surface temperature.

Chapman et al. (1994) conducted an experimental study on three different aluminum based heatsinks featuring crosscut, elliptical, and straight (plate) fins. The research focused on factors such as thermal resistance, forced convection performance for the entering air velocity to evaluate the performance of each heatsink. The observations revealed that the straight-fin heatsinks exhibited the lowest flow bypass and thermal resistance compared to the other two designs. Sikka et al. (2000) designed and constructed heatsinks with fluted, and wavy fins and compared their performance to plate and pin fin configurations under low-velocity natural airflow conditions.

Three dimensionless number characterize the heatsinks. The Nusselt number is a dimensionless number that represents the ratio of convective to conductive heat transfer across a boundary in a fluid flow. The Reynolds number is a dimensionless quantity that indicates whether fluid flow is laminar or turbulent, based on the ratio of inertial forces to viscous forces in the fluid. The Rayleigh number is a dimensionless number that characterizes the onset of natural convection in a fluid, representing the balance between buoyancy forces driving the flow and viscous forces resisting it. Sikka et al. (2000) studied the Nusselt number for various Reynolds numbers and Rayleigh numbers. Jousson & Palm (2000) conducted a study on nine heatsink designs with plate and pin fins of varying lengths. The fins were arranged in staggered configurations for some test cases and in line for others.

Jonsson & Moshfegh (2001) also performed experimental work to study the behaviour of heatsinks with different fin designs. In 2001, Jonsson & Moshfegh investigated 3 types of fin configuration: plate, strip and pin fins for 7 heatsink designs. Each heatsink design was studied for 3 different fin heights and models were also both in staggered and inline placements, which led to the experiment of 42 test cases. Figure 1.3 demonstrates the configuration design of the fin designs of experimental work of Jonsson & Moshfegh (2001). Each fin shape was studied in 3 different height and fin-position.

Their results demonstrated that in zero bypass ducts at high Reynolds numbers, strip fin heat sinks show a lower pressure drop compared to pin fin heat sinks, with a minimal variance in thermal resistance, thereby diminishing the advantage of pin fin heat sinks in such scenarios.

Jonsson & Moshfegh (2001) also concluded that the Nusselt number prediction is most influenced by the Reynolds number and the relative duct height (CH/H), and all the parameters examined have a significant impact on predicting the dimensionless pressure drop. Moreover, they created an empirical bypass correlation for various fin designs that accurately estimated the Nusselt number, and the dimensionless pressure drop. However, the last one needed additional refinement to increase design usability. Moshfegh & Nyiredy (2004) utilized the results of the study for further numerical investigation.

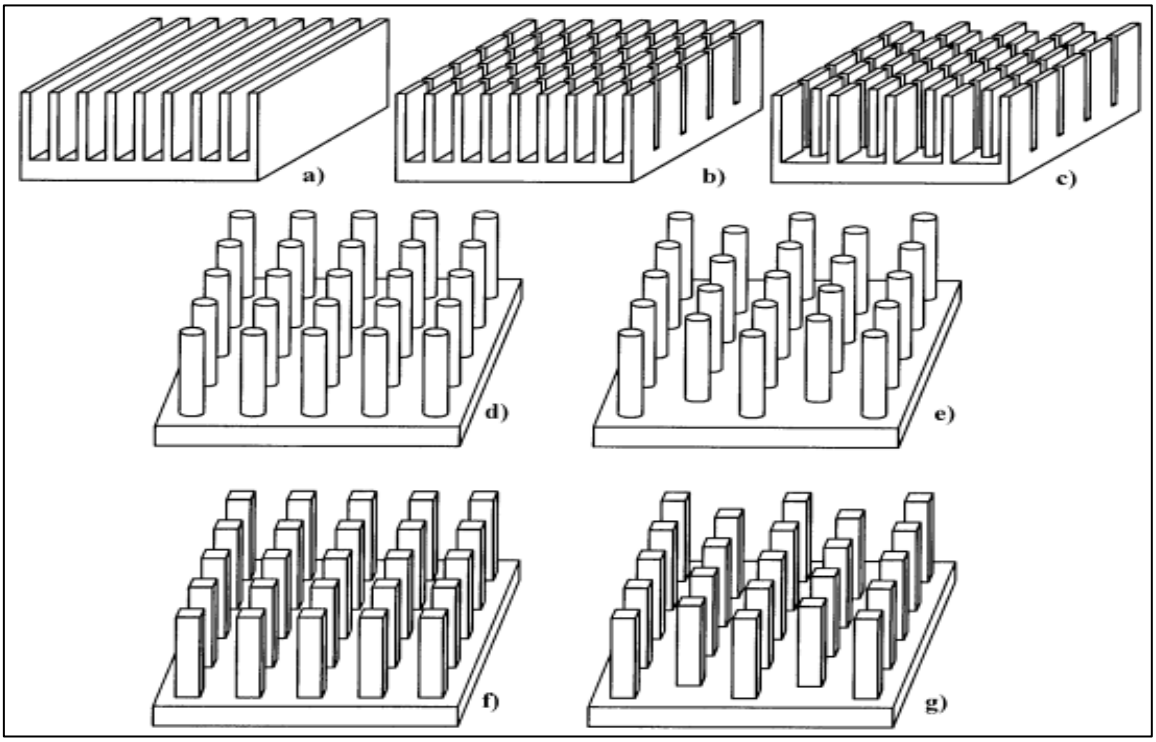

Figure 1.3 Fin Configuration of Jonsson & Moshfegh (2001) experimental work:
Plate fin heat sink (a), strip fin heat sinks with in-line, (b) and staggered,
(c) arrays, circular pin fin heat sinks, (in-line (d) and staggered (e) arrays),
and square pin fin heat sinks (in-line (f) and staggered (g) arrays)
Taken from Jonsson & Moshfegh (2001a)

Kim (2012) concentrated on the heatsinks with varying fin thickness. Enhancing the thermal performance of a vertical plate-fin heat sink under natural convection was the goal of the project. They obtained a 10 percent optimization of thermal resistance by the fin thickness

increases in the direction perpendicular to the flow. However, the difference in thermal resistance between heatsinks with uniform thickness and those with variable thickness diminished as the height and heat flux decreased (D.-K. Kim, 2012). Figure 1-4 shows the fin design: (a) Rectangular, (b)Triangular and (c) Reverse trapezoidal of Kim (2012) work.

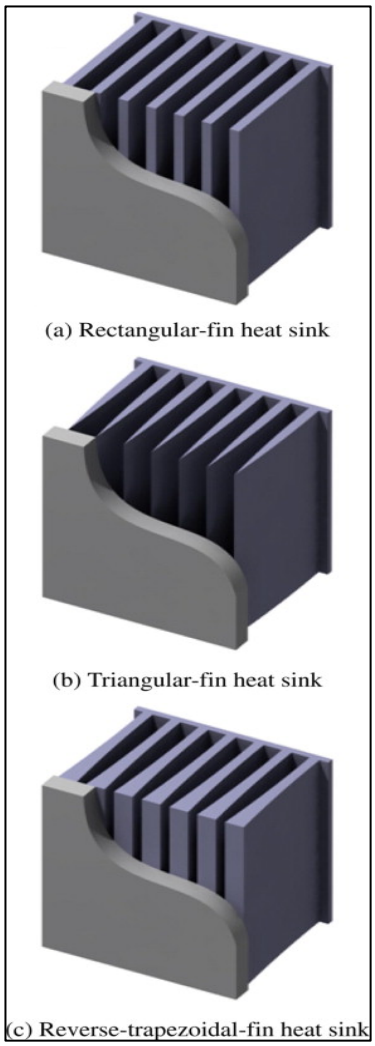

Figure 1.4 Heatsink models
Taken from
D.-K. Kim (2012)

Perforation of the fins is one of the modifications that can improve the thermal conductivity of the heatsinks. Depending on the cooling target and the design of the heatsink, the number of perforations can vary. Ismail (2013) studied the thermal and fluid performance of a heat exchanger with a concentration on the perforation of the heatsinks. The numerical study

focused on the behaviour of different types of perforated fins installed on a base plate, considered as heat exchangers of the system. They considered laminar forced convective heat transfer conditions and studied the test cases for different Reynolds numbers. The obtained results showed better performance due to the higher contact surface with the flow compared to the solid fins (Ismail, 2013). Figure 1-5 shows the perforation design of Ismail (2013) study.

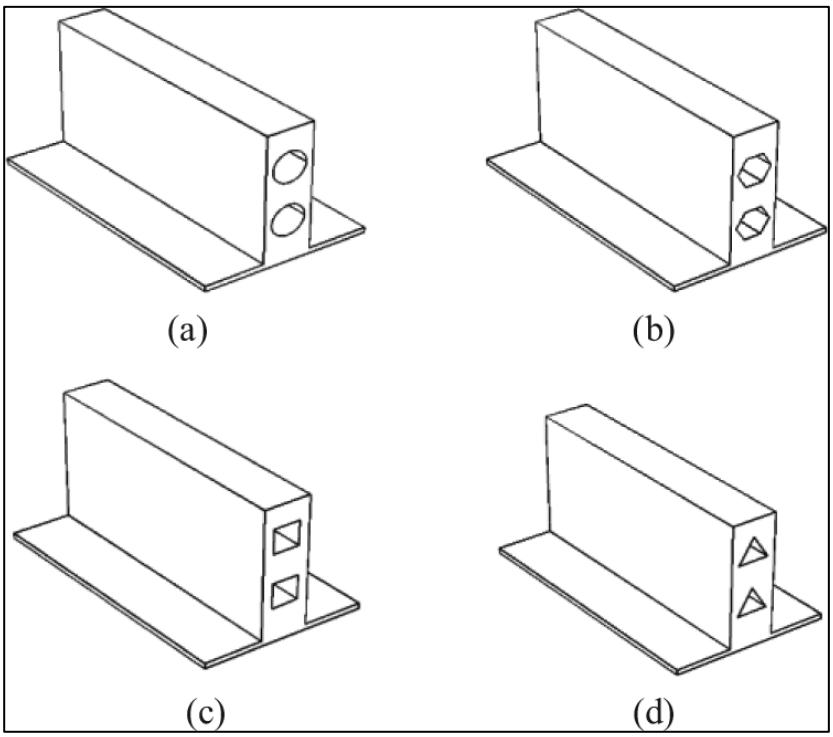

Figure 1.5 perforated fin design Ismail (2013).
Different types of perforated fins have the same surface area
(a)Circular. (b) Hexagonal. (c) Square. (d) Triangular

Al-Damook et al. (2015) worked on the position and number of the perforation of the fins from the numerical and experimental perspectives. Results showed that employing multiple pin perforations can result in significant performance advantages by enhancing heat transfer and lowering both the pressure drop across the heat sink and the fan power required to drive air through them. The perforated fin with 5 perforations demonstrated 15% optimization in Nusselt number and 11% in pressure drop compared to the solid fins. Figure 1-6 shows the fin-

perforation of the Al-Damook et al. (2015) project. The number of the perforations and their position is different for each model.

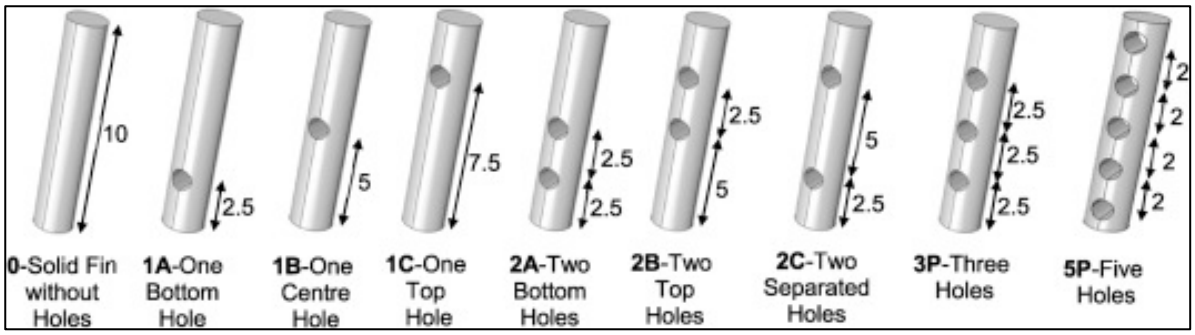

Figure 1.6 . Perforation design of the fins for Al-Damook et al. (2015) work
Measurements are in mm

1.1.3 Geometrical Dimensions

The dimensions of each part of the heatsink are important part for heatsink design. Multiple properties such as the thickness of the plate, size of the plate, and size of the fins should be studied. The size of the base plates and fins affects the thermal surface directly; therefore, it can improve or downsize the thermal performance of the heat exchanger. Depending on the size of the electric device and the cooling purpose of the HS, these measurements can vary.

Yu & Chen (1999) concentrated on the optimum fin length for different methods of heat transfer. They defined the concept of the optimization in their work as finding the shape and dimensions of the fins which leads to 2 objectives: one goal is to lower the volume or mass of a heatsink while retaining a certain heat dissipation capacity. The other goal is to improve heat dissipation performance within a specific volume or mass limitation. The independence of the fin from the fin base temperature during convection was one of their conclusions. Moreover, they concluded that for both convection-radiation and pure radiation with the flow, the optimal fin length is shorter at higher temperatures compared to lower temperatures(L.-T. Yu & Chen, 1999).

Kang (2007) studied the effect of the fins' base thickness on the thermal behaviour of a heatsink as a part of their 2D CFD-study. They concluded that reducing the fin base thickness resulted

in increased optimal heat dissipation and corresponding fin effectiveness (Kang, 2007). Mohan & Govindarajan (2010) analyzed the thermal behaviour of the CPU utilizing heatsinks with various base plate thicknesses from a CFD perspective. Moreover, they concentrated on the number and thickness of the fins to find the optimum options for the CPU. They concluded that overusing the number of fins will not improve the heat transfer process due to the decrease of space for air passage. Mohan & Govindarajan (2010) also concluded that increasing the base plate thickness improved the performance of heatsink which is in contradiction with Kang (2007) conclusion.

Utilizing a two-stage optimization, F. Wang et al. (2013) tried to improve the thermal performance of a thermoelectric generator (TEG). The heat transfer of the heat sink was modelled using an analytical method. The performance of the TEG was predicted utilizing a finite volume method. The study concluded that fin thickness has a negligible impact on the heatsink's performance, even at the optimal compromise point between TEG performance and heatsink efficiency. The key factors influencing performance were the length and frontal area of the heatsink, rather than the thickness of the fins (F. Wang et al., 2013).

Arshad et al. (2017) conducted an experimental study to investigate the effect of fin thickness on the performance of a PCM aluminum-based heatsink, maintaining a constant fin height. The performance of the heatsink was studied based on the improvement of the thermal resistance. The volume fractions of PCM were varied as 0.00, 0.33, 0.66, and 1.00 for each heatsink to assess thermal performance. The study concluded that the maximum thermal performance during operation was achieved with a 2 mm thick pin-fin heatsink filled with a PCM volumetric fraction of 1.00.

1.2 Inlet and Outlet Flow

Heat dissipation efficiency and overall thermal performance are impacted by the inlet and outlet flow, so these flow patterns are important for heatsink optimization (Hempijid & Kittichaikarn, 2020). The heat transfer efficiency of the heatsink depends on the direction of the flow around the fins (impinging or parallel). The rate of airflow across the heatsink affects the heat dissipation process. Higher airflow rates often enhance cooling efficiency but may

necessitate more powerful fans and increased energy usage. The setup of the inlet and outlet apertures, including their size and position, can improve the airflow pattern and heat removal. The role of the direction of the inlet and outlet flow in the performance of heatsinks has been a primary objective in multiple studies in the last decade. Researchers have investigated how various airflow directions, such as parallel, and impinging, impact heat dissipation efficiency. Khattak & Ali (2019) reviewed various aspects of heat sink design, limitations and recent advancements. They focused on the flow regime and its importance to improve the performance of heatsinks. They briefly discussed the parallel, impinging and by-pass airflow and concluded that there is a lack of literature regarding the flow direction (Khattak & Ali, 2019). Based on their results, until 2019, there were only 11 % available literature from 8 studies that they reviewed in their work aiming at impinging flow.

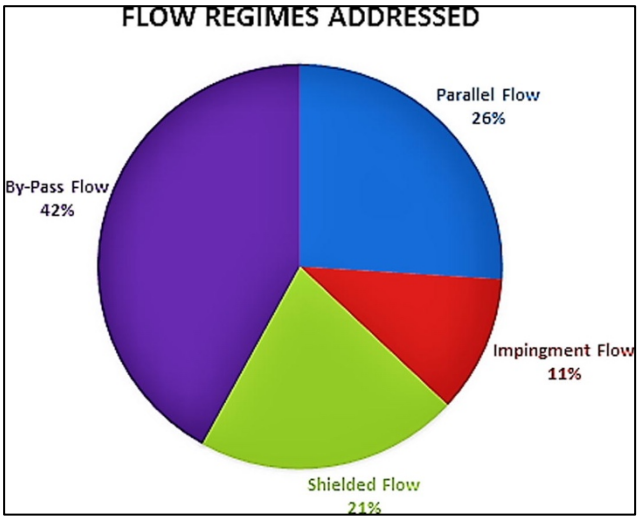

Figure 1.7 Addressed Flow Regimes in Literature
Taken From Khattak & Ali (2019)

Jonsson & Moshfegh (2001) studied the behaviour of their case studies considering parallel airflows, experimentally. Moshfegh & Nyiredy (2004) utilized the result of the previous work with the same flow regime but for their numerical work.

Kim & Kim (2009) studied the cross-cut effects on the thermal behaviour of a heatsink, with a focus on a parallel airflow regime. The study established connections between the thermal efficiency of the heat sinks exposed to parallel flow. The study considered the pressure drop and thermal resistance change based on the pumping power and Reynolds number as factors for thermal efficiency. Furthermore, the length of the cross-section was identified as a significant factor influencing the performance.

El-Sheikh & Gurimella (2000) experimented to improve the heat transfer of a heatsink subjected to an impinging airflow. Considering different Reynolds numbers and nozzle diameters, they concluded that when the flow rate is constant, heat transfer increases with a decrease in nozzle diameter.

Li et al. (2005) focused on confined impingement cooling and its effect on the thermal behaviour of a heatsink. They investigated the impact of the Reynolds number, fin width and height, distance between the nozzle and fin tip, and heat sink type on thermal resistance. As a part of their conclusion, they mentioned that the thermal resistance depends significantly on the Reynolds number of the impinging jet. An increase in the Reynolds number systematically reduces the thermal resistance. Additionally, the rate of decrease also decreases as the Reynolds number increases (Li et al., 2005).

To focus on the impinging airflow, Li & Chen (2007) conducted an experimental research to investigate the impact of impingement spacing (the ratio of nozzle distance to nozzle diameter ($\frac{Y}{d_{nozzle}}$)) on the thermal dissipation performance of plate-fin heat sinks at different Reynolds number ranges. Decreasing the impinging distance can result in reduced heat transfer. Figure 1-8 shows the experimental set-up of Li & Chen (2007) work. The position of the heatsink, the inlet nozzle which produces the impinging jet and the distance between these two items are considerable.

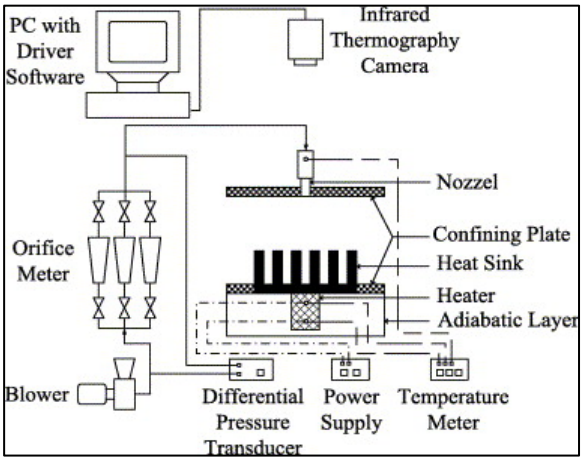

Figure 1.8 he schematic diagram of
the experimental set of Li & Chen (2007)

Li et al. (2007) designed a new hybrid micro-jet impingement/micro-channel heat sink. They studied parameters such as the fin inclination angle, fin height and fin length utilizing previous computational and experimental studies. During this study, utilizing a hybrid micro-jet impingement/micro-channel approach improved the thermal-hydraulic performance of the heat sink. It enhanced heat transfer rates and reduced thermal resistance which offer an efficient solution for handling heat dissipation in high-power electronic applications (Cui et al., 2024).
The bypass effect is an important aspect related to the inflow and outflow. Wirtz et al. (1994) believed there was a lack of literature regarding the bypass effect and its importance, therefore they conducted an experimental setup for a longitudinal fin heatsink which in this study is demonstrated as plate-pin fin heatsink attached to an electronic package which underwent forced convection air cooling in a regular array. The goal was to measure and reduce the effects of air circulation bypass. The research assessed how much of the airflow goes around the heat sink. In the case of the specific finned structure, as much as 60% of the incoming flow avoids the heat sink, resulting in a 50% decrease in its ability to dissipate heat.
Jousson & Palm (2000) conducted a comprehensive experimental study to explore the thermal performance of a heatsink under different bypass conditions considering parallel airflow. They tested nine different heatsink models, creating various flow conditions compared to the length of the heatsink and the fin heights. The pressure drop and thermal resistance of different

Reynolds numbers for the bypass conditions of the experimental results were in good agreement with a simple physical bypass model for laminar airflow (Jousson & Palm, 2000).

To address the importance of the presence of clearance on a bypass factor, Sparrow & Kadle (1986) performed experiments to investigate how heat transmission from a longitudinal fin array changes when there is space between the fin tips and an adjacent shroud. The investigation focused on the impact of varying the clearance on inlet and outlet airflow, which in turn affects the airflow pattern and distribution through the heatsink, on the heat transfer efficiency. In this study, the efficiency of heat sink was considered based on the improvement in fin efficiency and heat co-efficient ratio. The research demonstrated that the efficiency of heatsinks is directly affected by the presence of clearance, as it changes the airflow distribution and consequently influences heat transfer efficiency. This connection offers important perspectives for improving heatsink designs, especially in scenarios where limited space requires clearances between fins and shrouds.

Xia et al. (2023) focused on the effect of the inlet and outlet flow position on a microchannel heatsink performance from a topology perspective. Xia et al. (2023)'s primary focus was on improving the cooling performance and efficiency of microchannel heat sinks using topology optimization. The research project centred around optimizing the design of microchannel heat sinks by testing out five different combinations of inlet and outlet structures, using bi-objective topology optimization based on the density method. The ultimate goal was to minimize power dissipation and maximize heat generation, with the overall objective of enhancing the thermal performance of the microchannel heat sinks.

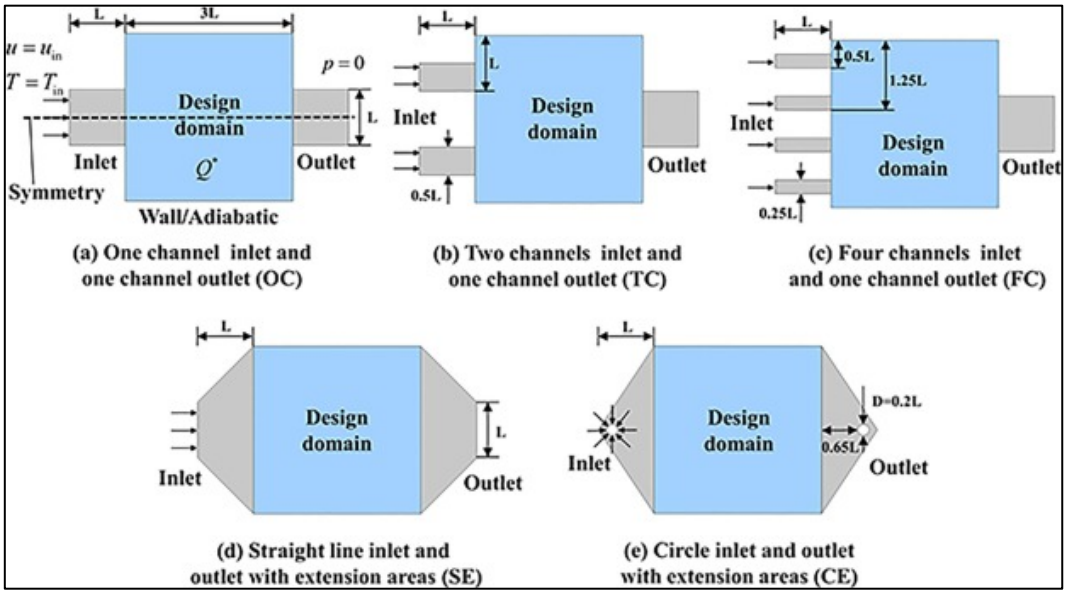

Figure 1.9 The 2D model of liquid-cooled heat sinks with five different inlet and outlet combinations from Xia et al. (2023)

Figure 1.9 shows the different Inlet and Outlet setup for Xia et al. (2023) work. The SE setup is the most efficient design, providing significant enhancements in heat transfer efficiency and reduction of power dissipation. The research results offer valuable guidance for developing more effective cooling systems for electronic use (Xia et al., 2023).

1.3 RANS, Menter's SST, CFD Studies on the thermal behaviour of heatsinks:

Osborne Reynolds, born in 1842, is a well-known contributor to the fluid mechanic, who represented the Reynolds-Averaged Navier-Stokes (RANS) equations. His two main articles Reynolds (1883) and (Reynolds (1895) have had leaded many researchers to ground-breaking development in CFD.

RANS equations are utilized to simulate fluid flow, especially within the realm of computational fluid dynamics (CFD). RANS is frequently used to forecast turbulent flows (Nichols, 2003), which are distinguished by disorderly and unpredictable variations in the fluid velocity field. Averaging the Navier-Stokes equations over time or space results in the derivation of the RANS equations. Since direct simulation of all turbulent scales is computationally costly (especially for high Reynolds number flows), RANS employs

turbulence models to simulate the influence of turbulence on the mean flow. These models incorporate new terms called the Reynolds stresses, which describe momentum transfer owing to turbulence. The most common turbulence models are the k-ε model (Jones & Launder, 1972), the k-ω model, the SST model (« Turbulence Modeling Resource », s.d.), and the Spalart-Allmaras model (Spalart & Allmaras, 1992). RANS is used to simulate and study turbulent flow behaviour in many engineering applications, including aerodynamics, hydrodynamics, heat exchangers, HVAC systems, and automotive engineering (Corson, Jaiman, & Shakib, 2009). Alfonsi, 2009) reviewed the RANS equations for the turbulent flows with the main focus on the limit of incompressible flows with constant properties.

1.3.1 Menter's Shear Stress Transport (SST):

Developed by Menter (1994), the Shear Stress Transport (SST) model is a turbulence model utilized in computational fluid dynamics (CFD) for forecasting turbulent flow characteristics. The idea was established with two articles Menter (1993) Menter (1994). The goal of the model was to predict aeronautics flows with intense adverse pressure gradients and separation accurately. In 2004, Menter utilized the SST model to simulate the flow over Ahmed's car body at a 25° slant angle. To evaluate the role of the SST in the industry, Menter (2009) overviewed the model outcomes in an article.

SST's effectiveness is notable in simulating flows with disruptive pressure gradients and boundary layer separations, leading to widespread adoption in aerospace, automotive, and turbomachinery engineering applications. The SST model offers a fair compromise between accuracy and computing cost, making it appropriate for a variety of applications.

1.3.2 CFD studies on heatsinks thermal behaviour behaviours:

Computational Fluid Dynamics (CFD) has played a significant role in developing and optimizing heat exchangers. While experimental researchers gather real data from case studies, numerical simulations help researchers predict and define the thermal behaviour of these systems. Various parameters such as pressure drop, thermal resistance, bypass factor, and

Nusselt number can be studied using CFD across different conditions, such as varying Reynolds and Rayleigh numbers. CFD studies can address the limitations of experimental work.

Pressure drop is important in heat sink design since it influences cooling performance, energy economy, noise levels, and the dependability of electronic equipment.

The bypass factor is important in heat sink design because it demonstrates the airflow that bypasses the heat sink rather than flowing through it to remove heat. A high bypass factor implies less air is accessible for cooling, resulting in worse thermal performance.

Thermal resistance is essential in heat sink design since it determines the heat sink's capacity to transmit heat away from the device. Lower thermal resistance implies more effective heat dissipation, which is critical for keeping operating temperatures stable and assuring the performance and lifetime of electronic components.

The Nusselt number is a significant indicator in heat sink design because it measures the efficiency of convective heat transfer vs conductive heat transfer over a barrier. A higher Nusselt number implies better convective heat transfer, which is desired for efficient cooling in heat sinks.

Behnia et al. (1998) developed a CFD model in which 2D Navier-Stokes and energy equations for the incompressible laminar flow were imposed. They performed Two-dimensional CFD simulations**.** For the thermal condition, an isothermal boundary was considered. The study used periodic boundaries for the inlet and outlet, symmetry conditions in the transverse direction, and isothermal conditions on solid surfaces. All fluid properties were assumed constant. Triangular elements with second-order discretization were generated for the mesh. They refined their mesh until the Nusselt number difference was less than 0.5%. therefore, for the most sensitive case, they had 50000 elements. They analyzed a group of in-line and staggered pin-fins with 1 mm diameter. For the inline circular pin-fins, the surface heat transfer coefficient demonstrated a change of 60 to more than 100 ($\frac{10^4 W}{cm^2 K}$) with varying pressure drop from 0 to 100 ($\frac{Pa}{cm}$). The circular fins showed better thermal behaviour compared to the square fins. Better thermal behaviour is defined as higher heat transfer performance with lower pressure drop and power pumping requirement.

Moshfegh & Nyiredy (2004) followed Jonsson & Moshfegh (2001) experimental work, by developing a CFD study for 5 different turbulent flow models: the standard *k*-ε, RNG, the realizable and the *k*-ω model, as well as the Reynolds stress model, RSM (Moshfegh & Nyiredy, 2004). Following the experimental model, the case study was aluminum pin-fins with parallel airflow conditions. The computational domain encompasses both the solid heat sink (base plate and pin fins) and the fluid domain (air). To capture the thermal interactions between the solid and the fluid, the study used a conjugate heat transfer (CHT) model. Three test cases were modelled based on the boundary conditions of their experimental work with different inlet velocities. 360 333 hexahedral cells were used for the coarse mesh and 1 710 027 cells for the fine mesh. The first point above the wall was located at y+>15. For the pressure drop, the case studies showed a better agreement between the RNG model and the experimental results.

Following the work of Jonsson & Moshfegh (2001) and Yu et al. (2005), a CFD model was developed by Zhou & Catton (2011). An SST model was used to forecast the turbulent flow and heat transfer across the heat sink channels. Regarding the pressure drop, to prevent the build-up of turbulence in the stagnation region a production limiter is used in the SST model(Zhou & Catton, 2011):

$$P_k = \mu_t \frac{\delta u_i}{\delta x_j}\left(\frac{\delta u_i}{\delta x_j} + \frac{\delta u_j}{\delta x_i}\right) \rightarrow \tilde{P}_k = \min\left(P_k\,, 20\ \cdot \beta^* \rho k \omega\right)$$

They focused on a single passage between adjacent fins of a heat sink as the computational domain, chosen due to the fin geometry's periodicity in the spanwise direction. To accommodate the non-uniform air velocity profile caused by the fin thickness at the channel entrance, the computational domain was extended upstream by 0.5 times the fin length and downstream by one fin length. Inlet boundary conditions were established with various inlet velocities (ranging from 5 m/s to 9.4 m/s) to attain specific wind velocities (6.5, 8.0, 10.0, and 12.2 m/s) within the heat sink channels, while a pressure boundary condition was implemented at the outlet. The solid-fluid interface was simulated as a no-slip wall with no thermal resistance

while the heat sink's bottom surface had an iso-heat-flux thermal boundary condition with a total heat load of 10 W. A structured hex mesh was generated, tailored for flow-aligned geometries to minimize false diffusion. A finer mesh was applied near the fluid-solid interface to accurately capture near-wall flow behaviour, ensuring y+ values remained below 1. To achieve grid independence, the mesh was recursively refined until pressure drop and thermal resistance variations were less than 0.5% (Zhou & Catton, 2011). For the pressure drop, they validated their CFD results with the experiments of Moshfegh and Yu for various inlet velocities. The goal of the study was to study the effectiveness of adding pin fins with different shapes to the plate fin heatsinks in thermal performance which was considered as improving heat dissipation efficiency while minimizing the pressure drop. While the pressure drop of the pin-fin was higher than the plate heatsinks for the inlet velocity between 6.5 to 12.2 m/s, it was lower than the circular Plane Pin-Fin Heatsink (PPFHS). The results were also evaluated for different dimensionless widths (ratio of the pin fin width to the plate fin spacing) at the wind velocity of 6.5 m/s.

In a computational study, Vasilev et al., 2021 simulated seventeen different models of microchannel heat sinks (MCHS). These models featured channels with circular pin fins of different diameters, spacing, and heights to compare their performance with a traditional MCHS. A model combining solid and fluid in three dimensions was utilized. Navier-Stokes equations were solved to perform hydrodynamic and thermal simulations for heat sinks, using a three-dimensional solid-fluid conjugate model within a single-phase, steady-state, flow environment. The validation for mesh independence was carried out for microchannel heat sinks without fins to ensure the reliability of the numerical solutions. Grid independence tests involved refining the grid and comparing the results of the numerical simulations for pressure drop. A physically controlled adaptive tetrahedral mesh with varying sizes (approximately 412,000, 1,133,000, and 3,760,000 elements) was employed to analyze mesh sensitivity for liquid velocity at 0.1 m/s. The computed values for velocity and temperature showed a percentage error of less than 1% between the fine and finer mesh, confirming that further mesh refinement does not affect the numerical solution. The results demonstrated the dependence of the pressure drop on the Reynolds number and constant ratio of the fin spacing for both experimental and numerical results.

Khetib et al. (2021) simulated turbulent nanofluid water-base flow in a channel with a pin-fin heatsink, considering different fin shapes (hexagonal, circular, square, and triangular) and arrangements. The standard k-ε turbulence model and SIMPLEC method were used for simulation. For their model, they compared the standard k-ε with k-omega SST and no difference was found for thermal resistance and pressure drop. For the mesh study, they performed a grid independence test to find the appropriate grid resolution. At an inlet velocity of 1 m/s, the outlet temperature and pressure drop (ΔP) were compared for several different mesh sizes. They utilized an unstructured grid to maintain accuracy while minimizing unnecessary computational complexity. The convergence criteria was set at 10^{-4} for velocity equations and 10^{-6} for the energy equation**.** The study did not consider conjugate heat transfer. It treated the nanofluid as a homogenous, single-phase fluid and assumed that the heat flux at the bottom of the heatsink was constant, without solving the solid's heat conduction equation. With a focus on the pressure drop at the inlet and outlet, they concluded that circular fins require less pressure drop to operate.

Li et al., 2007) evaluated the performance of pin-fin heat sinks with confined impingement cooling using numerical simulations. They explored the impact of different variables such as Reynolds number, height and width of the fins, thermal conductivity, and the quantity of fins on thermal resistance. They used the RANS equations and the energy equation in the study to simulate fluid flow under steady, incompressible, and turbulent conditions. They utilized the κ−ε turbulence model. A control volume approach discretizes the equations for the flow and the conjugate heat transfer. The computational domain consists of a confined impingement cooling setup with a pin-fin heat sink. It includes confining plates around the nozzle exit and the sides of the heat sink base, which are thermally insulated. The pressure-velocity coupling utilizes the SIMPLE algorithm, and solving the equations involves an iterative method with algebraic multigrid. Under-relaxation factors are 0.3 for pressure, 0.7 for momentum, 1 for temperature, and 0.5 for both turbulent kinetic energy and dissipation rate. Iterations continue until scaled residuals fall below 10^{-3} for most equations and 10^{-7} for the energy equation. The thermal resistance reduced as the Reynolds number increased. As the Reynolds number grew, the loss in thermal resistance decreased. Meanwhile, the thermal performance increased as the fins' height increased. The decrease in heat resistance grew less as the fin height increased.

Vasilev et al., 2021) concluded the height of the pins has a significant impact on the thermal resistance of microchannel heat sinks (MCHS). Therefore, they offered a model for specific fin height which improved the thermal resistance by around 40% compared to the other models. Behnia et al. (1998) analyzed the Nusselt number of a group of in-line and staggered pin-fins with 1 mm diameter for Reynolds numbers varying from 100 to 1000. For the circular in-line fins, the Nusselt number was changed from 10 to 20 for the Reynolds numbers between 100 to 1000 which was in good agreement with their experimental results.

The Nusselt numbers of the Pin-Fin heatsinks was the subject of of Zhou & Catton, 2011) . This research conducted a numerical analysis of heat sinks featuring plate and pin fins through CFD. The k–ω SST turbulence model is utilized, and a structured hexahedral mesh is implemented to improve solution accuracy. The study was investigated for different velocities and dimensionless widths at the wind velocity of 6.5 m/s. The Nusselt number of the pin-fin heatsink was 9% higher than the Plate-Fin heatsink. The PPFHS had 60 % higher Nusselt numbers compared to the Plate-Fin heatsink. Vasilev et al., 2021 emphasized the dependence of the Nusselt number on the height of the fin and offered an optimal height to increase the Nusselt Number.

Thakar et al. (2021) investigated the heat transfer characteristics of a circular array of air jets impinging on a heat sink under a thermal load. The objective was to keep the ideal temperature to ensure the efficient operation of the components. The simulations used a conjugate heat transfer model and the SST k-ω turbulence model. The mesh was built of tetrahedral elements. The mesh size is not specified in the article but, the problem was solved with 1000 iterations, with 1e-06 residual limit for continuity and energy equations, suggesting a well-refined grid. The simulation focused on fluid flow in a stationary air domain, with an impinging air jet at a specific velocity. Key parameters included the Reynolds number (Re) at the inlet, The Reynolds number are 6000, 8000, and 10000, while the Z/d ratio was set

at 4, 6, and 10. The jet diameter is kept constant at 8 mm, and the inlet velocity was determined based on the Reynolds number and the inlet diameter used as the characteristic length. The surface Nusselt number, and stagnation Nusselt number for different dimensionless lengths(Z/d) were studied. The most effective configuration of the test cases for heat transfer

characteristics occurred with a Z/d ratio of 6 and an inlet Reynolds number of 12,000. This configuration attained a static steady-state temperature of 60 °C, which was the lowest recorded. Furthermore, it exhibited the highest stagnation Nusselt number (5550), average Nusselt number (5237), and surface heat transfer coefficient (126.750) when compared to all testcases.

Sahray et al. (2010) looked at conjugate heat transfer from horizontal-base pin-fin heat sinks with exposed edges in free convection settings. They used RANS for numerical simulations, modelling both the sinks and their surrounding environment. The simulations utilized a grid featuring a higher resolution closer to the edges, especially around the base and fins A non-uniform grid with a variable step size, and the details mentioned that hexahedral elements were utilized. The grid was adjusted until minimal changes were observed. Detailed modelling was necessary for the most compact setups with 256 fins and narrow 2 mm passages. The height of the computational domain extended beyond the outer box dimensions, and pressure outlet conditions were implemented for both the upper boundary and vertical extensions of the box walls. The study separated the impacts of natural convection and radiation, extending the findings by employing Rayleigh and Nusselt numbers and considering the distance between the fins as the characteristic dimension. The distance between fins is defined as the distance between neighboring fins, which serves as the defining length in the suggested correlation for the Nusselt number in relation to the Rayleigh number. This study showed the variation of the Nusselt number with fin height and spacing, offering valuable information for enhancing heat sink design.

For the Moshfegh & Nyiredy, (2004) case studies, they analyzed the effect of the inlet velocity on the bypass ratio. Their results demonstrated that an increase in the velocity decreases the bypass ratio which resulted in more air moving through the heat sink package. They studied the Reynolds numbers: 5000,9500,14500. They generated unstructured 3D coarse and finer grids. The coarse mesh has 360,333 hexahedral cells with 108×58×32 mesh distribution. The mesh is clustered near walls and edges, ensuring the first numerical point at y+ > 15. The finer grid has 1,710,027 cells. They considered y+ close to 1 near walls and edges. They utilized the

k-ω model for computation. The CPU time was 8 hours on a 1.4 GHz Pentium-4 for the fine grid results.

In this review, we examined previous experimental and numerical studies conducted by other researchers. We initially explored the characteristics of heat sinks, followed by an analysis of the significance of flow geometry. Additionally, we provided an overview of prior CFD research on the thermal behaviour of heat sinks. This Review demonstrated that CFD is a valid tool to study the heat transfer of the heatsinks. Multiple studies showed that several flow and geometric dimensions can affect heat transfer.

No universal correlations exist to predict pressure drop and heat transfer, therefore, for specific geometries, experimental or CFD studies are needed to estimate heat sink efficiencies.

CHAPTER 2

Mathematical Model and Numerical Method

2.1 Introduction

Critical in electronic devices, heatsinks play a crucial role in managing the thermal and cooling processes of these system. The analysis and optimization of heatsink designs rely on simulations and models in computational studies addressing the significant challenges related to heatsinks and their performance. These studies offer insights that can enhance the pressure drop and thermal resistance of heatsinks.

The first chapter presented a summary of previous research on heat transfer and heat dissipation in heatsinks exposed to an inlet flow. This overview emphasized the different methods and approaches utilized in earlier investigations to comprehend the behaviour of heatsinks under various flow conditions. Furthermore, the crucial role of numerical findings and Computational Fluid Dynamics (CFD) simulations in advancing our understanding of this topic was explored, demonstrating the effective use of these tools in examining and enhancing heat exchanger performance. The knowledge gained from these studies serves as the basis for the current chapter.

This chapter will provide an overview of the methodology and mathematical framework utilized in the present project. The aim is to demonstrate the interconnection between the mathematical model and methodology in deriving the outcomes. It begins with the problem definition, where the case study is analyzed using the governing equations and relevant assumptions. Subsequently, the computational domain and boundary conditions are defined, leading to the generation of the mesh. Finally, the computational resources and software utilized for the analysis are discussed.

2.2 Problem definition

Heat transfers are studied for two geometries. The first geometry, a jet impinging on a flat plate, is used for verification and validation of the conjugate heat transfer method and the RANS model. A round jet with a diameter D impinges a uniformly heated circular flat plate at a right angle. The jet has a temperature of 293.15 K, while the bottom of the plate is maintained at a constant temperature of 303.15 K. The jet exits from a nozzle and behaves like a free submerged jet as it travels through the surrounding air. Velocity gradients at the jet's edges create shear forces that draw in additional fluid toward the plate. As the jet approaches the flat plate, its velocity profile expands, and its speed decreases. Near the wall, the jet loses its normal velocity component and redirects to flow parallel to the surface.

The objective of this part is to calculate the steady-state heat transfer coefficient, h, along the radius r of the circular flat plate, from the point of jet impingement to the plate's edge, while accounting for conduction within the plate. For a jet nozzle with diameter D and fluid thermal conductivity k, the results will present the Nusselt number, $Nu = hD/k$, as a function of r/D. This document outlines the mesh configurations and the SU2 solver setup for two cases. the Impinging jet where r/D=2 and r/D=6 and the Reynolds number Re=23,000 and Re=70000. The SU2 output files, located in the specified directory, should be validated against the findings of G. Zhang et al. (2019) work.

The second test case is a pin fin heat sink. As discussed in the previous section, Jonsson & Moshfegh (2001) examined 42 test cases as part of their experimental study on heatsinks, underscoring the significance of empirical research in validating and enhancing computational models. These test cases were studied based on different properties and their effect on their thermal performance. Moshfegh & Nyiredy (2004) utilized the previous experimental results of Jonsson & Moshfegh (2001) work to develop their model from a computational point of view. For the 2D flow of the pin fin heatsink, Re=4000,6000,10000,12400 were studied

A 2D geometry and computational domain were defined define based on Jonsson & Moshfegh, 2001 work.

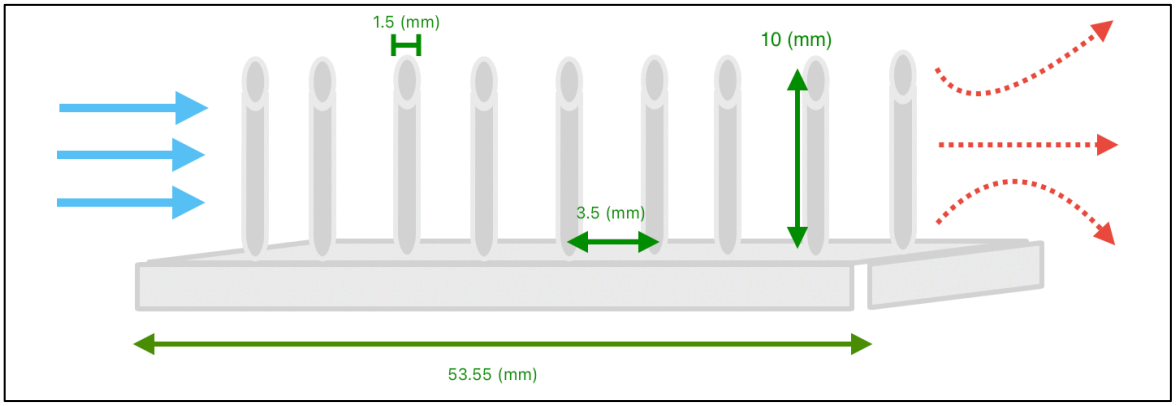

Figure 2.1 Schematic view of the 9-inline Pin-Fin test case

A scheme of the problem is presented on Figure 2-1. A Pin-Fin with 9 fins were studied. The height of the fins is h=10 (mm) and the radius of them is r=0.75 (mm), the distance between each fin is $d = 3.5\,mm.$ the length of the heatsink is $L = 53.55\,(mm)$. The considered material is Aluminum.

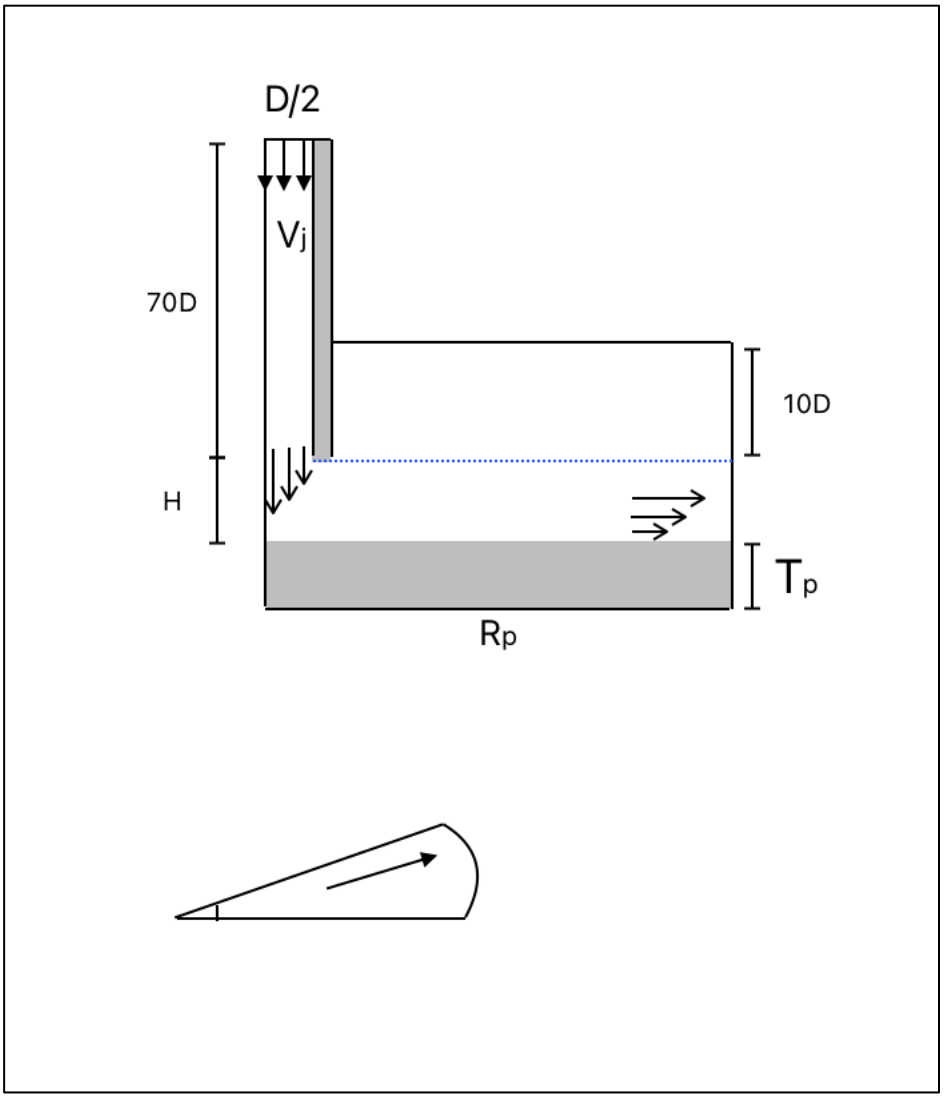

Figure 2.2 Scheme of the Computational Domain
for Zhang et al. (2019) Testcase.
front view(X-Z), and top view (X-Y)

Figure 2-2 shows the Scheme of the computational domain and variables which is used to discretize the mesh which will be expanded in mesh generation subsection.

2.3 The mathematical model

In this subsection, the mathematical model of the work will be presented. Starting with the governing equations, related mathematical variable will be discussed. Assumptions for each part of the work will be discussed. In the last sub-section, the boundary condition will be presented.

2.3.1 Governing equations

For the first part of the work the model is verified by a previous work by Zhang et al. (2019). G. Zhang et al. (2019) developed an improved Shear Stress Transport (SST) turbulence model to enhance the precision of simulating turbulent round jet impingement heat transfer. The enhancement incorporated a cross-diffusion correction in the turbulent kinetic energy (k) destruction term to address pressure gradient effects and the Kato-Launder correction in the production term for improved handling of stagnation regions. The model was used to simulate round jet impingement with different nozzle-to-plate spacings, and its accuracy was validated against experimental data and results from other established turbulence models such as the standard SST, k-ω, and combined RANS/LES models. The findings indicated that the improved SST model accurately predicted velocity, pressure, and heat transfer, particularly in regions sensitive to pressure gradients, effectively capturing complex flow structures near the stagnation point. This approach demonstrated the model's enhanced ability to accurately represent both the flow dynamics and thermal behavior of turbulent jet impingement scenarios.

The model is divided into two regions: the fluid and the solid regions. A conjugate heat transfer methodology exchanges the boundary conditions at the interface between the solid and the fluid.

For the fluid region, the incompressible Navier-Stokes equations are expressed in differential form as Economon (2020):

$$\Gamma \frac{\partial V}{\partial t} + \nabla . \bar{F}^{c}(V) - \nabla . \bar{F}^{v}(V, \nabla V) - S = 0 \tag{2.1}$$

where Γ is a preconditioning matrix, $\bar{v} = [u, v, w]^T$ is the flow velocity vector and the primitive variables are the static pressure, p, the velocity $\bar{v}$, and the Temperature is T.

$$V = \begin{bmatrix} p \\ \bar{v} \\ T \end{bmatrix} \tag{2.2}$$

S is a generic source term which is considered 0 for the current case study.

The convective flux,$\bar{F}^{c}(V)$, and the viscous fluxes, $\bar{F}^{v}(V, \nabla V)$ are:

$$F^{c} = \begin{pmatrix} \rho_a \, \bar{v} \\ \rho_a \, \bar{v} \otimes \bar{v} + \bar{I} \, p \rho_a \, c_p \, T \, \bar{v} \end{pmatrix} \tag{2.3}$$

Where ρ_a is the density, and $\bar{I}$ is the identity matrix. The viscous fluxes are:

$$F^{v} = \begin{pmatrix} \cdot \\ \bar{\tau} \\ k_a \nabla T \end{pmatrix} \tag{2.4}$$

$\bar{\tau}$ is the viscous stress tensor. The fluid is assumed to be Newtonian; therefore, the viscous stress tensor is:

$$\bar{\tau} = \mu_a (\nabla \bar{v} + \nabla \bar{v}^T) - \frac{2}{3} \mu_a \bar{I} \, (\nabla \cdot \bar{v}) \tag{2.5}$$

The pressure is decomposed into a dynamic pressure p and a thermodynamic pressure

P_o, constant in space.

The density is constant, therefore there is no equation of state to link the pressure, the density and the temperature. The dynamic viscosity, μ_d ,and conductivity are constant. The Prandtl number Pr_d is computed from the Prandtl definition:

$$Pr_d = \frac{\mu_d c_p}{k_d} \tag{2.6}$$

Considering the Boussinesq hypothesis and constant turbulent Prandtl number as Pr_t= 0.9, for the turbulent flow, the effective viscosity μ_a and the effective conductivity k_d include the effect of turbulence.

$$\mu_a = \mu_d + \mu_t \tag{2.7}$$

$$k_a = \frac{\mu_d c_p}{Pr_d} + \frac{\mu_t c_p}{Pr_t} \tag{2.8}$$

The Menter's Shear Stress Transport turbulence model (Menter et al., 2003) is the source of the turbulence viscosity.

For the **solid region**, the heat equation is:

$$\frac{\partial U}{\partial t} - \nabla . \bar{F}^v(U, \nabla U) - S = 0 \tag{2.9}$$

The conservative variable is $U = \left[\rho_s c_{ps} T\right]$, while ρ_s is the solid density, and c_{ps} is the specific heat of the solid. T is the temperature.

The viscous flux is:

$$F^v(U, \nabla U) = (k_s \nabla T) \tag{2.10}$$

In (2.10), k_s is the thermal conductivity of the solid. The source term S is set to zero.
Equation 2-1 to 2-10 were used for both the impinging test case and the pin fin heatsink.

Secondary quantities are computed from the primitive variables. For the heat transfer coefficient, we have:

$$h = \frac{Q}{(A_{hs}) \times (T_{hs} - T_{in})} \left[\frac{W}{(m^2.K)}\right] \tag{2.11}$$

Q is the heat dissipation in this part.
A_{hs} is the total heat transfer area of the heat sink. [m^2]
T_{hs} is the temperature at the heat sink base. [°K]
T_{in} is the temperature at the wind tunnel inlet. [°K]

For the thermal resistance:

$$R_{th} = \frac{1}{h \times A_{hs}} \left[\frac{K}{W}\right] \tag{2.12}$$

For the dimensionless pressure drop, we have:

$$\Delta p^* = \frac{\Delta P}{\left(\frac{1}{2}\right).\rho.\omega^2} \tag{2.13}$$

ΔP is the pressure drop between point 1 and point 2. [Pa]. Two internal planes are defined near x≈−50 and x≈153 mm to calculate average pressures, which are positioned close to the locations of experimental pressure taps.

ρ is the density of the air. [kg/m^3]

For the y^+ definition:

$$y^+ = \frac{y}{\nu u_\tau} \tag{2.14}$$

$$u_\tau = \sqrt{\frac{\tau_\omega}{\rho}} \tag{2.15}$$

$$\tau_\omega = c_f \times 0.5 \times \rho \times V_{ref}^2 \tag{2.16}$$

V_{ref} is the reference velocity. Which is defined as Inlet Velocity (V_j).

$$Re = \frac{\rho_a V_j D}{\mu_j} \tag{2.17}$$

For the heatsink, Reynolds number is calculated as:

$$Re = \frac{V_{ref} \times L}{\nu} \tag{2.21}$$

2.3.2 Assumptions

For the Impinging jet, the flows is incompressible air at T= 293.15 K. The constant density of air is $\rho_a = 1.2886\, kg/m^3$. The constant thermal conductivity is $k_a = 0.0269\, W.m^{-1}.K$. Constant molecular viscosity is $\mu = 1.953 \times 10^{-5}\, N.s/m^2$. The constant thermal

conductivity $k = 0.0269W/(m.K)$. Prandtl number is defined as $Pr = C_p\mu/k$. Both of steady and turbulent flows are modelled by RANS equations. For the Turbulent flow, the Prandtl number is constant, $Pr_t = 0.90$.
For the solid region, the material properties are constant. The density of the solid disk is $\rho_s = 7920\ kg/m^3$. The specific heat of $C_{p_s} = 900\ J.kg^{-1}.K^{-1}$. Thermal conductivity is $k_s = 201\ W.m^{-1}.K^{-1}$. The solid disk is heated from the bottom with the temperature of 303.15 K. Possible Radiation is ignored.

For the Pin Fin heatsink, For the 2D pin fin heatsink, because the conductivity of the solid is high compared to the air, the temperature is assumed to be constant in the fin. The effect of thermal conductivity is neglected, and no conjugate heat transfer procedure calculations are done. The parallel flow is incompressible air at T=293.15 K. The constant density of air is $\rho_a = 1.2886\ kg/m^3$. The constant thermal conductivity is $k_a = 0.0269\ W.m^{-1}.K$. Constant molecular viscosity is $\mu = 1.953 \times 10^{-5}\ N.s/m^2$. The constant thermal conductivity $k = 0.0269W/(m.K)$. Prandtl number is defined as $Pr = C_p\mu/k$. Both of steady and turbulent flows are modelled by RANS equations. Wall boundary conditions at isothermal T=303.15K, T=353.15K, T=403.15K are fixed

2.3.3 Boundary Condition and Computational Domain

For the first case, the impinging jet, Re =23000 and Re =70000 is considered. $D = 0.006\ m$ and the ratios of the D/H= 2 and D/H=6 were chosen to enable comparison the results with the numerical results of G. Zhang et al. (2019) and experimental results of Baughn et al. (1991). Figure 2.1 demonstrates the boundary condition that we have imposed. The entering constant velocity through the jet is $V_j = 55.13, 17.24(\frac{m}{s})$ and the temperature = 293.15 (K). Adiabatic walls are imposed on the pipe nozzle wall. Pressure inlet is applied to the open sidewalls of the air domain. If the flow exits the domain, the pressure inlet becomes a pressure outlet with a gauge pressure of 0 Pa. Otherwise, a total pressure of 0 Pa is applied with the velocity direction normal to the boundary. A dampening coefficient of 0.01 is applied at the pressure inlet to

ensure the convergence of solutions. Symmetry planes are used on the domain's front and rear sides. At the interface, temperature and heat flux data are exchanged with the solid solver, but flow velocity remains zero.

The solid solver uses an adiabatic boundary condition on the side and a constant temperature of 303.15 K on the bottom. Symmetry planes are used on the domain's front and rear sides. The interface exchanges temperature and heat flux data with the flow solver.

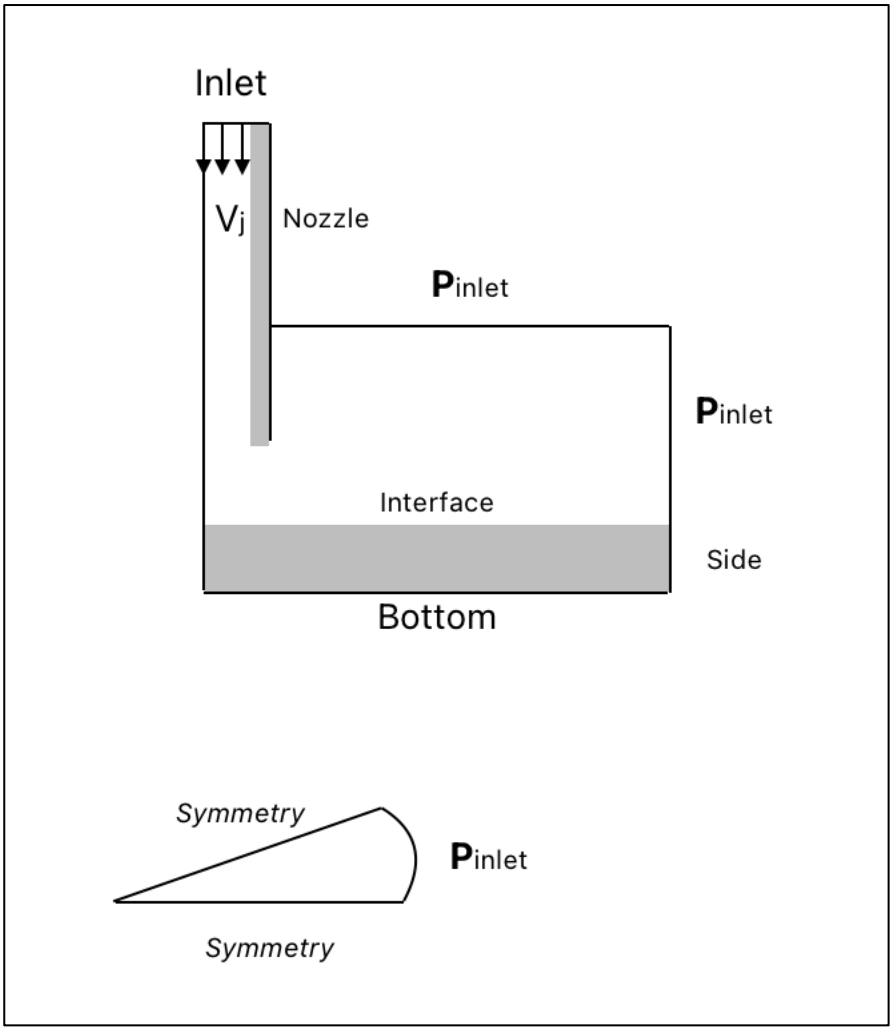

Figure 2.3 Scheme of the Boundary condition
for Zhang et al. (2019) Testcase.
Front view(X-Z), and top view (X-Y)

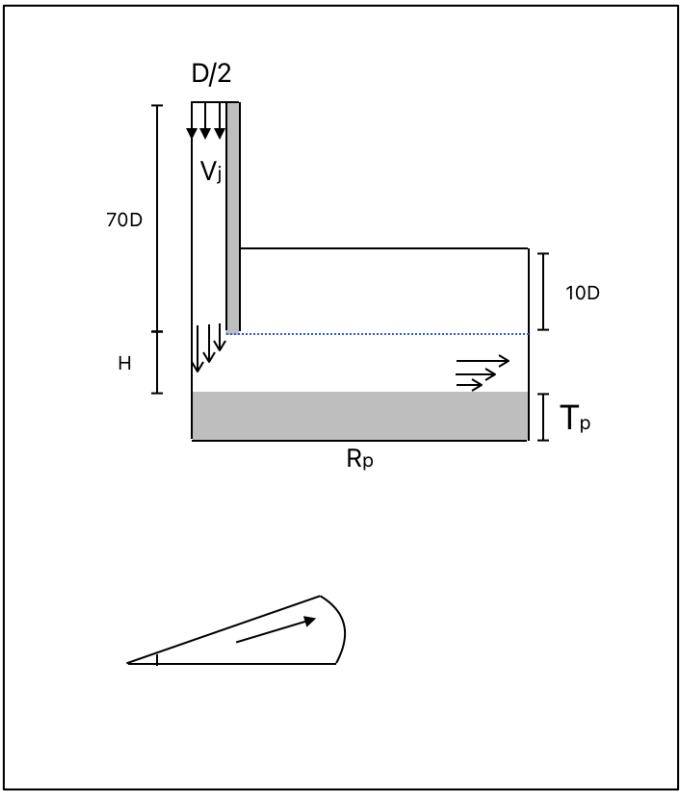

Figure 2.4 Scheme of the Computational Domain
for Zhang et al. (2019) Testcase.
front view(X-Z), and top view (X-Y)

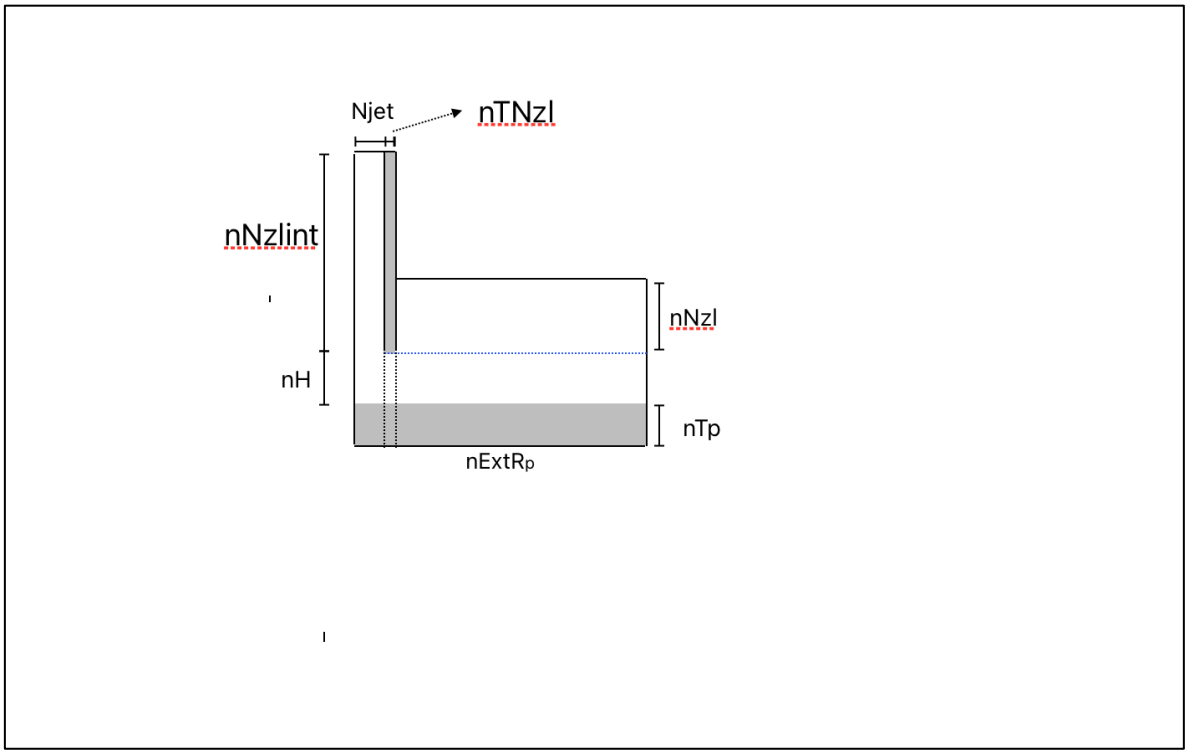

Figure 2.5 Variable names that define the number of nodes for the mesh generation: front view (X − Z plane)

For the second test case, the study involves a 2D inline pin-fin which consists of nine circular fins arranged in a row. The purpose of arranging them in a row with 8 numbers is to model them as infinite in the numerical case study. Figure (2-3) demonstrate the boundary condition of the 2D model. Isothermal wall conditions are applied at the surfaces of the cylinders. At the inlet, the flow has a constant temperature and velocity, consistent with the velocity profile. At the outlet, a constant pressure is specified. The top and bottom walls of the domain are treated as symmetry planes, while periodic boundary conditions are applied along the y-direction. Three isothermal boundary condition of T=303.15 °K, T=355.15 °K and T=403.15 °K is applied for the test case.

Two internal planes are defined near x≈−50 and x≈153 mm to calculate average pressures, which are positioned close to the locations of experimental pressure taps. The SU2_CFD software computes the average pressures on these planes, which are used to monitor the convergence of the simulation. The pressure drops across the cylinders is determined by the

difference between the upstream and downstream average pressures. These planes are solely utilized for post-processing purposes and do not influence the RANS equations.

Due to the symmetry boundary conditions, the fluid exhibits slip behavior along the top and bottom planes of the channel. In the 2D flow model, the flow remains uniform along the z-direction, so only a single mesh element with nodes on the bottom and top planes is needed in the z-direction. Figure (2.5) demonstrate the computational domain of 2D test case which was used to discretize the mesh.

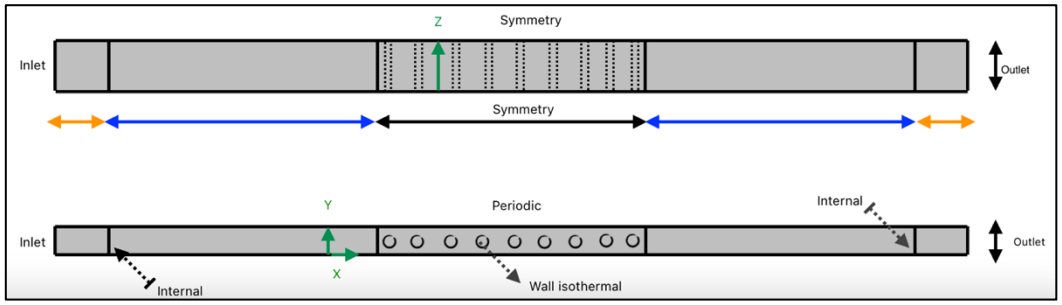

Figure 2.6 2D boundary conditions for the 9 in-line Pin-Fin

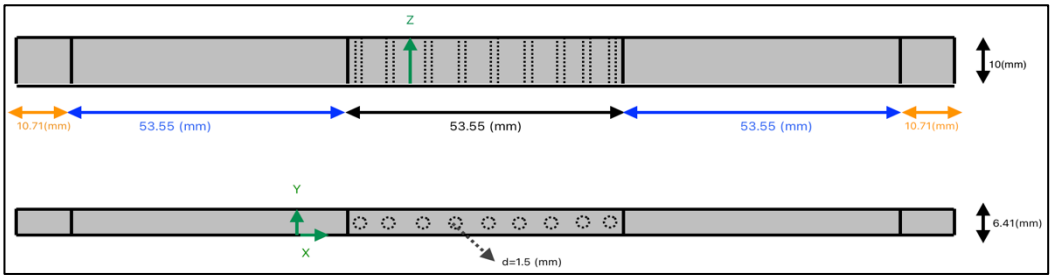

Figure 2.7 Computational Domain of the 9 in-line Pin-Fin

2.3.4 Mesh Generation

For the mesh discretization, GMSH (C. Geuzaine and J.-F. Remacle. Gmsh: a three-dimensional finite element mesh generator with built-in pre- and post-processing facilities. International Journal for Numerical Methods in Engineering 79(11), pp. 1309-1331, 2009.)is utilized.

For the first case of the work, transfinite algorithms are used to build the structured mesh, as

depicted in Figure 2-5, which shows the variable names used in the mesh generation script. The flow region is divided into five subregions, while the solid region is divided into three. Key parameters of interest include the number of nodes along the jet radius, denoted as *njet*; the number of nodes between the nozzle and the disk's top wall, represented as *nH*; and the total number of nodes along the disk's radius, given by the sum *njet* + *nTNzl* + *nExtRp*. A geometric progression is applied to accurately capture boundary layers and to ensure that the first grid nodes adjacent to the wall are positioned close enough, maintaining a $y+$ value of approximately 1 or less, which is crucial for the turbulence model. The number of nodes along the solid thickness—*nTNzl* for the pipe wall and *nTp* for the disk—are chosen to keep the growth ratio between elements in different regions below 1.2. Finally, the 2D regions are extruded by rotating them around the pipe axis to generate 3D elements in the angular direction, denoted by θ.

Table 2.1 shows the number of nodes in the different region, while Table 2.2 shows the growth rate for the elements. The number of nodes between each mesh doubles in the X and Z directions, resulting in a total of 4 nodes (2 × 2). The geometric progressions' growth ratio, r, is set so that the initial nodes in the fluid above the plate are decreased by a factor of two between the meshes. The size of the smallest element on a unit-length edge is determined by

$$a = \frac{r - 1}{r^n - 1} \tag{2.18}$$

n is the number of elements. While the mesh gets finer, the growth ratio is decreased, meaning that the mesh is more uniform. Figure 2.6 shows a simple view of the mesh.

Table 2.1 Number of the nodes for the different meshes

Mesh name	njet	nH	nExtRp	nTp	nNzl	nNzlint	nTNzl
xcoarse	25	37	32	5	10	35	7
coarse	50	75	65	11	20	70	15
medium	100	150	130	22	40	140	30
fine	200	300	260	44	80	280	60

Table 2.2 Number of the nodes for the different elements considering growth rate

Mesh name	rjet	rH	rExtRp	rTp	rNzl	rNzlint	rTNzl
xcoarse	1.22	1.24	1.26	1.0	0.84	0.93	1.0
coarse	1.10	1.11	1.12	1.0	0.97	0.975	1.0
medium	1.05	1.052	1.057	1.0	0.965	0.98	1.0
fine	1.025	1.025	1.028	1.0	0.975	0.99	1.0

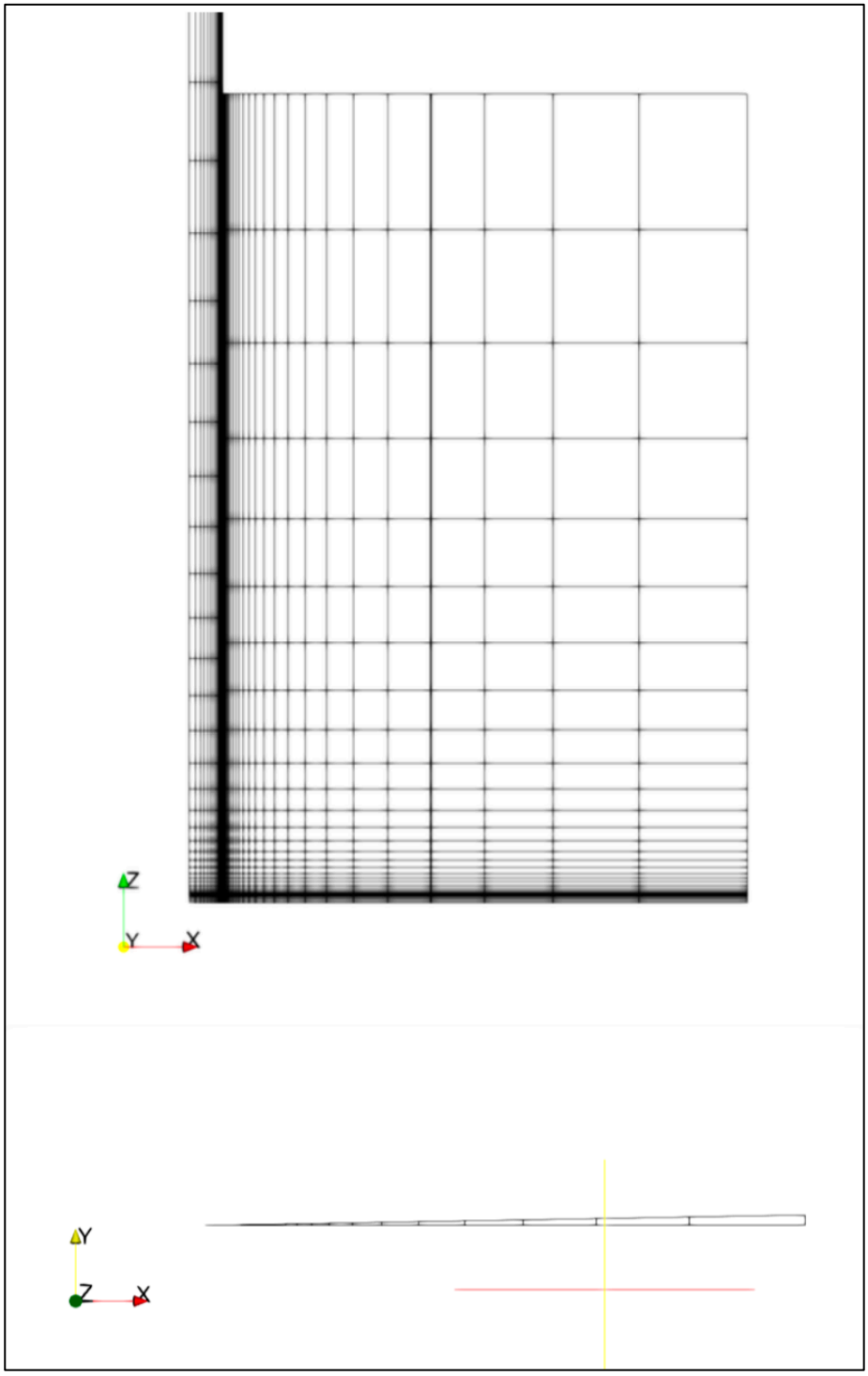

Figure 2.8 Example of mesh view for the coarse mesh:Top figure: y-view, Bottom figure: z-view

For the solid region, the number of nodes in the plate thickness direction is nTp = 5. One layer of elements is extruded in the angular direction.

For the inline Pin-Fin, the grid should be fine enough to represent the geometry's primary characteristics, particularly the round fins, as well as the momentum and thermal boundary layers. Two rules of thumb are frequently followed in the literature for the capture of the boundary layer.

The $y+$ value for the first node above the wall must be less than one for the RANS-SST model to be valid.

For a cylinder in cross flow, the angle between two grid nodes on the circumference should be between $\Delta\theta \approx 3°$ and $\Delta\theta \approx 2°$. DDES simulations employ a gap of around 1° between two in-line cylinders. A mesh analysis is required for the nine cylinders to determine the greatest angle that allows for accurate heat transfer prediction.

The division of the computational domain into structured and unstructured mesh region is demonstrated in Figure 2.7. Planes A, B, and C control the unstructured mesh size. Then, a zone of rectangular mesh elements is defined close to the fin, between d = 1.5(mm) and d = 1.875(mm). As shown in Figure 2.8 for three cylinders. The inner cylinder area, for d < 1.5 mm, is not meshed.

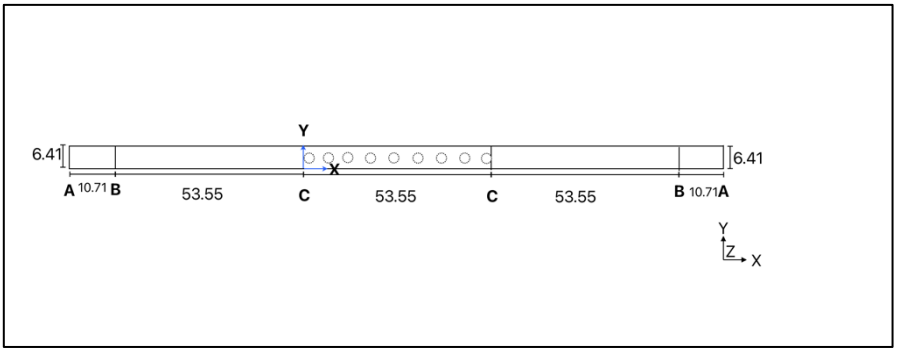

Figure 2.9 Unstructured 2D region dimension

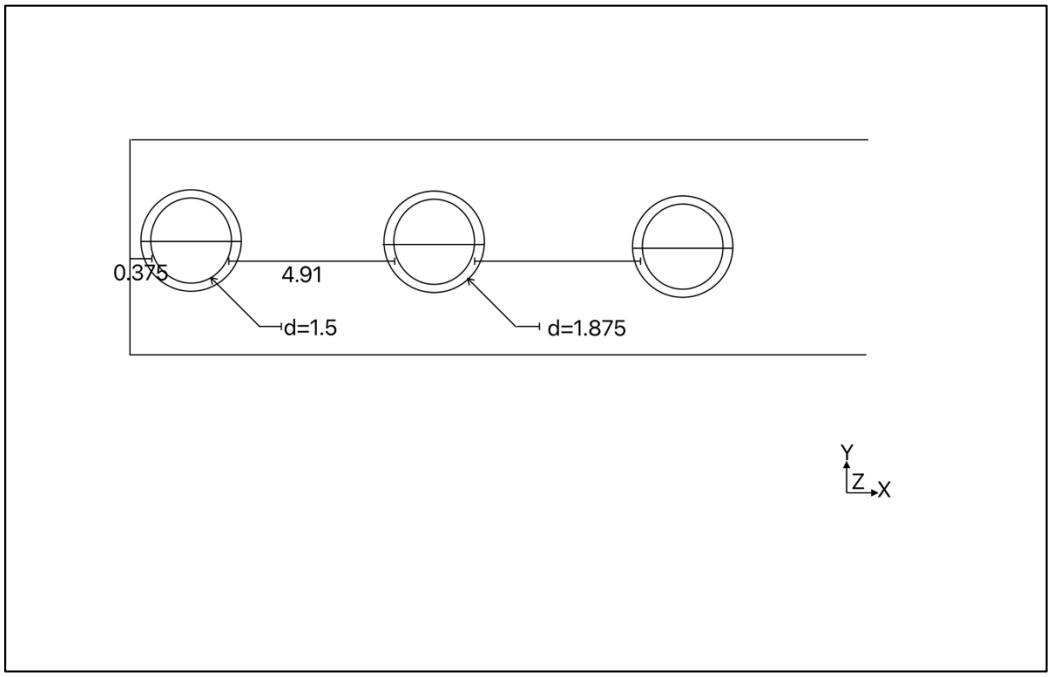

Figure 2.10 Structured 2D region dimension close to cylinder: zoom

Table 2.3 Number of nodes along the circle and radius in the structured area close to the fin wall

Mesh	n_r	$\Delta y_n(mm)$	n_c
1	18	0.00288	90
2	20	0.00213	128
3	23	0.00136	180
4	25	0.00102	154
5	28	0.000661	360

Table 2.4 Total number of nodes and elements in the mesh

Mesh	nodes	elements
1	71 078	34 770
2	130 682	64 239
3	243 050	119 963
4	449 460	222 522
5	847 058	420 394

Five different meshes are generated. n_c is the number of the nodes on the cylinder circumference and nr the number of nodes in the radial direction between d = 1.5mm and d = 1.875mm. A geometric distribution is used with a growth ratio of r=1/1.15. Table 2.3 shows the number of nodes along the radius, the size of the first element near to the cylinder Δy_n , and the number of nodes along the cylinder.

the size at plane A, B, and C are linked to the number of nodes on the circle n_c . At plane A, the element size is $10.1/n_c$. At planes B and C, the element size is $94.2/n_c$. Between the cylinders, plane A, B, and C, the mesh sizes vary linearly. Table 2.4 shows the number of nodes and element for each mesh. The Figure 2.9 shows the element distribution for the mesh 1. The Figure 2.10 and Figure 2.11 shows the elements in the structured area close to one fin.

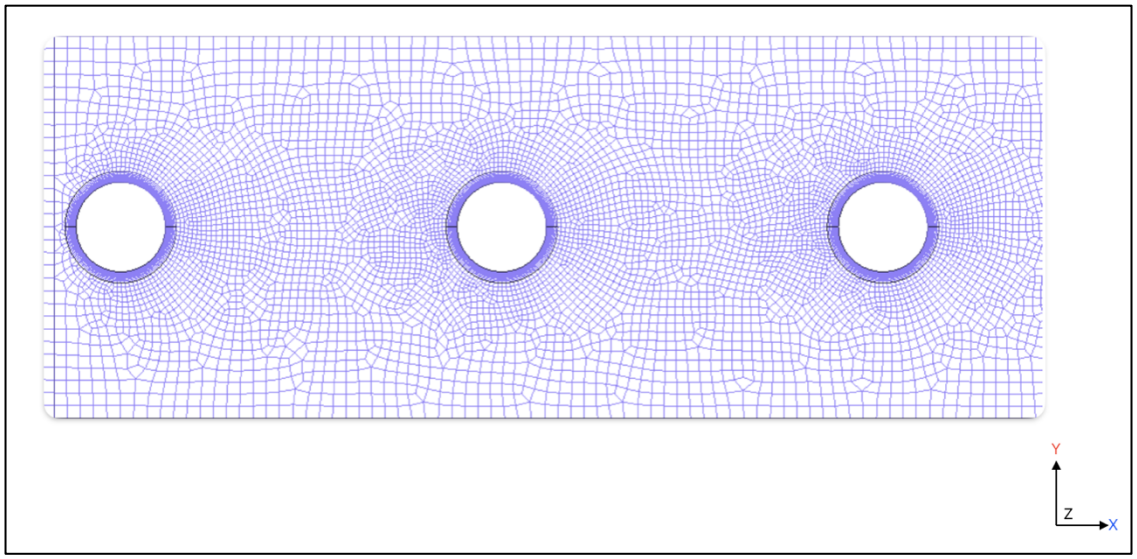

Figure 2.11 2D mesh around three cylinders

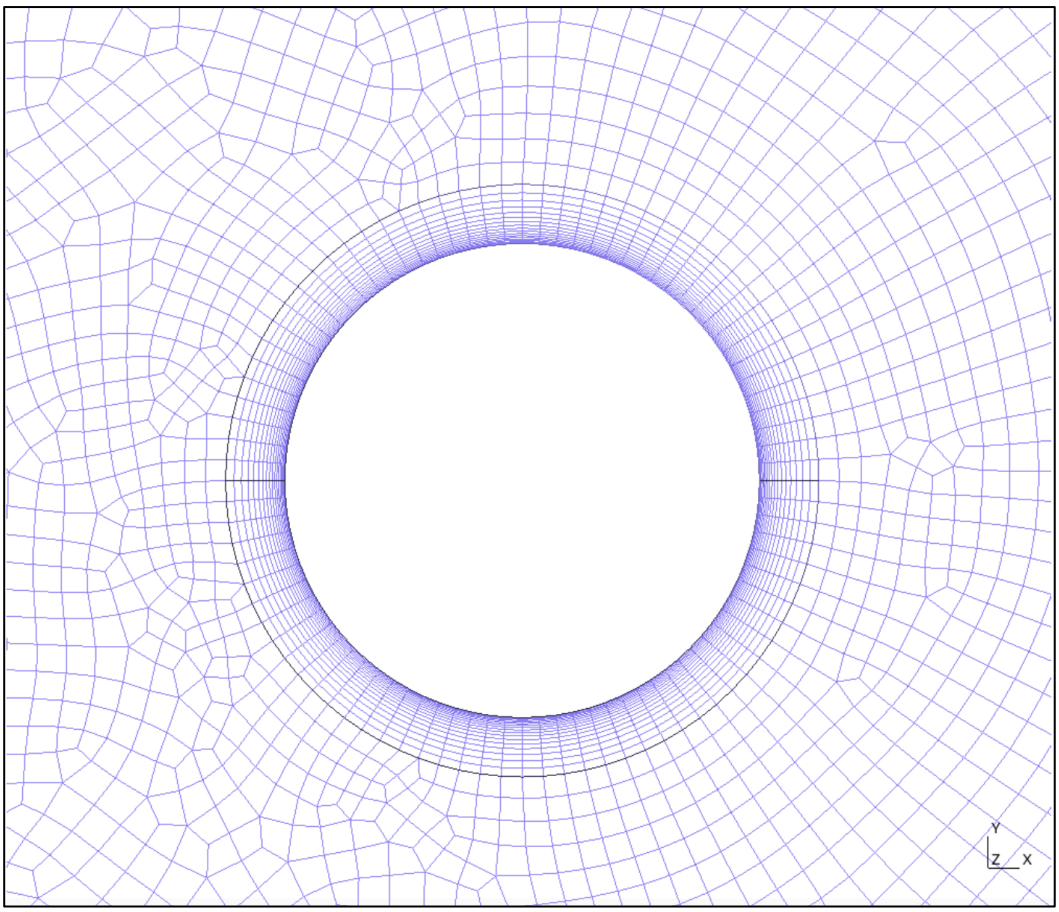

Figure 2.12 2D mesh around one cylinder

2.3.5 Numerical method

The incompressible RANS solver of SU2 is used to solve the system of equations. The equations are discretized in space with finite volume method (FVM) with a standard edge-based data structure on a dual grid with vertex-based schemes. The fluxes are evaluated at the midpoint of an edge.

The space numerical uses the FDS scheme for the RANS equations. The MUSCL scheme is used with a Venkatakrishnan slope-limiting method to have second order integration in space. For the viscous flows term the gradients are computed using the weighted least square theorem. For the turbulence equation, a scalar up-wind is used for the inviscid terms and a first order integration in space is used.

The problem is study unsteady. A first order time stepping approach is used with $\Delta t = 3 \times 10^{-5}$ for 200 000 time stepping. The time-numerical integration uses a Euler implicit method with a constant Courant-Friedrichs-Lewy number. The CFL number is set CFL= 40. The Flexible Generalized Residual Method FGMRES solves the resulting linear system of equations using LU-SGS preconditioning.

2.3.6 Simulation Set-up, Computational resources, post-processing path

In this project, the simulation calculation is done with SU2_CFD(Economon et al., 2016). For the computational study, the research was enabled by support from Ecole de technologie superieure (https://www.etsmtl.ca) and the Digital Research Alliance of Canada (alliancecan.ca).

2.4 Summary

This chapter described the mathematical modeling and numerical techniques used to simulate heat transfer in two configurations: a jet impinging on a heated plate and a pin-fin heatsinks.

The first case, based on the experimental work of Zhang et al. (2019), served as a validation study for the simulation setup. It uses the conjugate heat transfer (CHT) approach and the SST turbulence model to capture both fluid and solid heat transfer. The second case focused on a 2D model of a pin-fin heatsink inspired by Jonsson & Moshfegh (2001)experimental work.

Both simulations solved the incompressible Navier-Stokes and energy equations using SU2, an open-source CFD solver. The air was considered as an incompressible fluid with constant properties under steady-state conditions. For turbulence, the Shear Stress Transport (SST) model is applied, using a fixed turbulent Prandtl number of 0.9 to close the system of equations.

The jet impingement case utilized the CHT method, accounting for heat conduction in the solid domain, while the heatsink model simplified the solid as adiabatic due to aluminum's high thermal conductivity. In both cases, velocity inlets and pressure outlets are applied, along with isothermal wall conditions where needed. Symmetry boundaries are used to reduce the computational domain where appropriate. Mesh independence tests were carried out utilizing three mesh levels for the impinging jet and four to five mesh levels for the pin-fin heatsink.

Key output parameters include the local and average Nusselt number, thermal resistance, convective heat transfer coefficient, and pressure drop. The simulations are carried out on 3 to 6 computing nodes, using 64 parallel tasks. Depending on the mesh size and model complexity, total run times ranged from approximately 12 hours and 55 minutes to 24 hours.

CHAPTER 3

Numerical Results and Analysis

Introduction

Focusing on the thermal and fluid flow behaviour linked with an impinging jet and heatsink design, this chapter focus on pressure coefficients and wall heat transfer. The analysis starts with a comprehensive examination of the impinging jet case, which includes mesh sensitivity studies and the validation of Nusselt number and pressure coefficient results against established literature. The performance of various mesh densities for a pin-fin heatsink is then assessed under different Reynolds numbers using the SST turbulence model. The impact of mesh refinement on flow structures, heat transfer, and pressure losses is investigated using convergence histories, contour plots, and quantitative comparisons. Important performance parameters including pressure drop and thermal resistance are utilized to evaluate the simulations' accuracy and reliability.

3.1 Impinging Jet

In this section, the designed CFD model for the impinging airflow on the heatsink will be verified against Zhang et al. (2019). A comprehensive examination of fluid flow and heat transfer in an impinging jet configuration is part of the study. To guarantee numerical correctness and stability, convergence behaviour is first evaluated. The flow and thermal behaviour are then characterized by analyzing iso-contours of temperature, velocity, and turbulent viscosity close to the impingement point. A mesh sensitivity analysis is carried out by contrasting pressure coefficients and Nusselt numbers. The best turbulence model is chosen based on its predicted accuracy after numerical findings for pressure coefficients and Nusselt numbers are verified against current literature.

3.1.1 Convergence curves for test case: Re=23000, H/D=2, Time-Iterations:200,000

The study begins with an analysis of the logarithmic values of the residual for the pressure (P), temperature (T), and velocity components (U, V, W) as a function of outer iterations to assess numerical convergence. Figure 3.1 shows the residual for the coarse mesh after 200,000 time-iterations. Each RMS value decreases values indicating the overall solution convergence. While the pressure converges with minimal fluctuations, the convergence process of the temperature, in green, is slower. The behavior of the residual is similar for the medium and fine meshes. The fine mesh logarithmic values of the residual are plotted on Figure 3.2. After 200,000 iterations, the value of the pressure residual is around 10^{-12} and around 10^{-6} for the temperature. This is a drop of at least four orders of magnitude that lead us to believe that the solutions are converged.

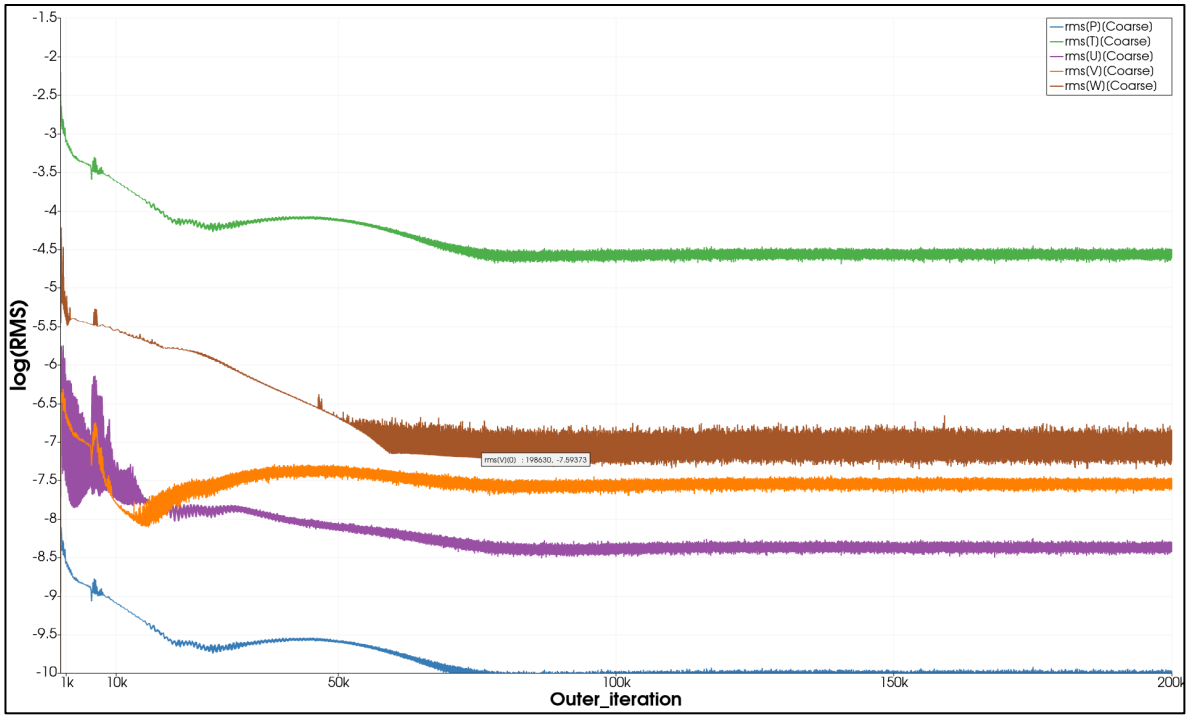

Figure 3.1 The logarithmic values of P, T, U, V, W based on Time iterations
Test case: Re=23000, H/D=2, Time-iterations:200,000, Coarse mesh
x-axis is the time-iterations, y-axis is the log (RMS)

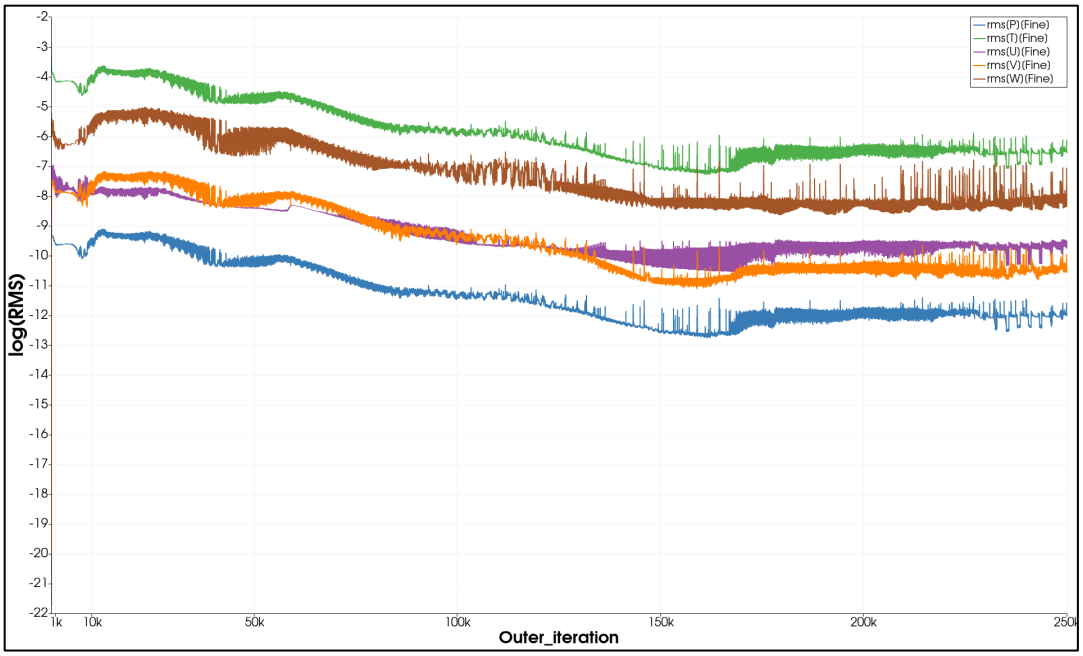

Figure 3.2 The logarithmic values of P, T, U, V, W based on Time iterations
Test case: Re=23000, H/D=2, Time-iterations:250,000, Fine mesh.
x-axis is the time-iterations, y-axis is the log (RMS)

To assess further the convergence of the solution, the turbulent kinetic energy (k) and the dissipation rate (ω) were studied. Figure 3.3 shows the behavior of the k and ω for the coarse mesh after 200,000 time-iterations. ω shows significant oscillations specially between 50,000 to 120,000 iterations. Meanwhile, k decreases more regularly. Figure 3-4 shows the behavior of k, and ω for the fine mesh. k shows the smoothest behavior compared to the coarse mesh and reaches to the lowest value of -11.9. ω still demonstrates notable fluctuations before 100,000 iterations but shows better convergence compared to the coarse meshes.

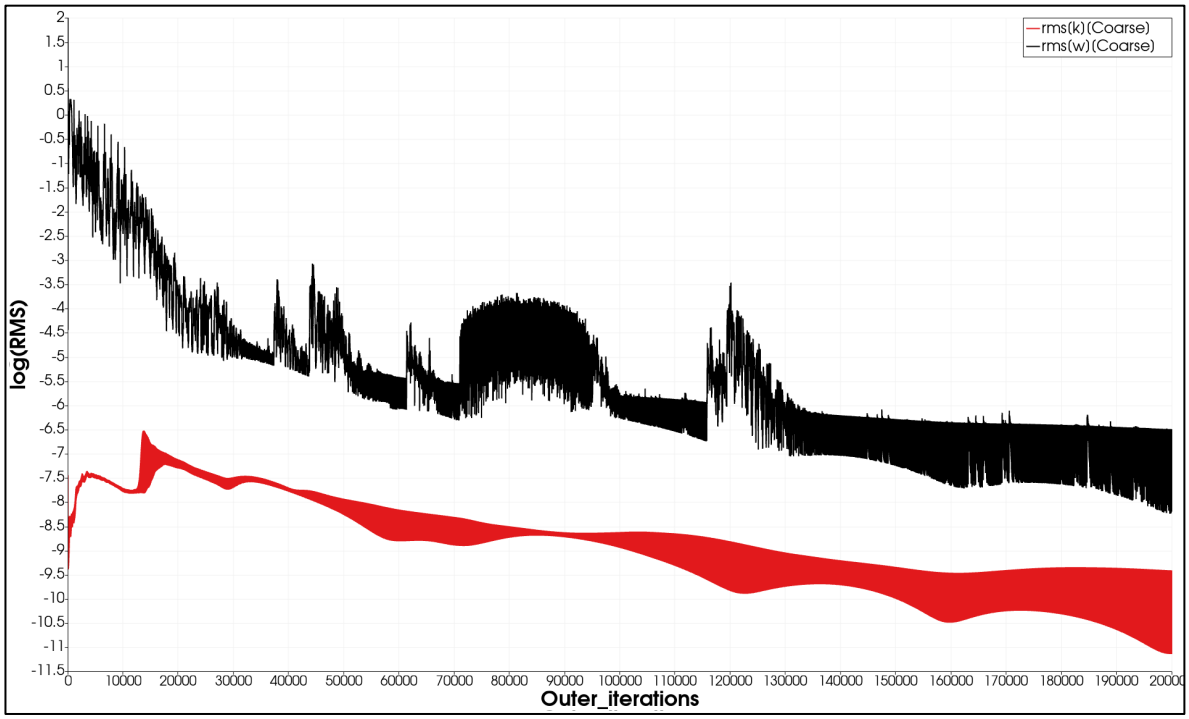

Figure 3.3 The logarithmic values of k, ω based on Time iterations
Test case: Re=23000, H/D=2, Time-iterations:200,000, Coarse mesh
x-axis is the time-iterations, y-axis is the log (RMS)

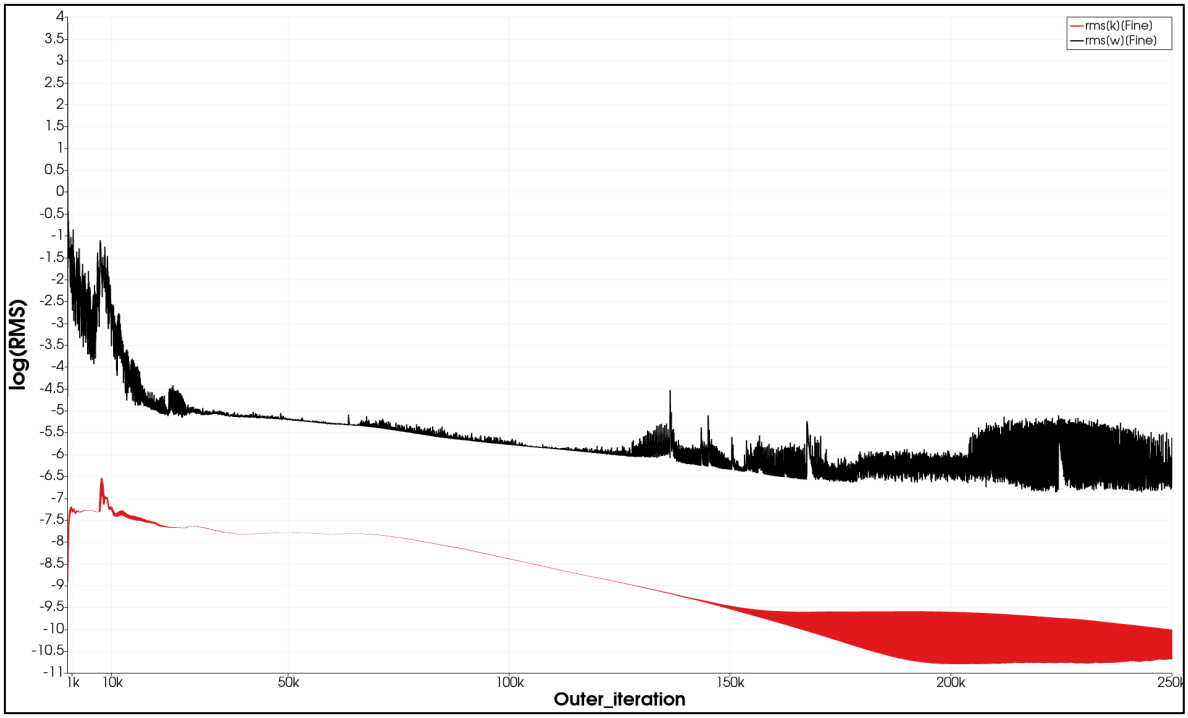

Figure 3.4The logarithmic values of k, ω based on Time iterations
Test case: Re=23000, H/D=2, Time-iterations:250,000, Fine mesh
x-axis is the time-iterations, y-axis is the log (RMS)

To study the convergence of the model in the solid region, the logarithmic values of the temperature residual in the solid zone for each mesh were studied. Figure 3.5 shows the values of the temperature residual after 200,000 time-iterations for the coarse mesh. While the value decreases gradually from -0.7 to -10.9, there are visible oscillations before 30,000 iterations. Figure 3-9 illustrates the residual of the solid temperature for the fine mesh. The fluctuations are smaller than for the coarse mesh. The residual temperature decreases smoothly after 170,000 iterations.

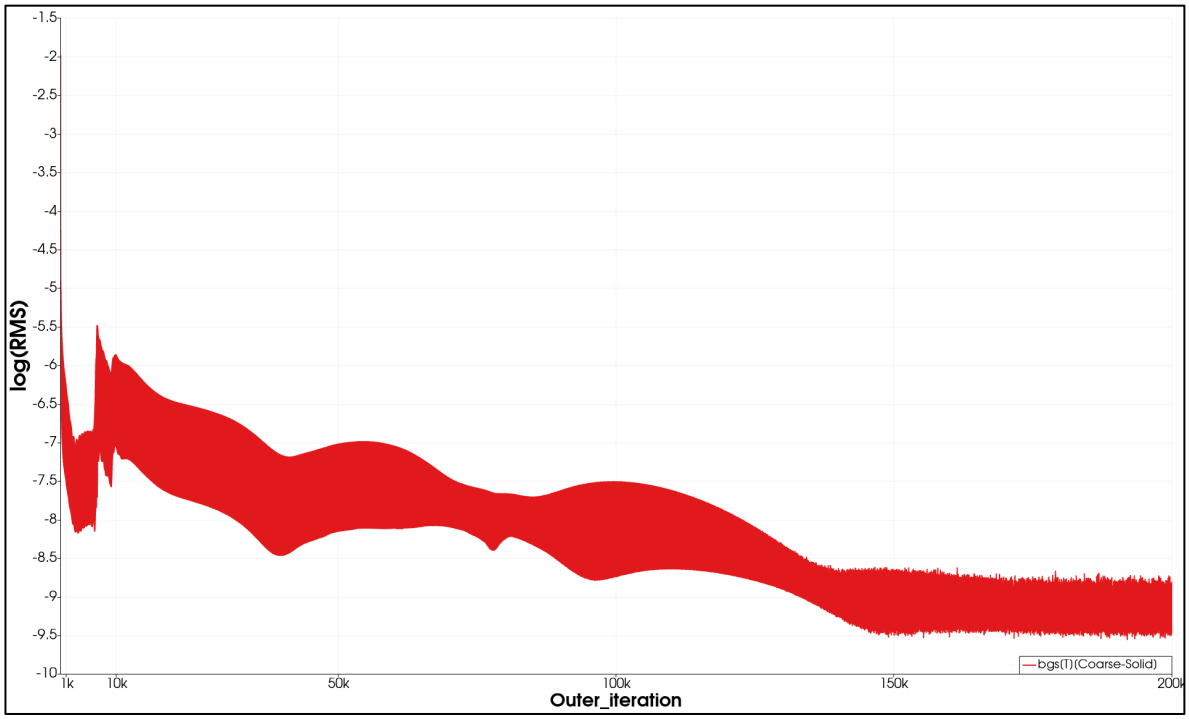

Figure 3.5 The logarithmic values of Temperature of the solid zone based on Time iterations. Testcase: Re=23000, H/D=2, Time-iterations:200,000, Coarse mesh
x-axis is the time-iterations, y-axis is the log (RMS)

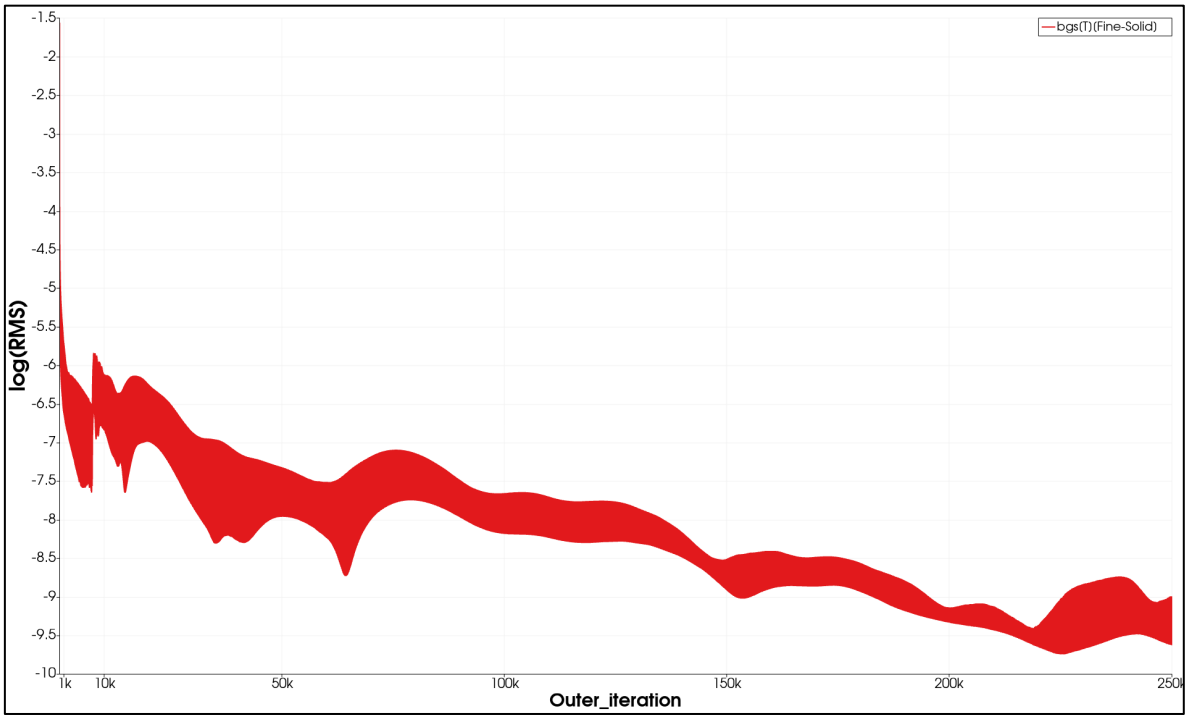

Figure 3.6 The logarithmic values of Temperature of the solid zone based on Time iterations
Testcase: Re=23000, H/D=2, Time-iterations:250,000, Fine mesh
x-axis is the time-iterations, y-axis is the log (RMS)

3.1.2 Isocontour of the Velocity and Turbulent Viscosity for Coarse, Medium, Fine meshes.

The contour of the velocity and turbulent viscosity for the course, medium, and fine meshes for the test case: Re=23000, H/D=2, at time-iterations:200,000 are plotted in this section. After 200,000 time steps, the solution is considered steady.

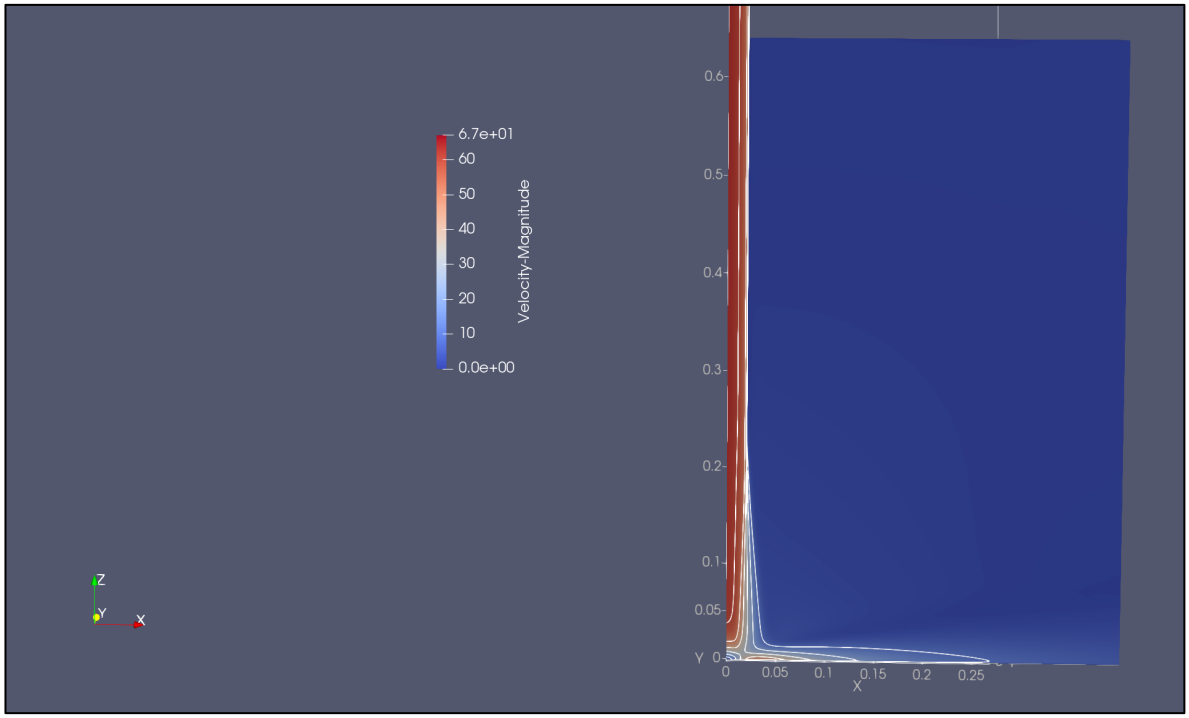

Figure 3.7 Isocontour of the Velocity Magnitude close to the Stagnation Point for the test case: Re=23000, H/D=2, Time-iterations:200,000, Medium mesh

Figure 3.7 shows the contour of the velocity magnitude close the stagnation point. The velocity magnitude slightly increases along the z axis after getting of the nozzle, until it reaches 43 m/s. Then, it starts slowing down toward the stagnation point. At the stagnation point, the velocity vector changes direction and aligned with the bottom plate. It accelerates along the bottom plate until it reaches a maximum value and decelerate again. The results are very similar for the coarse, medium and fine meshes, thus only the medium mesh results are presented for the velocity.

Figure 3.8 shows the turbulent viscosity for the test case close the stagnation point. The highest value, 0.0046 for the Medium mesh, was observed close the stagnation point. This highest value is in the region where the radial jet boundary crosses the edge of the bottom wall boundary layer. Close to the nozzle exit, effects of the thin nozzle wall are visible.

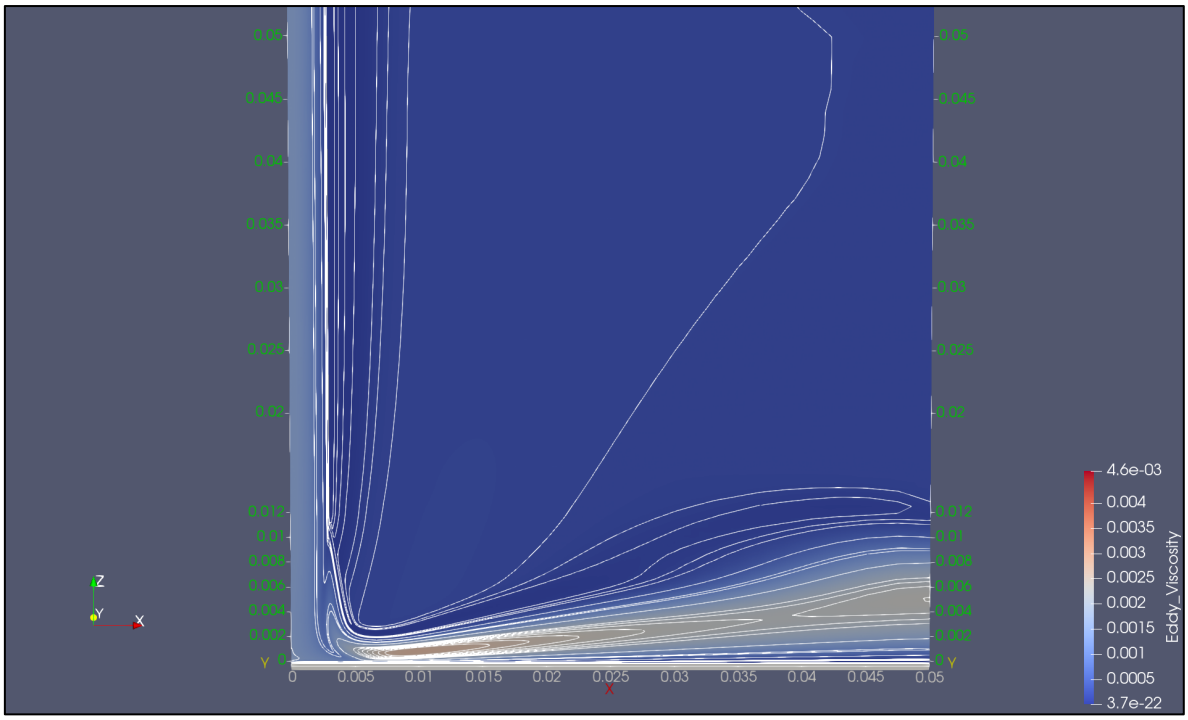

Figure 3.8Turbulent Viscosity at the Stagnation Point For the testcase: Re=23000, H/D=2, Time-iterations:200,000, Medium mesh

3.1.3 Mesh study for the Nusselt Number and Pressure Coefficient

Impinging jet are often used for the cooling of heat sink in electronic application. The quantities of interest for this test case are the heat transfer coefficient, in dimensionless form $Nu/(Re^{2/3})$ and the pressure coefficient. Figure 3-9 shows the values of the $Nu/(Re^{2/3})$ based as a function of r/D for different meshes. The highest value is between 0.22 and 0.23 and there is a secondary peak before r/D=2. The xcoarse predictions have large discrepancies with the coarse, medium, and fine mesh results. Results are particularly sensitive to the mesh size close to the stagnation point, r/D=0. The values evolve rapidly along the x-axis, in a range between 0.18 and 0.225. As these discrepancies are local, they have a small impact on the overall heat transfer.

Figure 3.10 compares the pressure coefficients for different meshes for the impinging jet test case. Results agree, except close to the stagnation point. The pressure coefficient goes from 1.37 for the xcoarse mesh to 1.46 for the fine mesh. In theory, the pressure should be maximum at r/D=0, however, the fine mesh experiences an unexpected slight increase just after r/D=0. It may be a spurious effect caused by the numerical scheme. For the most part of the region of interest, the pressure coefficients are in close agreement, even for the Xcoarse mesh.

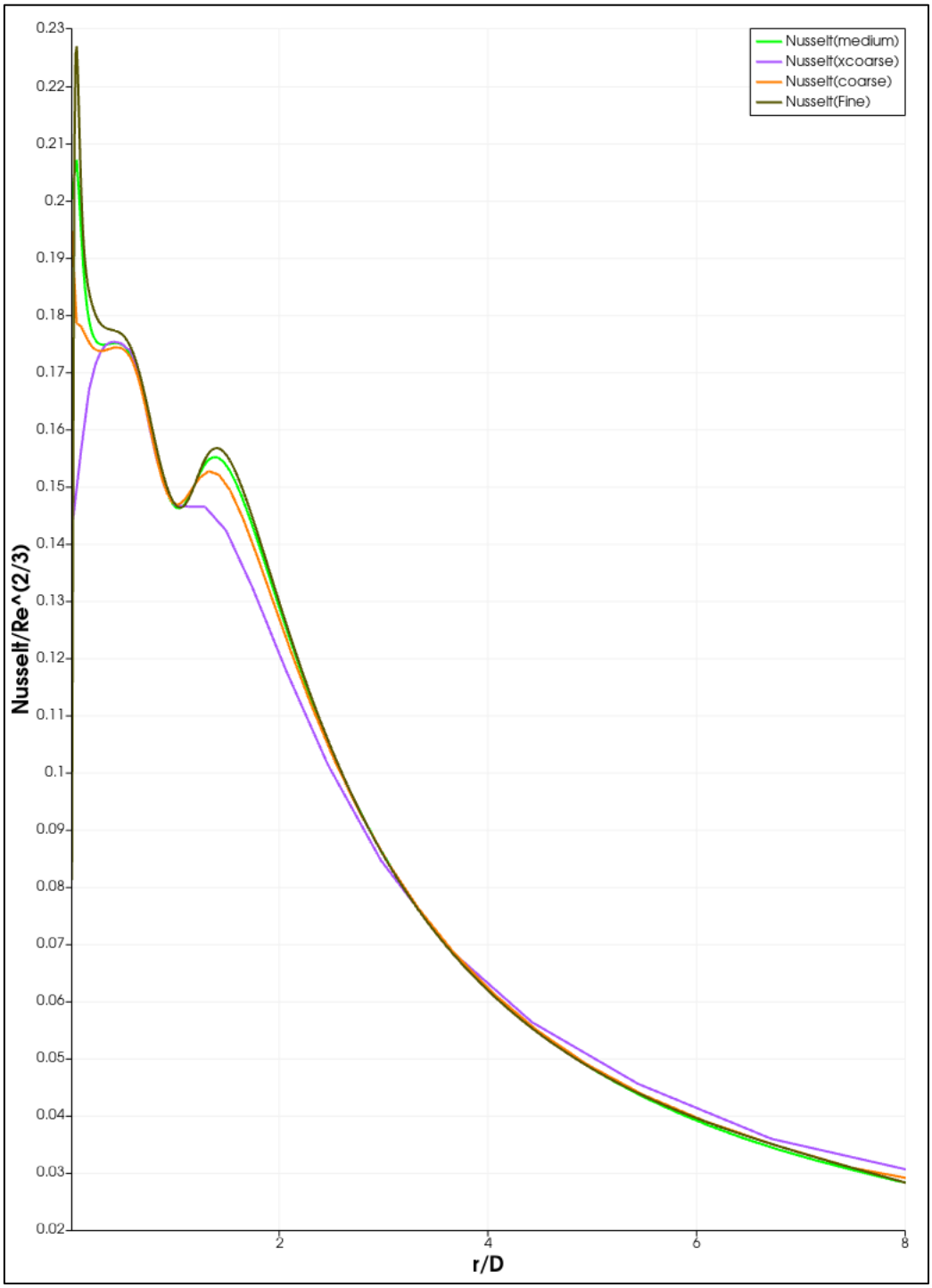

Figure 3.9 Comparison of the Nusselt Numbers for Four Meshes:
Xcoarse, Coarse, Medium, Fine. For the test case:
Re=23000, H/D=2, Time-iterations:200,000
x-axis is r/D and y-axis is Nusselt Number divided by $Re^{2/3}$

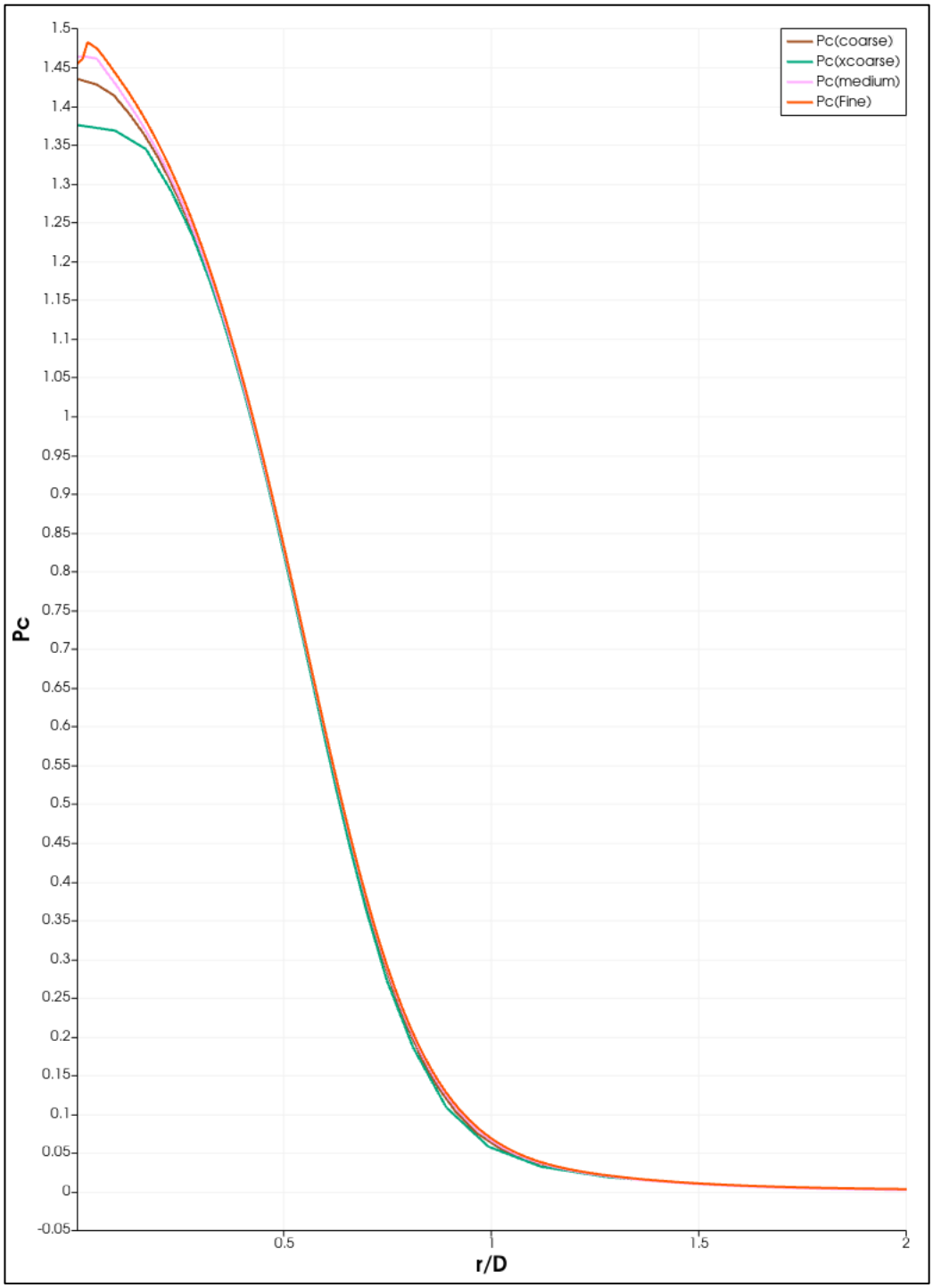

Figure 3.10 Comparison of the pressure coefficient (pc) for four meshes: Xcoarse, Coarse, Medium, Fine. For the test case: Re=23000, H/D=2, Time-iterations:200,000.
x-axis is r/D and y-axis is pressure coefficients

3.1.4 Comparison of the Nusselt number and Pressure Coefficient with the Literature

The results of SU2 will be compared to the available results from G. Zhang et al. (2019) and Huang et al. (2021) . Pressure coefficients and Nusselt numbers along the bottom plate will be compared for each model. Zhang et al. (2019) results are for the same geometry but with H/D=6. Figure 3-11 compares the SU2 results to the G. Zhang et al. (2019) for the pressure coefficient. At r/D=0, the pressure coefficient of the coarse mesh is 1.33. Note that the average velocity at the nozzle exit is used as the reference velocity. As the centerline velocity is around 1.2 time larger than the average velocity, the pressure coefficient base on the centerline velocity become 0.92. Zhang et al. (2019) have tested several turbulence models, and the values are around 1.1. at r/D=0, but they also report a value of 1.2 from previous experiments.

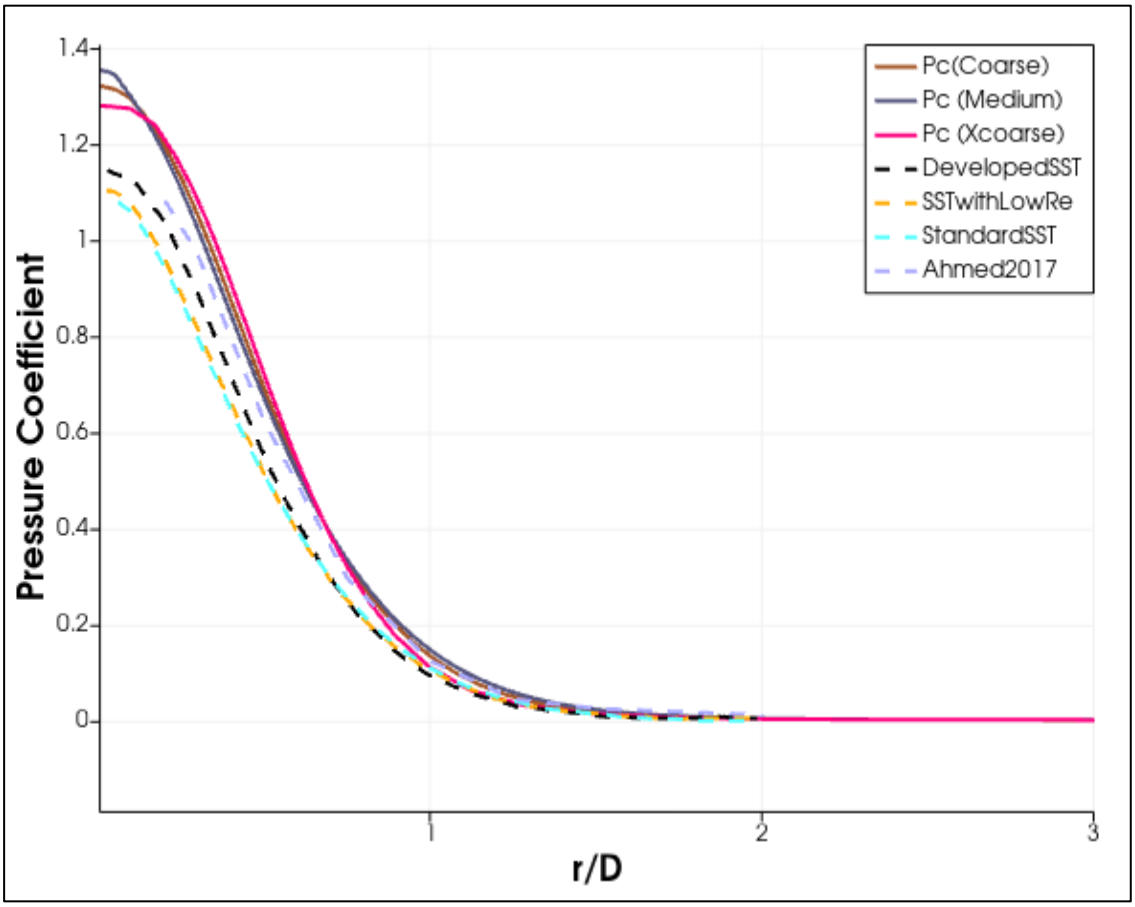

Figure 3.11 Comparison of the pressure coefficient (Pc) as a function of r/D between the SU2 results for Xcoarse, Coarse, and Medium meshes and G. Zhang et al. (2019) for Re=23 000 at H/D=6

Figure 3.12 displays the comparison of the results between SU2 and G. Zhang et al. (2019) for $Nu/(Re^{2/3})$. While SU2 results are lower than most literature results at stagnation point, there is a large discrepancy between the different results from the literature.

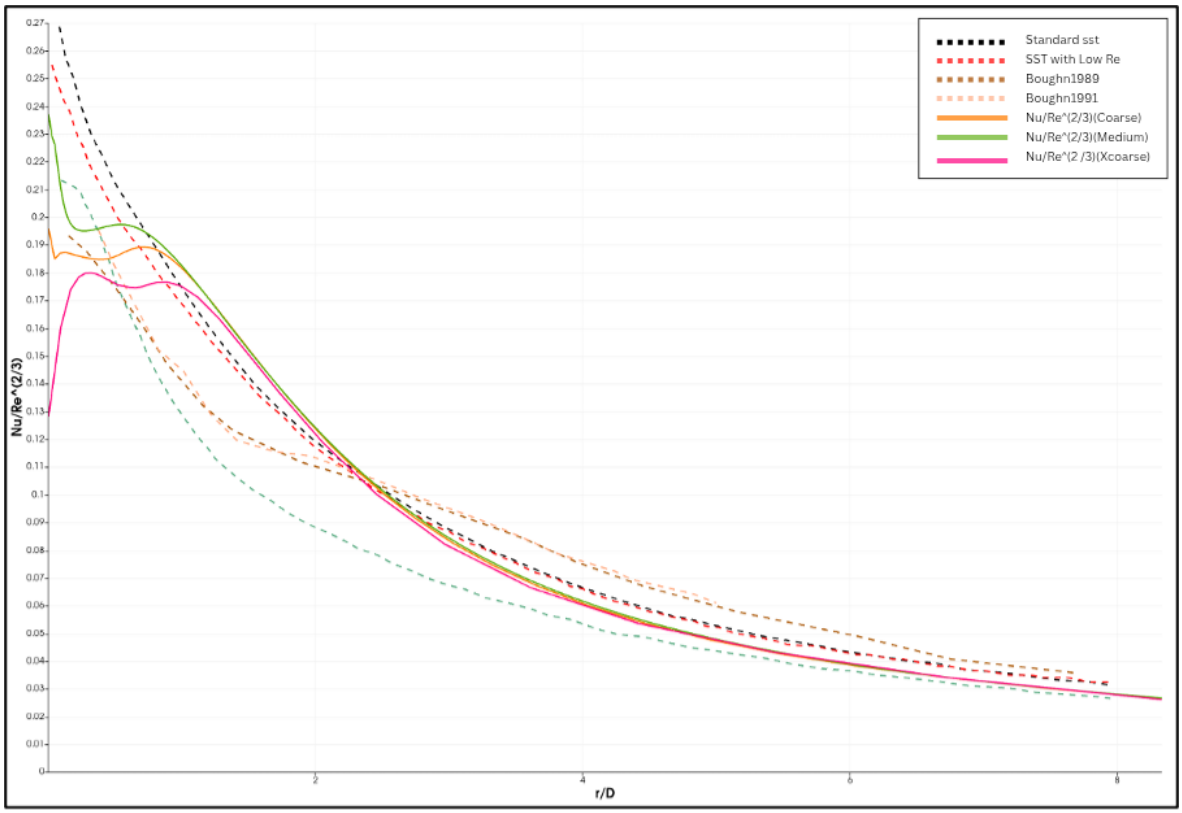

Figure 3.12 Comparison of the Nusselt Numbers as a function of r/D for the Xcoarse, Coarse, Medium meshes with the results from Zhang et al. (2019)

Results are also compared to Huang et al. (2021) for H/D=2. Figure 3-13 shows the comparison for three different meshes from Coarse to Fine for the pressure coefficient as a function of r/D. The SU2 results covers the Huang results for r/D above 0.25. Although, the Fine mesh had a peak value of 1.48 at stagnation points, it is close to the 1.4 value of the literature.

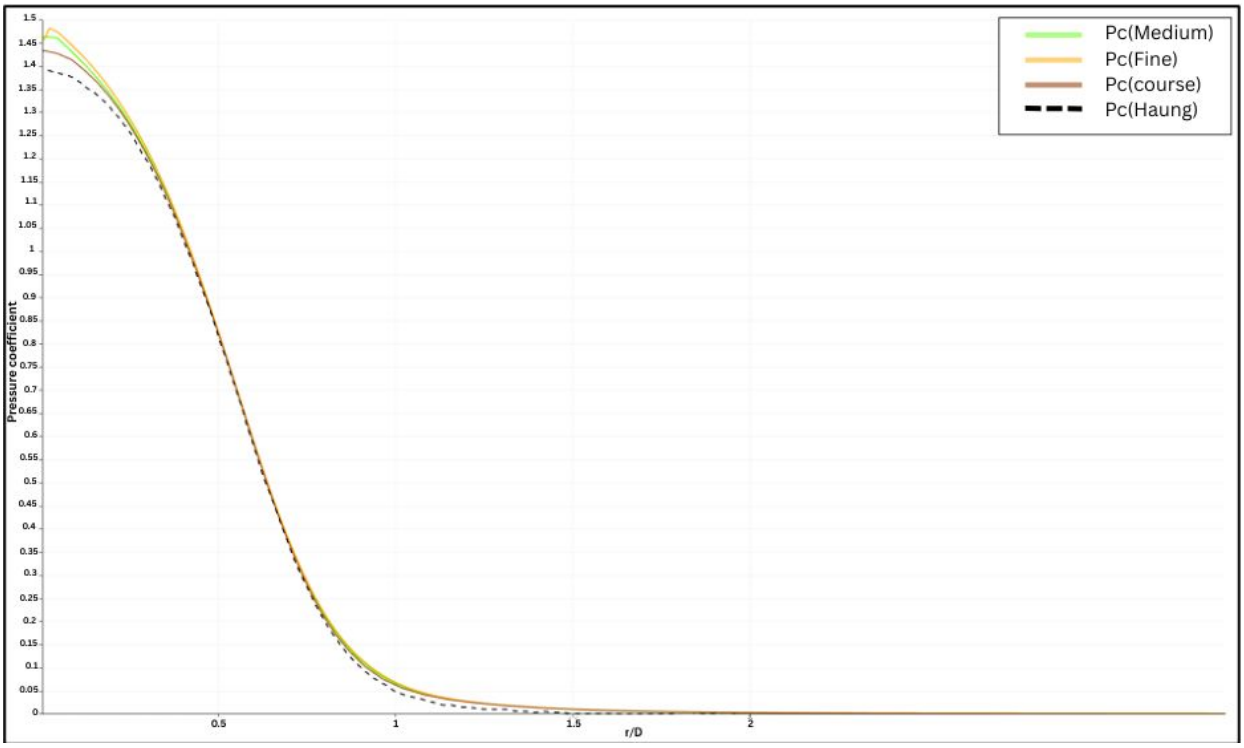

Figure 3.13 Comparison of the pressure coefficient as a function of r/D for the Coarse, Medium and Fine meshes with the results of Huang et al. (2021) for Re=23000

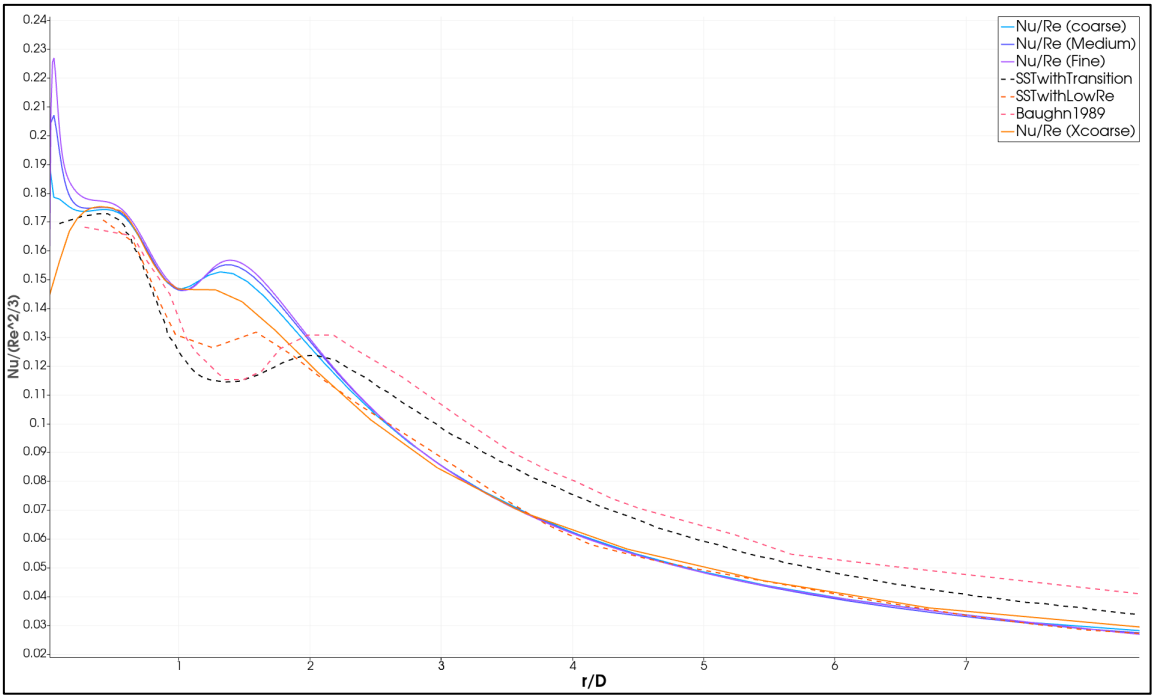

Figure 3.14 Comparison of Nu/(Re^2/3) as a function of r/D for results of three different meshes to Huang et al. (2021) For Re=23000

Figure 3.14 compares the normalized Nusselt number Nu/(Re^2/3) as a function of the radial position (r/D) for different mesh resolutions and turbulence models. The Fine, Medium, and Coarse meshes show similar trends with slight variations in peak magnitude and secondary bumps, indicating mesh independence is mostly achieved. Overall, the fine mesh aligns well with Huang et al. (2021) and captures detailed features of the heat transfer profile more consistently than coarser meshes or some turbulence models.

In this section, the behavior of the flow and temperature in the solid region were verified. The pressure coefficients and Nusselt numbers were compared to the chosen literature to validate the model.

3.2 2D inline pin-fin

3.2.1 2D mesh results for various Reynolds numbers and isothermal conditions

The 2D model consists of 9 inline circular pin fins placed inside a rectangular frame which are subjected to a parallel airflow. The inlet air flow is constant. The behaviour of the 2D meshes will be studied for different Reynolds numbers and temperature conditions. The inlet temperature is fixed at 293.15 °C, and two different isothermal conditions for the Standard SST model and 3 isothermal conditions for the SST2003 and Spalart Allmaras models are studied. The pressure drop and thermal resistance will be compared to each to other. In the final part, the CFD result will be compared to the chosen literature.

Table 3.1 shows the different meshes and boundary conditions used for the parallel flow over inline pin-fins. Three turbulence models: Standard SST, SST2003 and Spalart Allmaras for different isothermal temperature conditions, Reynolds numbers and mesh are studied.

Table 3.1 Models, isothermal conditions,
Reynolds numbers, and meshes for the 2D inline pin-fin
for the inlet temperature of T=293.15 °C.

Model	Isothermal Condition	Reynolds Numbers	Meshes
Standard SST	T=303 °C T=403 °C	Re=4000 Re=6000 Re=10000 Re=12400	Xcoarse Coarse Medium Fine Xfine
SST2003	T=303 °C T=353 °C T=403 °C	Re=4000 Re=6000 Re=10000 Re=12400	Xcoarse Coarse Medium Fine Xfine
Spalart Allmaras	T=303 °C T=353 °C T=403 °C	Re=4000 Re=6000 Re=10000 Re=12400	Xcoarse Coarse Medium Fine Xfine

3.2.2 Convergence Curves for the SSTV2003 model for the testcase Re=6000, Isothermal= 403℃

The log of the residual evolution with time for multiple values: pressure, temperature, velocity component, kinetic turbulent energy and ω for the test case: Re=6000, isothermal=403 ℃ , are presented in the first section of this study. The residual evolutions are similar for the different meshes, thus only the fine mesh results are presented. The Figure 3.15 shows the logarithm of the RMS residual values of pressure, temperature and velocity for the fine mesh test case. The main flow is in the U direction. Since the flow is 2D, with only one mesh element in the z-direction, there is no flow in the z-direction. After an increase of residual values before 35000 iterations, the values stabilize around a steady state. Since the flow is unsteady with vortex shedding around the cylinder, the residual of the pressure and temperature oscillate cyclically.

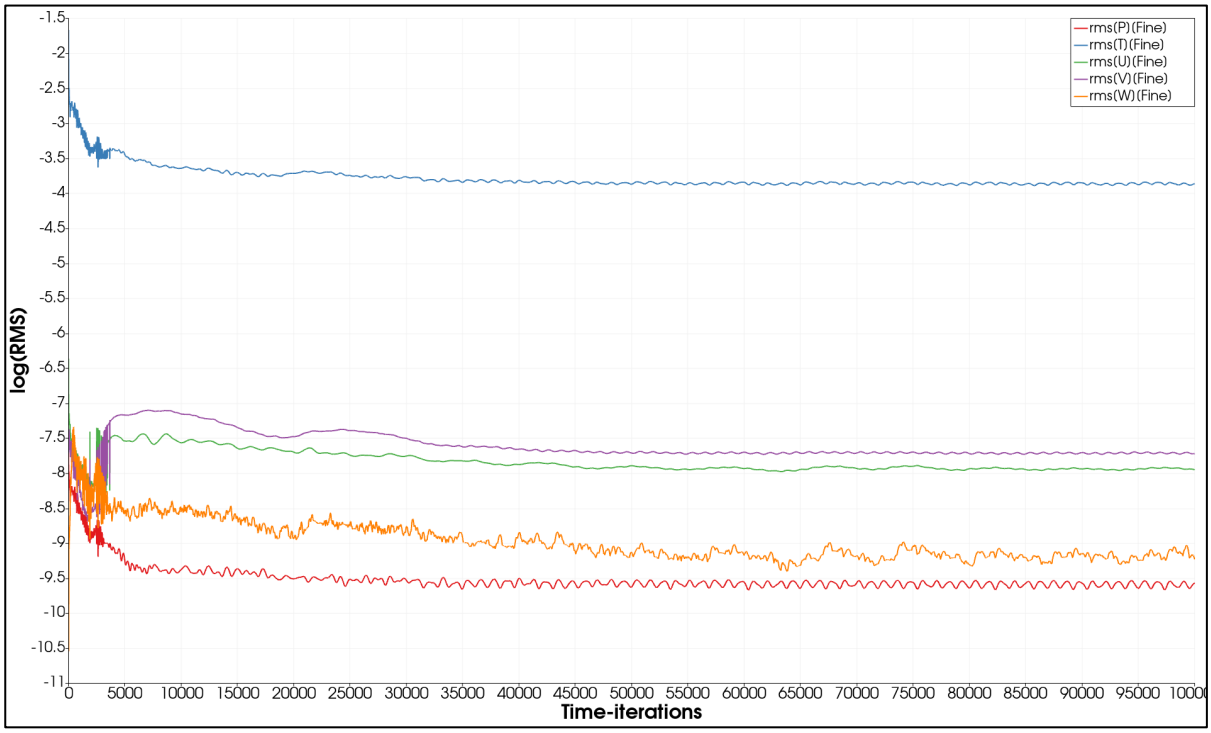

Figure 3.15 The log (RMS) of P, T, U, V, W with time iteration: SST2003V, Isothermal temperature 403 °C, for Re=6000, Fine Mesh

Figure 3.16 shows the logarithm of the residual RMS values of k and ω for the fine mesh. Although the RMS k values show an almost constant value after an observable fluctuation before 10000 iterations, cyclic oscillations of the RMS ω can be observed. This is expected since vortices are shed cyclically after the initial transitional state.

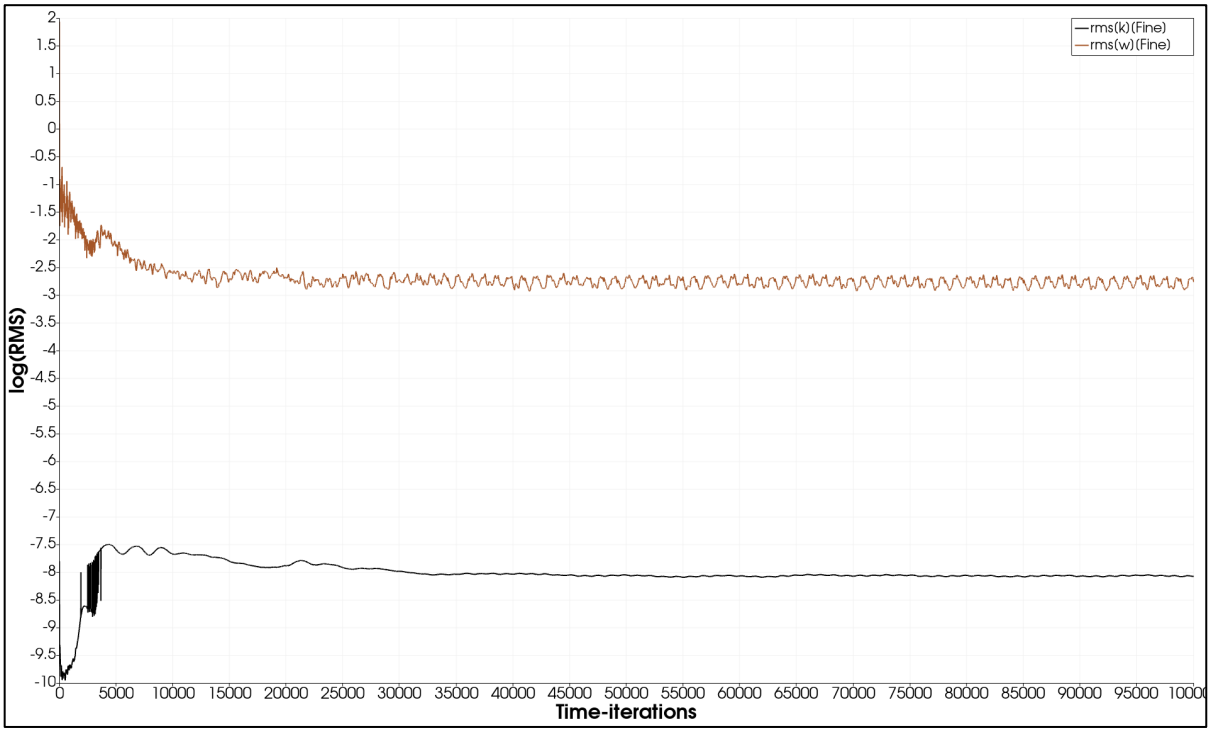

Figure 3.16 The log (RMS) of k, and ω with time iteration:
SST2003V, Isothermal temperature 403 °C, for Re=6000, Fine Mesh

3.2.3 Isocontour of Velocity, Temperature and Turbulent Viscosity

The isocontour of velocity, temperature and turbulent viscosity for the test case: Re=6000, Isothermal=403 °C, SST model will be shown in this section. Figures 3.17 shows the contours of the velocity magnitude for the 2D flow around the cylinder of the heat sink. The flow is from right to left. By refining the mesh, the path of the cooling air between the fins are straighter, although the Fine and Xfine meshes does not show notable difference.

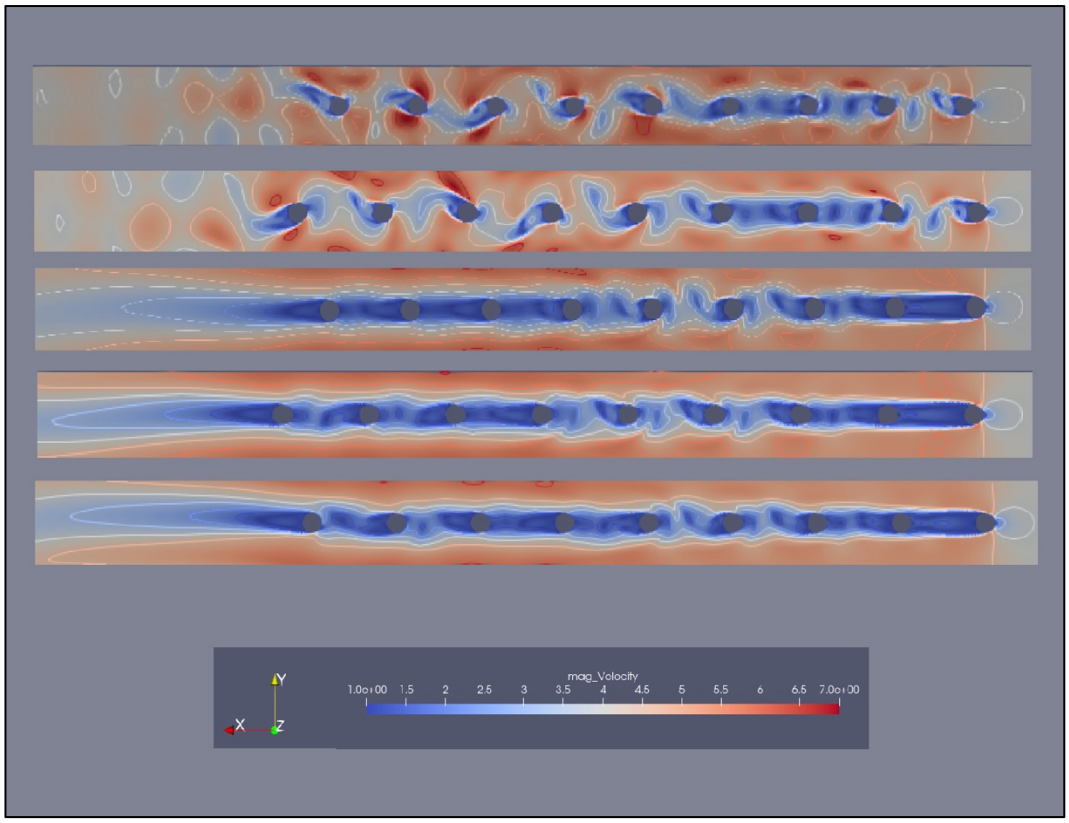

Figure 3.17 Isocontour of the velocity magnitude for the testcase:
Re=6000, Isothermal temperature= 403℃
SST2003V model, from top to bottom
XCoarse, Coarse, Medium, Fine and XFine meshes

Isocontour of the temperature are shown for each mesh in figures 3.22. Temperature contours from XCoarse to XFine mesh (top to bottom) show increasing precision in recording thermal gradients near pin fins. The temperature field seems spread with coarser meshes, with fewer hot zones and thermal wakes. As the mesh is refined, the thermal boundary layers grow thinner and clearer, particularly near hot surfaces, suggesting better resolution of convective heat transfer effects. The XFine mesh effectively captures vortex-induced mixing and thermal wake propagation downstream, which is crucial for accurate thermal performance prediction in heatsink applications. The temperature around the fins is at the values between 350 ℃ to 370 ℃ while the higher value of 382 ℃ is observed on the fine meshes.

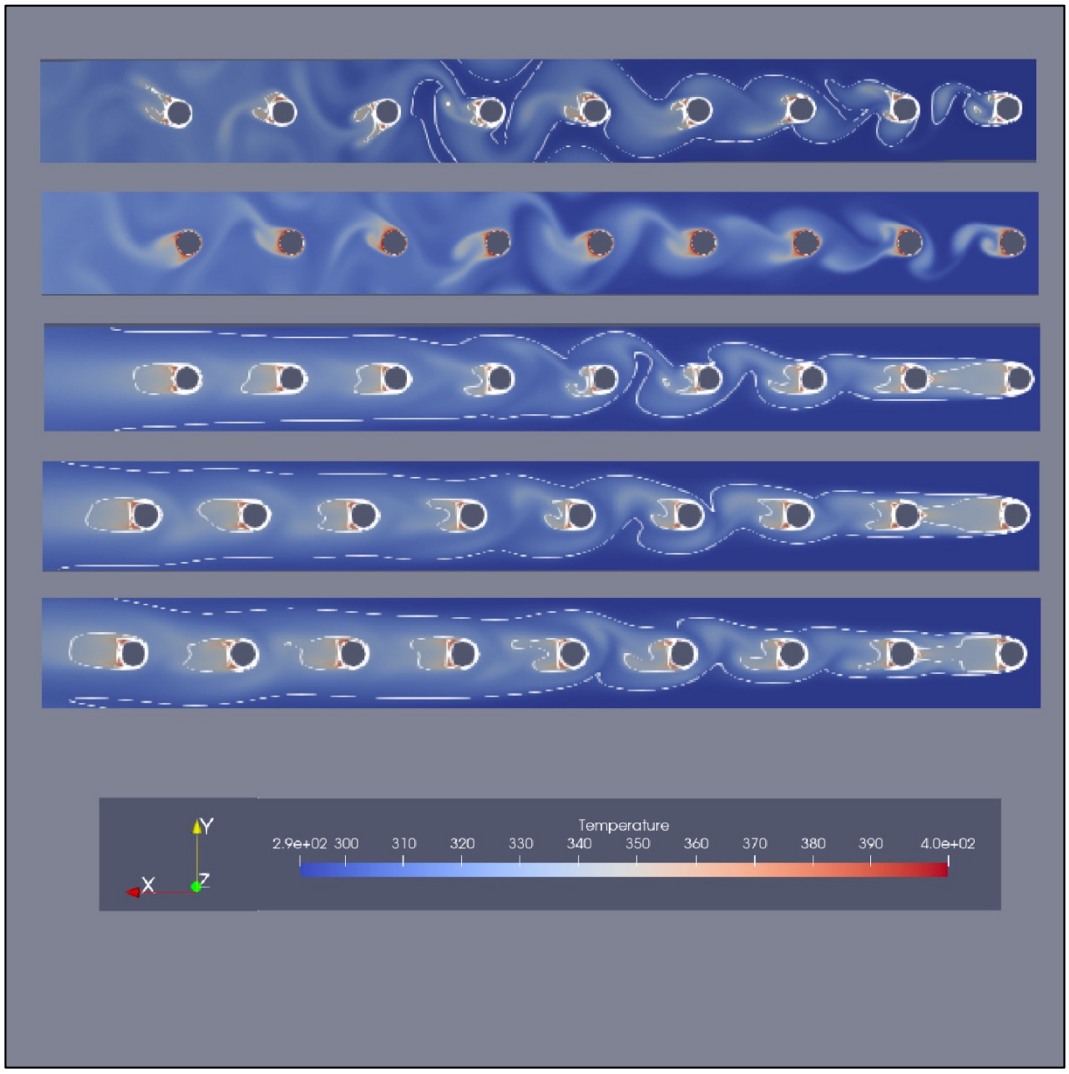

Figure 3.18 Isocontour of temperature for the testcase:
Re=6000, Isothermal temperature= 403℃
Time-iterations=200000, from top to bottom
XCoarse, Coarse, Medium, Fine and XFine meshes, SST2003V model

Eddy viscosity for the test case is shown for different meshes in Figure 3.23. The eddy viscosity contours from XCoarse to XFine mesh indicate a significant increase in turbulence resolution as the mesh is refined. This development emphasizes the significance of mesh refinement in capturing precise turbulent behaviour and producing consistent CFD results. The highest observed value is 0.0004.

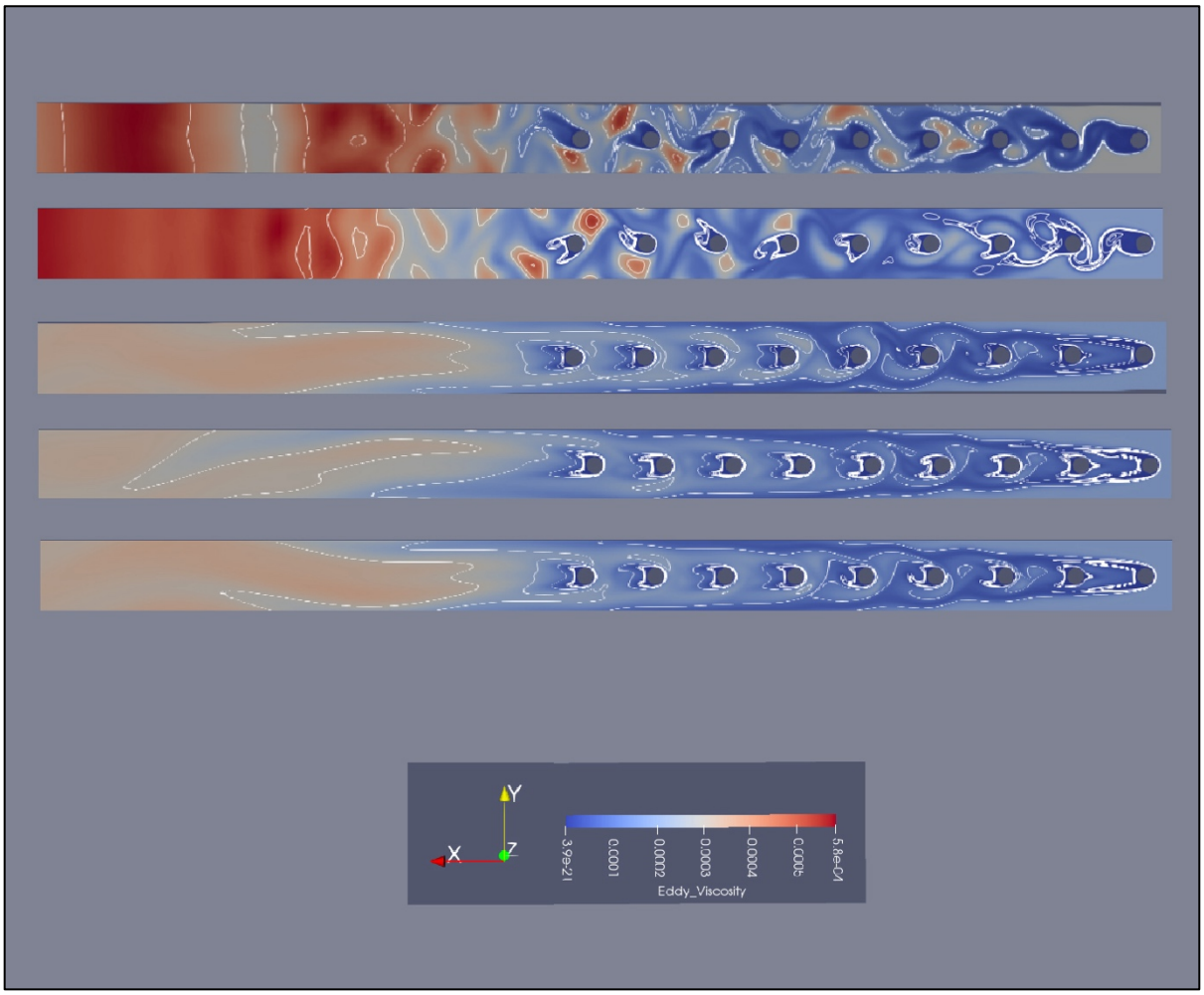

Figure 3.19 Isocontour of Turbulent viscosity for the test case:
Re=6000, Isothermal temperature= 403℃
Time-iterations=200000, from top to bottom
XCoarse, Coarse, Medium, Fine and XFine meshes, SST2003V model

3.2.4 Pressure Drop and Thermal Resistance for: Re=4000,6000,10000,12400, Isothermal=303, 353, 403℃; Standard SST, SST2003V and Spalart-Allmaras models

In this part of the work, the average pressure drops, and thermal resistances for different meshes will be valued for Re=4000, 6000, 10000, 12400. The pressure drop is evaluated as the difference between the average pressure on planes just before and after the inline cylinders. Table 3.2 shows the pressure drop (Pa) of different test cases for the Standard SST model. The pressure drops decreases with mesh refinement across all Reynolds numbers. At Re = 4000, the Pressure drop decreases from 19.02 Pa (Xcoarse) to 5.94 Pa (Xfine), demonstrating strong mesh sensitivity. For higher Reynolds numbers, results converge around the fine mesh, suggesting it provides a good balance between accuracy and computational efficiency.

Table 3.2 Time-average of Pressure Drop [Pa] for the test case:
Isothermal= 303℃, Meshes:
Xcoarse, Coarse, Medium, Fine, Xfine. Standard SST model

Mesh	Re=4000	Re=6000	Re=10000	Re=12400
Xcoarse	19.02 [Pa]	27.38 [Pa]	68.4 [Pa]	101.79 [Pa]
Coarse	10.65	17.28	56.4	81.52
Medium	7.75	16.1	46.4	69.83
Fine	6.88	15.83	43.7	64.1
Xfine	5.94	-	-	-

Table 3.3 Time-average of Pressure Drop [Pa] for the test case:
Isothermal= 403℃, Meshes:
Xcoarse, Coarse, Medium, Fine, Xfine. Standard SST model

Mesh	Re=4000	Re=6000	Re=10000	Re=12400
Xcoarse	12.05 [Pa]	26.34 [Pa]	68.96 [Pa]	102.86 [Pa]
Coarse	11.31	25.64	61.15	94.6
Medium	8.32	17.34	56.77	87.95
Fine	7.96	16.74	44.02	66.33
Xfine	6.26	14.91	-	-

Table 3.3 shows consistent pressure drop decrease with mesh refinement for all Reynolds numbers, highlighting the influence of grid resolution. At Re = 4000, the pressure drop went from 12.05 Pa (Xcoarse) to 6.26 Pa (Xfine). The trend was similar at higher Reynolds numbers, where convergence appears to be approached by the Fine mesh, particularly at Re = 12400 which the pressure drop decreased from 102.86 Pa to 66.33 Pa.

Table 3.4 Time-average of Pressure Drop [Pa] for the test case:
Isothermal= 303℃, Meshes:
Xcoarse, Coarse, Medium, Fine, Xfine. SST2003V model

Mesh	Re=4000	Re=6000	Re=10000	Re=12400
Xcoarse	12.2 [Pa]	28.1[Pa]	68.96[Pa]	102.86[Pa]
Coarse	10.3	23.36	61.5	97.02
Medium	6.97	16.56	57.81	87.55
Fine	5.71	15.75	44.02	69.92
Xfine	-	15.5	-	-

Table 3.4 shows a clear decrease of the pressure drop with the refinement of the meshes specifically at Re = 4000 and Re = 6000. At Re=6000 the pressure drop decreased from 28.1 Pa (Xcoarse) to 15.5 Pa (Xfine), reflecting the effects associated with finer meshes.

Table 3.5 Time-average of Pressure Drop [Pa] for the test case:
Isothermal= 353℃, Meshes:
Xcoarse, Coarse, Medium, Fine, Xfine. SST2003V model

Mesh	Re=4000	Re=6000	Re=10000	Re=12400
Xcoarse	11.72[Pa]	26.12[Pa]	68.96[Pa]	102.86[Pa]
Coarse	11.67	25.41	61.15	97.02
Medium	8.32	17.35	57.84	87.54
Fine	7.96	15.71	44.09	70.45
Xfine	5.93	13.64	-	-

Table 3.5 illustrates the decline in pressure drop for finer, reflecting reduced discretization error. At Re = 6000, pressure drop decreased from 26.12 Pa (Xcoarse) to 13.64 Pa (Xfine). The fine mesh generally provides stable and reliable results, while the Xfine mesh offers further

precision but encountered convergence limitations at higher Reynolds numbers. Meanwhile the medium mesh was more practical from an engineering perspective considering the CPU usage and required calculation time. While the Xfine was not converged using 4 nodes for 64 parallel tasks for a calculation time of 24:00 on beluga servers, the Fine mesh calculation time was around 17 hours with same calculation properties.

Table 3.6 Time-average of Pressure Drop [Pa] for the test case:
Isothermal= 403℃, Meshes:
Xcoarse, Coarse, Medium, Fine, Xfine. SST2003V model

Mesh	Re=4000	Re=6000	Re=10000	Re=12400
Xcoarse	11.70[Pa]	25.95[Pa]	68.96	97.01[Pa]
Coarse	11.67	25.68	61.15	97.01
Medium	8.34	17.34	44.3	87.96
Fine	7.62	16.45	41.27	73.23
Xfine	5.94	12.04	-	71.14

Table 3.6 shows a clear trend of decreasing pressure drop with mesh refinement confirming reduced numerical diffusion. At Re = 6000, pressure drop reduced from 25.95 Pa (Xcoarse) to 12.04 Pa (Xfine), indicating significant improvement in capturing flow behavior. While the Xfine mesh provides the most accurate representation, convergence issues limit its use in all test cases. The medium mesh offered a practical balance between precision and computational efficiency. The Xfine mesh were not converged for all test cases after 200,000 utilizing 4 nodes each node compiling 64 tasks for a 24:00 hours calculation time on Narval.

Table 3.7 Time-average of Pressure Drop [Pa] for the test case:
Isothermal= 303℃, Meshes:
Xcoarse, Coarse, Medium, Fine, Xfine. Spalart-Allmaras model

Mesh	Re=4000	Re=6000	Re=10000	Re=12400
Xcoarse	11.77[Pa]	25.18 [Pa]	63.13[Pa]	91.35 [Pa]
Coarse	8.57	21.53	58.06	80.99
Medium	7.42	17.83	53.72	79.29
Fine	7.26	17.24	48.63	73..53
Xfine	-	10.98	45.17	72.41

Table 3.8 Time-average of Pressure Drop [Pa] for the test case:
Isothermal= 353℃, Meshes:
Xcoarse, Coarse, Medium, Fine, Xfine. Spalart-Allmaras model

Mesh	Re=4000	Re=6000	Re=10000	Re=12400
Xcoarse	11.55[Pa]	25.18[Pa]	60.52[Pa]	91.35 [Pa]
Coarse	11.22	24.42	57.3	80.94
Medium	8.63	17.69	53.69	79.63
Fine	7.58	15.22	48.33	73.52
Xfine	-	14.89	45.13	71.78

Table 3.9 Time-average of Pressure Drop [Pa] for the test case:
Isothermal= 403℃, Meshes:
Xcoarse, Coarse, Medium, Fine, Xfine. Spalart-Allmaras model

Mesh	Re=4000	Re=6000	Re=10000	Re=12400
Xcoarse	11.55[Pa]	25.22[Pa]	60.52[Pa]	81.04 [Pa]
Coarse	10.35	24.24	58.06	81.02
Medium	8.57	18.97	53.75	79.62
Fine	7.65	15.84	48.91	73.45
Xfine	-	-	46.44	66.03

Table 3.7 to 3.9 show the pressure drop decrease for Spalart-Allmaras model with mesh refinement, confirming mesh sensitivity. Re = 10000 showed a pressure drop ranging from around 63 Pa (Xcoarse) mesh to about 45–46 Pa (Xfine) meshes. This trend continued for all Reynolds numbers, particularly at Re = 12400, where Xfine values are the lowest. The consistent pattern suggested that finer meshes better resolve the flow, especially near boundaries.

Table 3.10 Thermal Resistance(K/W) for the test case:
Isothermal= 303℃,
Meshes: Xcoarse, Coarse, Medium, Fine. Standard SST model

Mesh	Re=4000	Re=6000	Re=10000	Re=12400
Xcoarse	19.46[K/W]	14.18	10.51	9.05
Coarse	23.29	17.06	11.28	9.83
Medium	25.82	18.42	11.26	11.31
Fine	26.87	19.37	12.96	11.46
Xfine	27.31	-	-	-

Table 3.11 Thermal Resistance(K/W) for the test case:
Isothermal= 403℃,
Meshes: Xcoarse, Coarse, Medium, Fine. Standard SST model

Mesh	Re=4000	Re=6000	Re=10000	Re=12400
Xcoarse	16.78[K/W]	13.02	9.69	8.49
Coarse	17.26	13.34	10.13	8.76
Medium	20.19	16.14	12.10	9.11
Fine	20.88	16.59	12.37	9.57
Xfine	22.45	16.78	-	-

Table 3.10 and 3.11 shows the decrease of thermal resistance values with increasing Reynolds number, showing enhanced convective heat transfer at higher flow rates. Both tables suggest that refining the mesh tends to slightly increase the thermal resistance, particularly from Coarse to Fine levels, indicating improved resolution of temperature gradients. At Re = 4000, resistance rose from 19 K/W (Xcoarse) to 27 K/W (Xfine) in Table 3.10. However, the

differences between Medium and Fine/Xfine meshes are suggesting convergence. Overall, results validate expected trends: higher Reynolds Number, lowers thermal resistance.

Table 3.12 Thermal Resistance(K/W) for the test case:
Isothermal= 303℃,
Meshes: Xcoarse, Coarse, Medium, Fine. SST2003V model

Mesh	Re=4000	Re=6000	Re=10000	Re=12400
Xcoarse	18.63[K/W]	14.46	10.77	9.35
Coarse	18.91	14.85	11.12	9.44
Medium	22.32	17.77	11.42	10.12
Fine	22.39	18.19	13.35	11.41
Xfine	-	18.72	-	-

Table 3.13 Thermal Resistance(K/W) for the test case:
Isothermal= 353℃,
Meshes: Xcoarse, Coarse, Medium, Fine. SST2003V model

Mesh	Re=4000	Re=6000	Re=10000	Re=12400
Xcoarse	15.48[K/W]	12.13	8.95	7.74
Coarse	16.27	12.46	9.27	8.01
Medium	18.56	14.16	9.51	8.38
Fine	19.15	14.76	11.12	9.43
Xfine	20.52	14.89	-	-

Table 3.14 Thermal Resistance(K/W) for the test case:
Isothermal= 403℃,
Meshes: Xcoarse, Coarse, Medium, Fine. SST2003V model

Mesh	Re=4000	Re=6000	Re=10000	Re=12400
Xcoarse	16.63[K/W]	13.29	9.65	9.4
Coarse	17.65	13.31	10.13	9.6
Medium	22.21	17.72	13.31	10.11
Fine	22.84	18.53	13.48	10.7
Xfine	23.25	18.88	-	10.8

Tables 3.12 to 3.14 present the thermal resistance (K/W) for the SST2003V turbulence model under isothermal boundary conditions of 303 K, 353 K, and 403 K, across various mesh densities and Reynolds numbers. Between all temperatures, thermal resistance decreased with increasing Reynolds number, reflecting enhanced convective heat transfer at higher flow rates. At lower Reynolds numbers Re = 4000 and 6000, the variation in resistance across meshes was more observable, while at higher Reynolds numbers, especially Re = 12400, results begin to stabilize, especially for medium to fine meshes The finest meshes of Fine and Xfine produced more consistent values, suggesting mesh independence is nearly achieved in many cases, though some Xfine data are missing at high Reynolds numbers. Overall, the SST2003V model demonstrated consistent behavior across temperature conditions, with expected physical trends in heat transfer performance of Bencherif et al. (2023).

.

Table 3.15 Thermal Resistance(K/W) for the test case:
Isothermal= 303℃,
Meshes: Xcoarse, Coarse, Medium, Fine. Spalart-Allmaras model

Mesh	Re=4000	Re=6000	Re=10000	Re=12400
Xcoarse	19.62[K/W]	14.71	11.48	10.27
Coarse	19.85	15.12	11.60	10.77
Medium	20.97	16.27	11.91	10.91
Fine	22.34	16.92	12.56	11.03
Xfine	-	17.41	13.52	11.12

Table 3.16 Thermal Resistance(K/W) for the test case:
Isothermal= 353℃,
Meshes: Xcoarse, Coarse, Medium, Fine. Spalart-Allmaras model

Mesh	Re=4000	Re=6000	Re=10000	Re=12400
Xcoarse	15.1[K/W]	12.31	10.05	8.57
Coarse	16.02	12.34	9.62	9.61
Medium	16.56	13.54	9.94	8.84
Fine	17.45	13.82	10.48	9.06
Xfine	-	14.59	11.36	9.17

Table 3.17 Thermal Resistance(K/W) for the test case:
Isothermal= 403℃,
Meshes: Xcoarse, Coarse, Medium, Fine, Xfine. Spalart-Allmaras model

Mesh	Re=4000	Re=6000	Re=10000	Re=12400
Xcoarse	17.12[K/W]	13.49	10.54	8.87
Coarse	17.73	13.57	10.59	9.29
Medium	19.91	16.24	11.5	10.2
Fine	20.04	17.21	12.04	10.77
Xfine	20.07	17.71	12.08	11.1

Tables 3.15 to 3.17 showed the thermal resistance (K/W) values for the Spalart-Allmaras turbulence model under three different isothermal boundary conditions (303 K, 353 K, and 403 K), evaluated across a range of mesh densities and Reynolds numbers. Across all temperatures, thermal resistance decreased as the Reynolds number increased, confirming the expected improvement in convective heat transfer with higher flow rates. Comparing across the three isothermal conditions, it is evident that thermal resistance is correlated with wall temperatures; for example, at Re = 12400 and fine mesh, the resistance decreased from 11.03 K/W (303 K) to 9.06 K/W (353 K), and then increase to 10.77 K/W (403 K). Meanwhile the fluctuation of the values suggests that there is an optimal temperature to improve the pressure drop and thermal resistance which should be investigated in a more specific study. Mesh refinement led to slightly higher or stabilized thermal resistance values, particularly in medium to fine mesh ranges, indicating convergence. The Xfine mesh results, where available, are often the highest, suggesting the onset of mesh independence. However, some inconsistencies in the trend (higher resistance at 403 K than 353 K at Re = 12400 for fine mesh) could suggest to nonlinearities in temperature effects or numerical sensitivity. Overall, the Spalart-Allmaras model showed consistent and physically reasonable thermal resistance behavior across different thermal and flow conditions.

Tables 3.2 to 3.17 present the time-averaged pressure drop (Pa) and thermal resistance (K/W) for each test case, considering various turbulence models, isothermal boundary conditions, and Reynolds numbers. It is important to note that for some test cases, the XFine mesh did not reach convergence. The results indicate that the pressure drop generally increases with rising Reynolds number, reflecting the expected behavior of enhanced inertial effects. Conversely, thermal resistance exhibits a decreasing trend as the Reynolds number increases, consistent with improved convective heat transfer at higher flow rates. In the next part of the study, the results of each model will be compared to each other.

3.2.5 Pressure Drop and Thermal Resistance for the Medium Mesh for Re= 4000,6000,10000,12400

The mesh study indicates that the medium mesh gives acceptable engineering prediction for the inline pin-fin heat exchanger. The pressure drop is computed for four Reynolds number. The pressure drop is expected to increase with the Reynolds number according to the Jonsson & Moshfegh (2001) study which modelled the thermal performance and Hydraulic performance of the Pate, Strip and Pin-Fin Heatsinks. Correlation 7 and 8 of the study predicted pressure drop and thermal resistance. Pressure drop should scale with $Re^{-0.1759}$ for in line circular pin fin. Nusselt should scale with $Re^{0.6422}$.

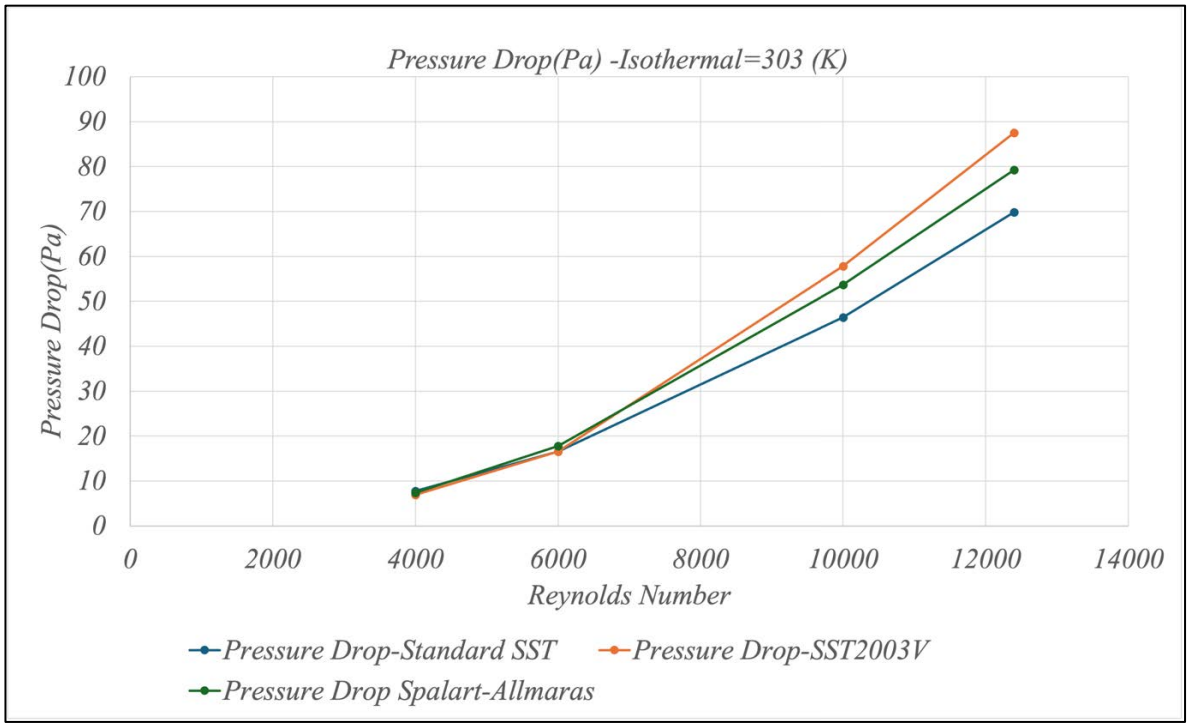

Figure 3.20 Time-average of Pressure Drop (Pa) for the test cases:
Re=4000,6000,10000,12400, Isothermal= 303℃,
Mesh= Medium. Standard SST, SST2003V, Spalart-Allmaras models

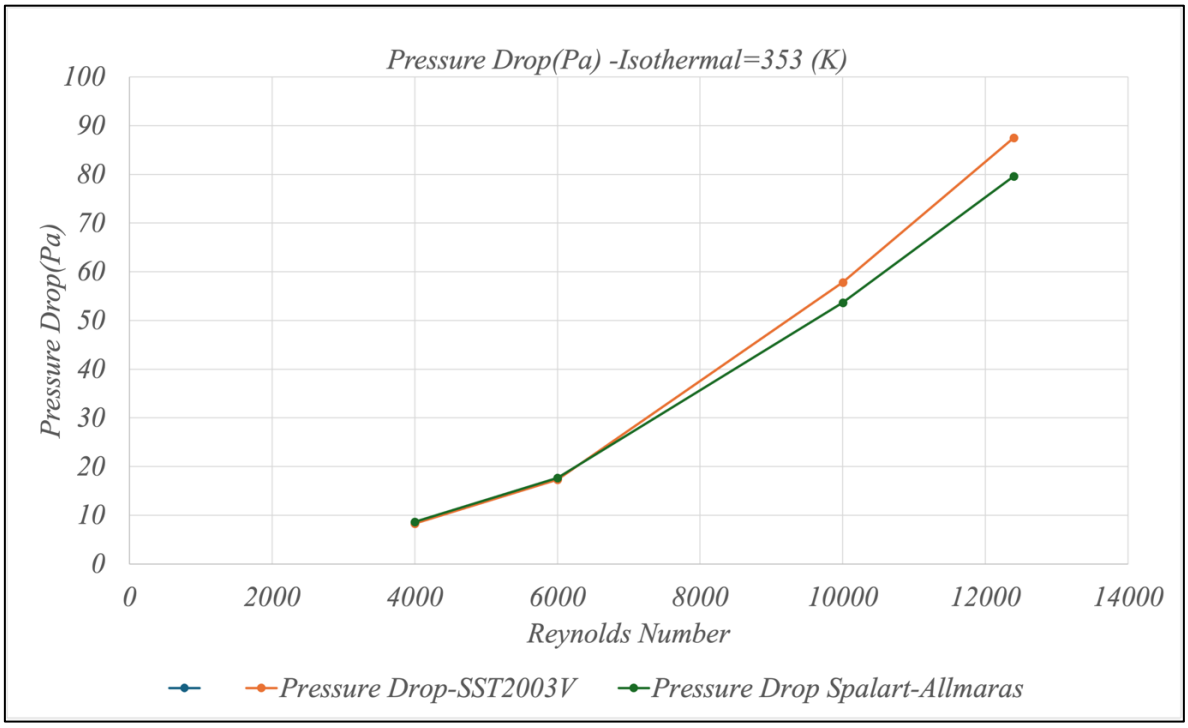

Figure 3.21 Time-averaged Pressure Drop(Pa) for the test case:
Re=4000,6000,10000,12400, Isothermal= 353℃,
Time iteration=200000, Mesh= Medium. SST2003V, Spalart Allmaras model

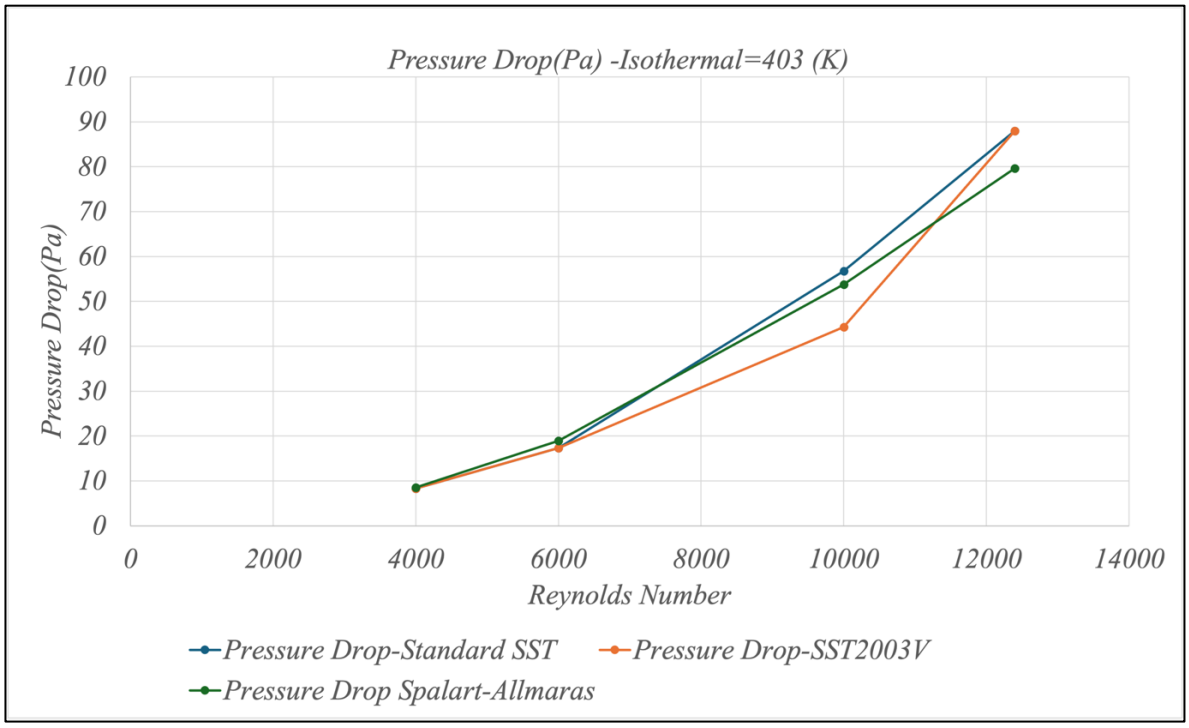

Figure 3.22 Time-average of Pressure Drop (Pa) for the test case: Re=4000,6000,10000,12400, Isothermal= 403℃, Mesh= Medium. Standard SST, SST2003V, Spalart-Allmaras models

Figure 3.20 to 3.22 present the variation of pressure drop with Reynolds number for different isothermal conditions (403 K, 353 K, and 303 K), using three turbulence models: Standard SST, SST-2003V, and Spalart–Allmaras. Moshfegh & Nyiredy (2004) also studied the pressure drop based for different turbulent models but instead their approach was utilizing standard $k-\varepsilon$, RNG, and Reynolds Stress Model (RSM). Between all cases, pressure drop increases consistently with Reynolds number, which is expected due to the rise in flow momentum at higher velocities. The influence of the turbulence model varies with temperature. At 403 K and 353 K, the SST-2003V model tends to predict higher pressure drops, especially at higher Reynolds numbers, while the Spalart–Allmaras model shows slightly lower values. For instance, at Re=12400 for T=403 K, there is 25% difference between two models. At 303 K, the SST-2003V model still yields the highest pressure drop, while the Standard SST model results in the lowest predictions at higher Reynolds numbers. These differences become more

observable as the Reynolds number increases, suggesting that the SST-2003V model may be more sensitive to both flow intensity and thermal conditions.

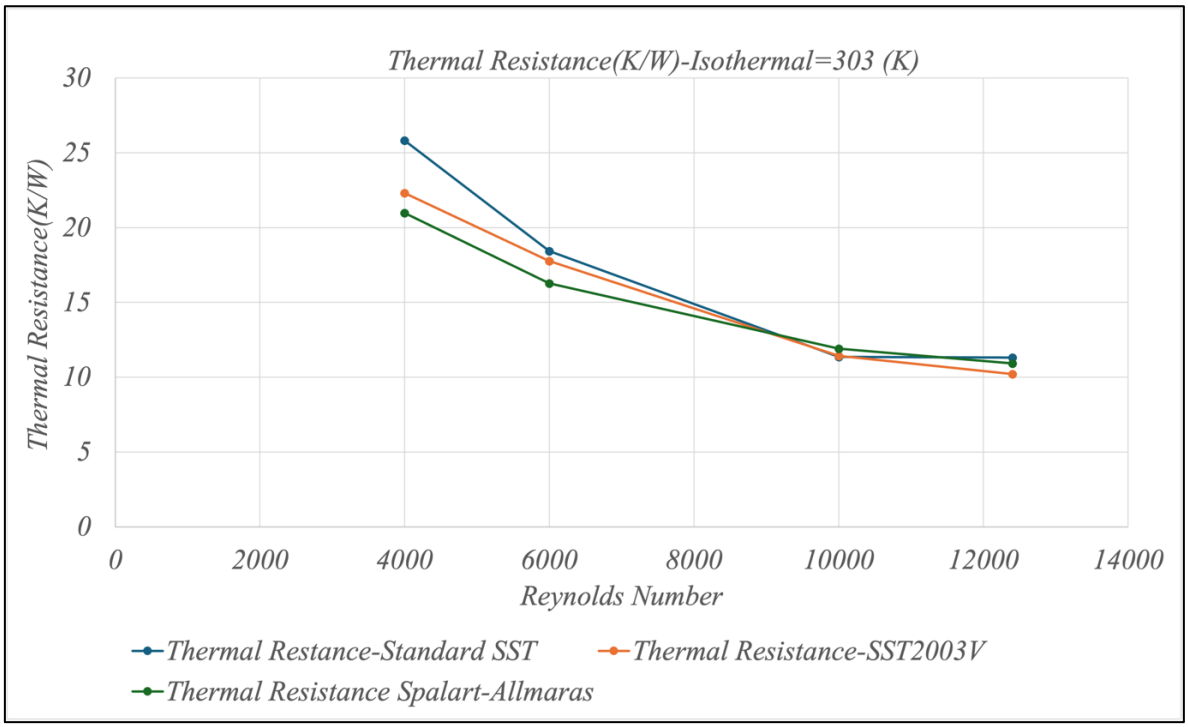

Figure 3.23 Thermal resistance (K/W) for the test case: Re=6000,4000,10000,12400, Isothermal= 303℃, Mesh= Medium. Standard SST, SST2003V, Spalart-Allmaras models

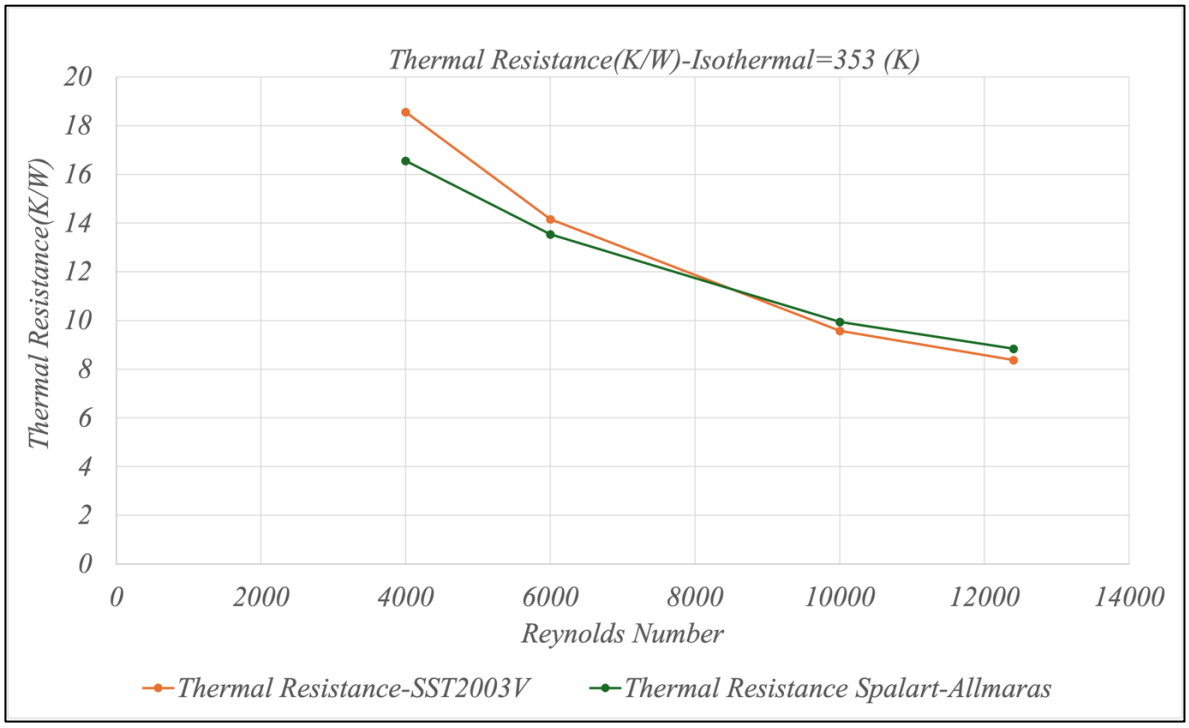

Figure 3.24 Thermal Resistance for
Isothermal= 353℃, Mesh= Medium, SST2003V, Spalart-Allmaras models

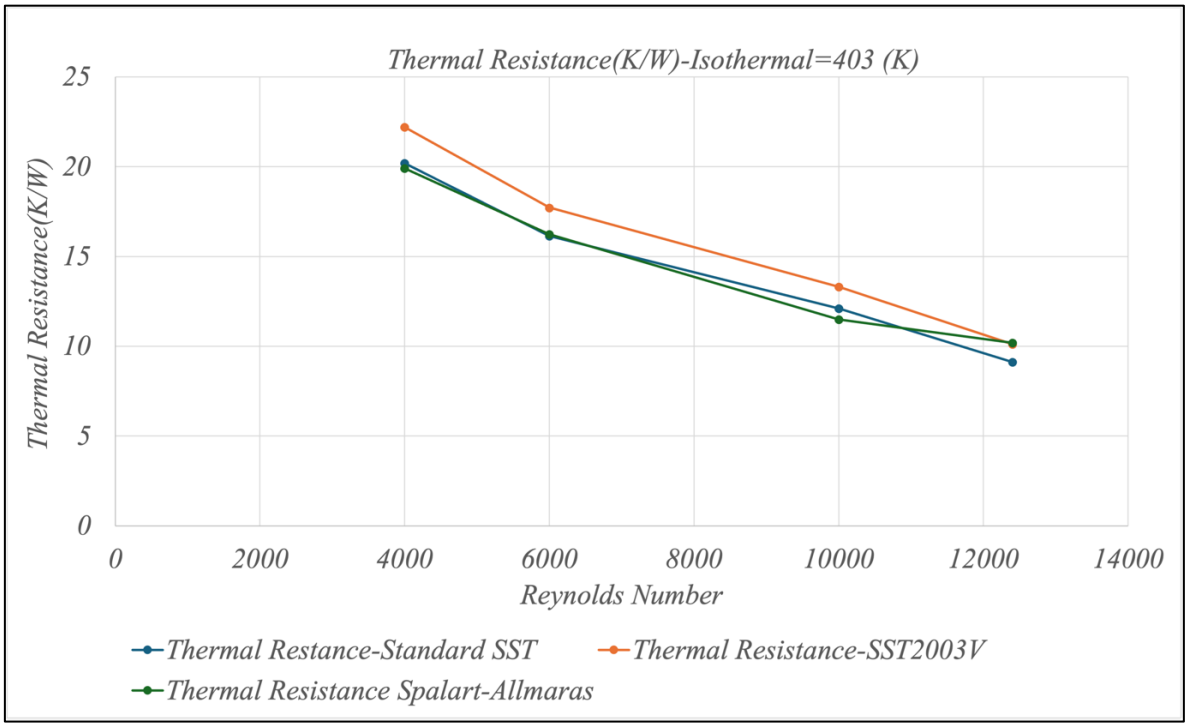

Figure 3.25 Thermal Resistance(K/W) for
isothermal= 403℃, Mesh= Medium.
Standard SST, SST2003V, Spalart-Allmaras models

Figures 3.23 to 3.25 show how thermal resistance (K/W) changes under three different isothermal conditions 303 (K), 353 (K), and 403 (K) using various turbulence models. Unlike pressure drop, which increases with Reynolds number, thermal resistance tends to decrease as the Reynolds number rises according to Bencherif et al. (2023). This behavior is mainly due to the improved convective heat transfer at higher flow velocities, which allows heat to dissipate more efficiently.

3.2.6 Comparison with Experimental results

To compare the CFD results with the experimental results of the literature, the pressure drop and thermal resistance were compared to experimental work of Jonsson & Moshfegh (2001) for the Re=4000,6000,10000,12400. They have used a square heat exchanger with nine-by-nine in-line square pin-fins as one of their test cases which were subjected to the parallel

airflow such as the suggested model. Although the number of the fins are 9 times higher than the model, it is comparable to our inline pin-fins with periodic boundary conditions. To decrease the level of error, difference of number of the fins were considered during the work.

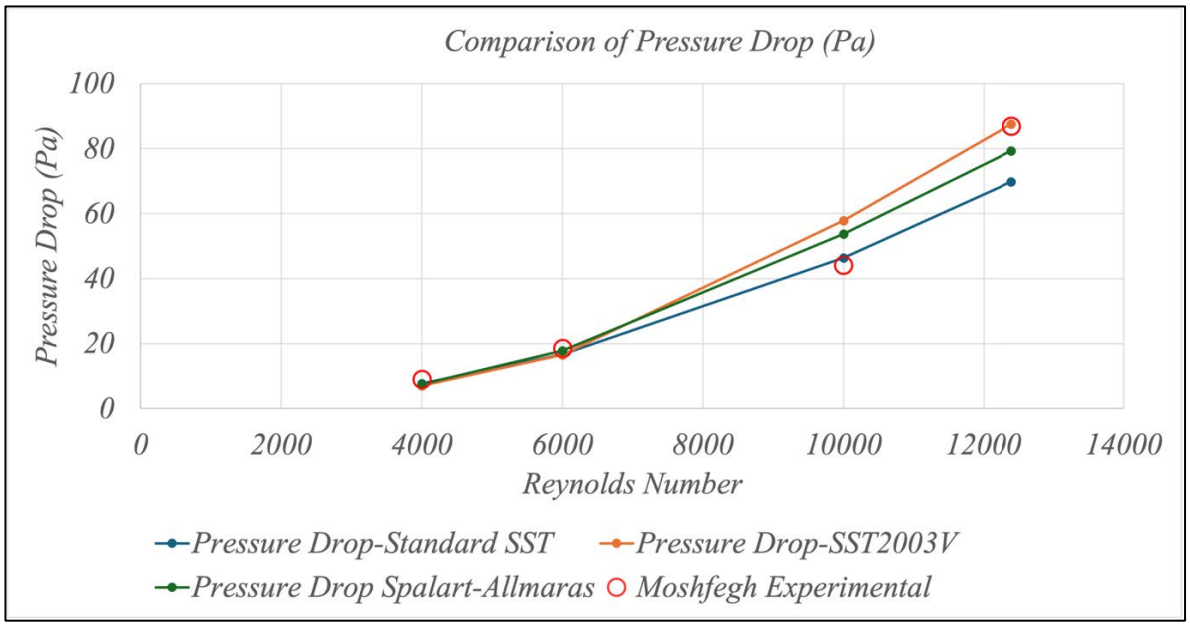

Figure 3.26 Comparison of pressure drop (Pa) of CFD to Experimental results of Jonsson & Moshfegh (2001)

Figure 3.26 shows the difference between the CFD results and the experimental results from literature at 303.15 (K). The predicted pressure drop was higher than the experimental data, for Re=10000. It was higher for Re=12500. The absolute error of each model compared to experimental results is shown in table 3.18.

Table 3.18 The error (%) of each model compared to experimental results for the pressure drop [Pa]

Reynolds Number	Standard SST	SST2003V	Spalart-Allmaras
4000	1	2	2
6000	1	2	1
10000	2	13	9
12400	17	1	7

The table shows that the Spalart-Allmaras model performed the most consistently for all Reynolds numbers, with the lowest average error and no extreme deviations. The SST model was accurate at lower Reynolds numbers: Re = 4000 and 6000, but underpredicted the pressure drop at Re = 12400, resulting in its highest error. The SST2003V model performs well at high Reynolds numbers, particularly at Re = 12400, where it has the smallest error among all models, but it showed a major overprediction at Re = 10000, giving the highest single-point error in the dataset. Overall, Spalart-Allmaras provides the most balanced and reliable prediction relative to experimental data.

Figure 3.27 compares the CFD results to the experimental work of Jonsson & Moshfegh (2001) for the surface temperature at 303.15 (K). Turbulence models overpredict the thermal resistance. Note that our geometry does not include heat transfer from the plate that hold the cylinders, whereas experiment include it. It could explain the lower experimental thermal resistance, but additional 3D CFD verification would be needed to be conclusive.

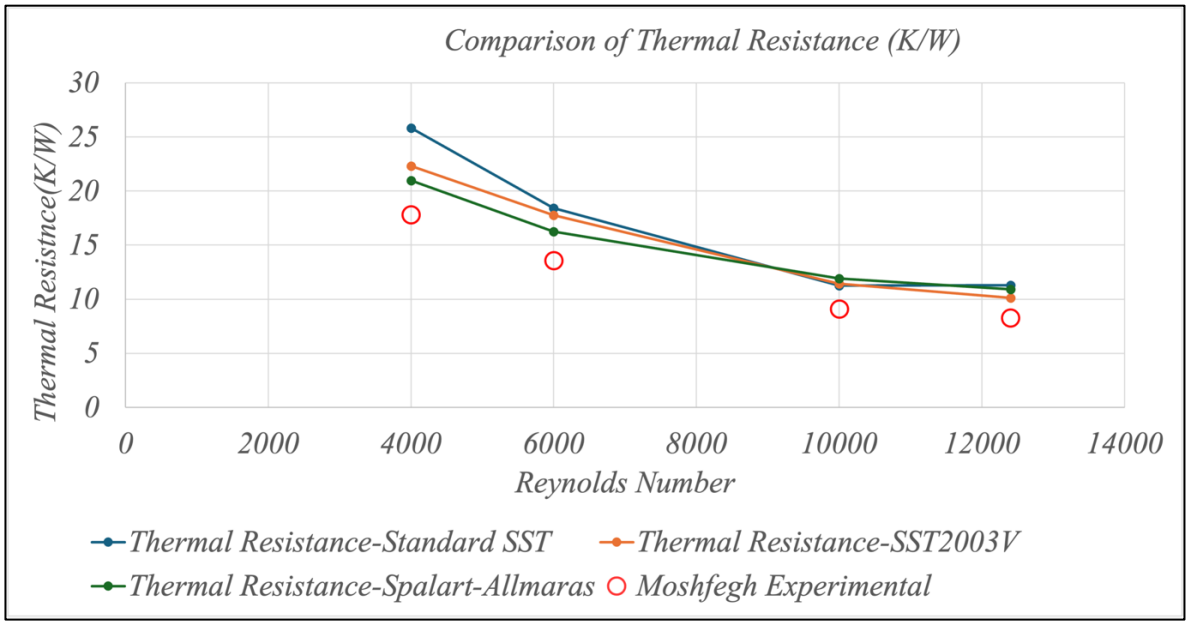

Figure 3.27 Comparison of Thermal Resistance(K/W) of CFD to Experimental results of Jonsson & Moshfegh (2001)

Although the CFD results have shown similar decreasing pattern compared to the experimental work of Jonsson & Moshfegh (2001), the error of model for each test case is studied.

Table 3.19 The error (%) of each model compared to experimental results for the Thermal Resistance [K/W]

Reynolds Number	Standard SST	SST2003V	Spalart-Allmaras
4000	44	25	17
6000	35	30	19
10000	23	25	30
12400	36	22	31

The percentage of error analysis showed that all CFD models overpredict the thermal resistance compared to the experimental data across all Reynolds numbers. Among the three, the Spalart-Allmaras model showed the lowest error at Re = 4000 (17%), indicating better agreement in low-flow regimes. However, its error increases significantly at higher Reynolds numbers. The

SST2003V model provided a more balanced performance with consistently lower errors at Re = 12400 (22%). Meanwhile, the Standard SST model tended to show the highest error at low Reynolds numbers (44% at Re = 4000), though the gap narrowed as the Reynolds number increased. Overall, none of the models fully capture the experimental behavior, but SST2003V shows more stability across the range. This error may cause by the fact that in the model both the thermal resistance of solid and flow parts is studied but the proposed model is only for the flow. To improve the results, the solid zone should be added in the further studies.

3.3 Summary

In this chapter, the results of the proposed computational model were presented and analyzed in detail. The initial section examined the convergence of the computational meshes, which was evaluated based on a range of criteria, including pressure, velocity, and temperature. This analysis ensures the reliability and accuracy of the numerical results obtained.

To validate the model, a comparison was made between the pressure coefficient and the Nusselt number obtained from the simulations and Zhang et al. (2019) and Huang et al. (2021). This comparison provides a critical verification on the accuracy of the model and its agreement with previously established results.

The subsequent section delved into a study of the pressure drop and thermal resistance characteristics for three turbulence models: Standard SST, SST 2003V, and Spalart-Allmaras. These models are evaluated under varying isothermal boundary conditions and across different Reynolds numbers to explore the sensitivity of the results to these factors. The performance of each turbulence model is carefully compared in terms of their ability to predict pressure drop and thermal resistance, with an emphasis on understanding the underlying fluid dynamics.

In the final part of the chapter, the results obtained from the medium mesh configuration were compared with experimental data from Jonsson & Moshfegh (2001) concerning pressure drop and thermal resistance. This comparison not only serves to validate the numerical model but

also demonstrates its applicability in engineering world, providing insight into its potential for future use in thermal management applications.

CONCLUSION

This thesis presented a computational investigation into the thermal performance of heat sinks under various flow and thermal boundary conditions. The objective of this study was to analyze the impact of flow characteristics: velocity and wall temperature on the performance of heatsinks. The pressure drop and thermal resistance were reported for a flow around nine in-line cylinders. This simplified 2D geometry is representative of a square pin-fin heat exchanger.

The study was initiated with a comprehensive literature review that discussed previous research on heat sink design, materials, thermal performance metrics, and prior CFD simulations. This foundational review provided valuable context for the selection of RANS modelling approaches and performance evaluation criteria used in the current work. According to literature, the SST turbulence gives acceptable results. For impinging jet heat sink, the performance metrics is the pressure coefficient and Nusselt number along the surface. For pin-fin heat sink, the pressure drop and thermal resistance are commonly used.

The numerical methodology was then thoroughly described, highlighting the unsteady incompressible URANS equations, turbulence models (Standard SST, SST-2003V, and Spalart-Allmaras), boundary conditions, and mesh generation strategies. For the impinging jet heat sink, the conjugate heat transfer approach is favored to solve the solid conduction equation inside the heat sink and the URANS equations in the fluid. Special attention was paid to mesh independence by constructing family of meshes, from coarse to fine. These multiple meshes are needed for the mesh sensitivity study that evaluate the reliability of the computational results.

In the results section, mesh sensitivity was assessed using pressure, temperature, and velocity fields, and the impinging jet model was validated against established literature through comparisons of pressure coefficients and Nusselt numbers. Once validated, the simulations

were extended to analyze the isocontours of velocity, temperature, and turbulent viscosity to better understand the thermal and flow behavior within the heat sink structure.

The core of the investigation focused on evaluating thermal resistance and pressure drop across a 2D inline pin-fin heat exchanger. Three different turbulence models, Reynolds numbers, and isothermal wall boundary conditions were investigated. The CFD results were systematically compared with experimental data from the literature, demonstrating acceptable levels of agreement, particularly in trends. The pressure drop increases with the Reynolds number. Also, it was observed that thermal resistance decreased with increasing Reynolds number, confirming the enhancement of convective heat transfer at higher flow rates. Differences among turbulence models became more pronounced at higher Reynolds numbers, with SST-2003V generally showing the closest alignment with experimental data. The results showed that changing the wall temperature caused fluctuations. This shows that there may be an ideal temperature that improves both thermal resistance and pressure drop. However, additional research in a more concentrated study is required to completely understand and define the appropriate temperature for heat sink performance.

This work contributes to the growing body of knowledge on CFD-based heat sink analysis by providing validated numerical insights into the effects of turbulence modeling, mesh refinement, and operating conditions. The findings serve as a reference for future optimization studies and practical thermal management applications in electronic cooling and related engineering systems.

Future research should involve including the solid area into pin-fin test scenarios to better capture conduction effects. In a laboratory setting, it is also advised to increase the number of fins and rows to simulate a more industrial-scale structure. These modifications are intended to narrow the gap between CFD simulations and experimental results.

BIBLIOGRAPHY

Ahmed, H. E., Salman, B., Kherbeet, A. S., & Ahmed, M. (2018). Optimization of thermal design of heat sinks: A review. *International Journal of Heat and Mass Transfer*, *118*, 129-153.

Al-Damook, A., Kapur, N., Summers, J., & Thompson, H. (2015). An experimental and computational investigation of thermal air flows through perforated pin heat sinks. *Applied thermal engineering*, *89*, 365-376.

Alfonsi, G. (2009). Reynolds-averaged Navier–Stokes equations for turbulence modeling.

Alpsan, E. (2008). Experimental investigation and numerical analysis of microchannel heatsinks for phased array radar cooling application.

Arifin, Z., Tjahjana, D. D. D. P., Hadi, S., Rachmanto, R. A., Setyohandoko, G., & Sutanto, B. (2020). Numerical and experimental investigation of air cooling for photovoltaic panels using aluminum heat sinks. *International Journal of Photoenergy*, *2020*(1), 1574274.

Arshad, A., Ali, H. M., Ali, M., & Manzoor, S. (2017). Thermal performance of phase change material (PCM) based pin-finned heat sinks for electronics devices: Effect of pin thickness and PCM volume fraction. *Applied Thermal Engineering*, *112*, 143-155.

Arshad, A., Ali, H. M., Yan, W.-M., Hussein, A. K., & Ahmadlouydarab, M. (2018). An experimental study of enhanced heat sinks for thermal management using n-eicosane as phase change material. *Applied Thermal Engineering*, *132*, 52-66.

Baby, R., & Balaji, C. (2014). Thermal performance of a PCM heat sink under different heat loads: an experimental study. *International Journal of Thermal Sciences*, *79*, 240-249.

Baughn, J. W., Hechanova, A. E., & Yan, X. (1991). An experimental study of entrainment effects on the heat transfer from a flat surface to a heated circular impinging jet. *Journal of Heat Transfer (Transactions of the ASME (American Society of Mechanical Engineers), Series C);(United States)*, *113*(4).

Behnia, M., Copeland, D., & Soodphakdee, D. (1998). A comparison of heat sink geometries for laminar forced convection: numerical simulation of periodically developed flow (pp. 310-315). Communication présentée au ITherm'98. Sixth Intersociety Conference on Thermal and Thermomechanical Phenomena in Electronic Systems (Cat. No. 98CH36208), IEEE.

Bencherif, B., Sahel, D., Benzeguir, R., & Ameur, H. (2023). Performance analysis of central processing unit heat sinks fitted with perforation technique and splitter inserts. *ASME Journal of Heat and Mass Transfer*, *145*(1), 014501.

Bhattacharyya, S., Vishwakarma, D. K., Roy, S., Biswas, R., & Ardekani, M. M. (2020). Applications of heat transfer enhancement techniques: a state-of-the-art review. *Inverse Heat Conduction and Heat Exchangers*, 3.

Bonnie, A. (2015). Experimental design and comparative testing of a hybrid-cooled computer cluster (pp. 1-10). Communication présentée au Proceedings of the 3rd International Workshop on Energy Efficient Supercomputing.

Brendel, A., Popescu, C., Leyens, C., Woltersdorf, J., Pippel, E., & Bolt, H. (2004). SiC-fibre reinforced copper as heat sink material for fusion applications. *Journal of Nuclear Materials*, *329*, 804-808.

Cartagenas, I. (2021, 18 octobre). The Importance of Heat Sinks for the Thermal Management. *Thermtest*. Repéré à https://thermtest.com/the-importance-of-heat-sinks-for-the-thermal-management-of-electronic-devices

Chai, L., Xia, G. D., & Wang, H. S. (2016a). Numerical study of laminar flow and heat transfer in microchannel heat sink with offset ribs on sidewalls. *Applied Thermal Engineering*, *92*, 32-41.

Chai, L., Xia, G. D., & Wang, H. S. (2016b). Parametric study on thermal and hydraulic characteristics of laminar flow in microchannel heat sink with fan-shaped ribs on sidewalls–Part 1: Heat transfer. *International Journal of Heat and Mass Transfer*, *97*, 1069-1080.

Chapman, C. L., Lee, S., & Schmidt, B. L. (1994). Thermal performance of an elliptical pin fin heat sink (pp. 24-31). Communication présentée au Proceedings of 1994 IEEE/CHMT 10th Semiconductor Thermal Measurement and Management Symposium (SEMI-THERM), IEEE.

ChatGPT. (s.d.). Repéré à https://chatgpt.com/

Chiba, H., Ogushi, T., Nakajima, H., & Ikeda, T. (2004). Heat transfer capacity of lotus-type porous copper heat sink. *JSME International Journal Series B Fluids and Thermal Engineering*, *47*(3), 516-521.

Corson, D., Jaiman, R., & Shakib, F. (2009). Industrial application of RANS modelling: capabilities and needs. *International journal of Computational Fluid dynamics*, *23*(4), 337-347.

Coursey, J. S., Kim, J., & Boudreaux, P. J. (2005). Performance of graphite foam evaporator for use in thermal management.

Cui, H., Fan, W., Wang, J., Yu, M., Zhang, Z., Liu, Z., & Liu, W. (2024). Characteristics analysis and structure optimization of a hybrid micro-jet impingement/micro-channel heat sink. *Applied Thermal Engineering*, *245*, 122769.

Cuta, J. M., Bennett, W. D., McDonald, C. E., & Ravigururajan, T. (1995). Fabrication and testing of microchannel heat exchangers (Vol. 2640, pp. 152-160). Communication présentée au Microlithography and Metrology in Micromachining, SPIE.

Economon, T. D. (2020). Simulation and adjoint-based design for variable density incompressible flows with heat transfer. *AIAA Journal*, *58*(2), 757-769.

Economon, T. D., Mudigere, D., Bansal, G., Heinecke, A., Palacios, F., Park, J., … Dubey, P. (2016). Performance optimizations for scalable implicit RANS calculations with SU2. *Computers & Fluids*, *129*, 146-158. https://doi.org/10.1016/j.compfluid.2016.02.003

El-Sheikh, H. A., & Gurimella, S. (2000). Enhancement of air jet impingement heat transfer using pin-fin heat sinks. *IEEE Transactions on Components and Packaging Technologies*, *23*(2), 300-308.

Gallego, N. C., & Klett, J. W. (2003). Carbon foams for thermal management. *Carbon*, *41*(7), 1461-1466.

Goldberg, N. (1984). Narrow channel forced air heat sink. *IEEE transactions on components, hybrids, and manufacturing technology*, *7*(1), 154-159.

Hempijid, T., & Kittichaikarn, C. (2020). Effect of heat sink inlet and outlet flow direction on heat transfer performance. *Applied Thermal Engineering*, *164*, 114375.

Hirasawa, T., Kawabata, K., & Oomi, M. (2005). Evolution of the heatsink technology. *Furukawa Review*, *27*, 25-29.

Hosseinizadeh, S., Tan, F., & Moosania, S. (2011). Experimental and numerical studies on performance of PCM-based heat sink with different configurations of internal fins. *Applied Thermal Engineering*, *31*(17-18), 3827-3838.

Huang, H., Sun, T., Zhang, G., Liu, M., & Zhou, B. (2021). The effects of rough surfaces on heat transfer and flow structures for turbulent round jet impingement. *International Journal of Thermal Sciences*, *166*, 106982.

Ismail, M. F. (2013). Effects of perforations on the thermal and fluid dynamic performance of a heat exchanger. *IEEE Transactions on Components, Packaging and Manufacturing Technology*, *3*(7), 1178-1185.

Jaffal, H. M. (2017). The Effect of Fin Design on Thermal Performance of Heat Sink. *Journal of Engineering*, *23*(5), 123-146.

Jones, W. P., & Launder, B. E. (1972). The prediction of laminarization with a two-equation model of turbulence. *International journal of heat and mass transfer*, *15*(2), 301-314.

Jonsson, H., & Moshfegh, B. (2001a). Modeling of the thermal and hydraulic performance of plate fin, strip fin, and pin fin heat sinks-influence of flow bypass. *IEEE Transactions on Components and Packaging Technologies*, *24*(2), 142-149.

Jonsson, H., & Moshfegh, B. (2001b). Modeling of the thermal and hydraulic performance of plate fin, strip fin, and pin fin heat sinks-influence of flow bypass. *IEEE Transactions on Components and Packaging Technologies*, *24*(2), 142-149.

Jousson, H., & Palm, B. (2000). Thermal and hydraulic behavior of plate fin and strip fin heat sinks under varying bypass conditions. *IEEE Transactions on Components and Packaging Technologies*, *23*(1), 47-54.

Kalbasi, R. (2021). Introducing a novel heat sink comprising PCM and air-Adapted to electronic device thermal management. *International Journal of Heat and Mass Transfer*, *169*, 120914.

Kang, H. (2007). Optimum performance and design of a rectangular fin. *International journal of automotive technology*, *8*(6), 705-711.

Keller, K. (1998). Low cost, high performance, high volume heatsinks (pp. 113-118). Communication présentée au Twenty Second IEEE/CPMT International Electronics Manufacturing Technology Symposium. IEMT-Europe 1998. Electronics Manufacturing and Development for Automotives (Cat. No. 98CH36204), IEEE.

Kepekci, H., & Asma, A. (2020). Comparative analysis of heat sink performance using different materials. *American Journal of Engineering Research*, *9*(4), 204-210.

Khattak, Z., & Ali, H. M. (2019). Air cooled heat sink geometries subjected to forced flow: A critical review. *International Journal of Heat and Mass Transfer*, *130*, 141-161.

Khetib, Y., Sedraoui, K., Melaibari, A. A., Alzaied, A., Alsulami, R., & Sharifpur, M. (2021). Heat transfer and pressure drop in turbulent nanofluid flow in a pin-fin heat sink: Fin and nanoparticles shape effects. *Case Studies in Thermal Engineering*, *28*, 101378.

Kim, D.-K. (2012). Thermal optimization of plate-fin heat sinks with fins of variable thickness under natural convection. *International journal of heat and mass transfer*, *55*(4), 752-761.

Kim, T. Y., & Kim, S. J. (2009). Fluid flow and heat transfer characteristics of cross-cut heat sinks. *International Journal of Heat and Mass Transfer*, *52*(23-24), 5358-5370.

Kumar, A. U., Javed, A., & Dubey, S. K. (2018). Material selection for microchannel heatsink: Conjugate heat transfer simulation (Vol. 346, p. 012024). Communication présentée au IOP Conference Series: Materials Science and Engineering, IOP Publishing.

Kumaraguruparan, G., & Sornakumar, T. (2010). Development and testing of aluminum micro channel heat sink. *Journal of Thermal Science*, *19*, 245-252.

Lawag, R. A., & Ali, H. M. (2022). Phase change materials for thermal management and energy storage: A review. *Journal of Energy Storage*, *55*, 105602.

Lee, S. (1995). Optimum design and selection of heat sinks. *IEEE Transactions on Components, Packaging, and Manufacturing Technology: Part A*, *18*(4), 812-817.

Lei, N., Skandakumaran, P., & Ortega, A. (2006). Experiments and modeling of multilayer copper minichannel heat sinks in single-phase flow (pp. 9-18). Communication présentée au Thermal and Thermomechanical Proceedings 10th Intersociety Conference on Phenomena in Electronics Systems, 2006. ITHERM 2006., IEEE.

Li, H.-Y., Chao, S.-M., & Tsai, G.-L. (2005). Thermal performance measurement of heat sinks with confined impinging jet by infrared thermography. *International Journal of Heat and Mass Transfer*, *48*(25-26), 5386-5394.

Li, H.-Y., & Chen, K.-Y. (2007). Thermal performance of plate-fin heat sinks under confined impinging jet conditions. *International Journal of Heat and Mass Transfer*, *50*(9-10), 1963-1970.

Li, H.-Y., Chiang, M.-H., & Chen, K.-Y. (2007). Performance analysis of pin-fin heat sinks with confined impingement cooling. *IEEE transactions on components and packaging technologies*, *30*(3), 383-389.

Liang, T. S., & Hung, Y. M. (2010). Experimental investigation on the thermal performance and optimization of heat sink with U-shape heat pipes. *Energy Conversion and Management*, *51*(11), 2109-2116.

Lotfizadeh, H., Mehrizi, A. A., Motlagh, M. S., & Rezazadeh, S. (2015). Thermal performance of an innovative heat sink using metallic foams and aluminum nanoparticles—Experimental study. *International Communications in Heat and Mass Transfer*, *66*, 226-232.

Menter, F. (1993). Zonal two equation kw turbulence models for aerodynamic flows (p. 2906). Communication présentée au 23rd fluid dynamics, plasmadynamics, and lasers

conference.

Menter, F. R. (1994). Two-equation eddy-viscosity turbulence models for engineering applications. *AIAA journal*, *32*(8), 1598-1605.

Menter, F. R. (2009). Review of the shear-stress transport turbulence model experience from an industrial perspective. *International journal of computational fluid dynamics*, *23*(4), 305-316.

Menter, F. R., Kuntz, M., & Langtry, R. (2003). Ten years of industrial experience with the SST turbulence model. *Turbulence, heat and mass transfer*, *4*(1), 625-632.

Mohan, R., & Govindarajan, P. (2010). Thermal analysis of CPU with variable heat sink base plate thickness using CFD. *International journal of the computer, the internet and management*, *18*(1), 27-36.

Moshfegh, B., & Nyiredy, R. (2004). Comparing RANS models for flow and thermal analysis of pin fin heat sinks. Communication présentée au Proc. 15th Australasian Fluid Mechanics Conference, Citeseer.

Nichols, R. (2003). Applications of RANS/LES turbulence models (p. 83). Communication présentée au 41st Aerospace Sciences Meeting and Exhibit.

Phillips, R. J. (1988). Microchannel heat sinks. *The Lincoln Laboratory Journal*, *1*(1), 31-48.

Ping, P., Peng, R., Kong, D., Chen, G., & Wen, J. (2018). Investigation on thermal management performance of PCM-fin structure for Li-ion battery module in high-temperature environment. *Energy conversion and management*, *176*, 131-146.

Qu, W., Mala, G. M., & Li, D. (2000). Heat transfer for water flow in trapezoidal silicon microchannels. *International journal of heat and mass transfer*, *43*(21), 3925-3936.

Qu, W., & Mudawar, I. (2002). Experimental and numerical study of pressure drop and heat transfer in a single-phase micro-channel heat sink. *International journal of heat and mass transfer*, *45*(12), 2549-2565.

Reynolds, O. (1883). XXIX. An experimental investigation of the circumstances which determine whether the motion of water shall be direct or sinuous, and of the law of resistance in parallel channels. *Philosophical Transactions of the Royal society of London*, (174), 935-982.

Reynolds, O. (1895). IV. On the dynamical theory of incompressible viscous fluids and the determination of the criterion. *Philosophical transactions of the royal society of london.(a.)*, (186), 123-164.

Sahray, D., Shmueli, H., Ziskind, G., & Letan, R. (2010). Study and optimization of horizontal-base pin-fin heat sinks in natural convection and radiation.

Shaukatullah, H., Storr, W. R., Hansen, B. J., & Gaynes, M. A. (1996). Design and optimization of pin fin heat sinks for low velocity applications. *IEEE Transactions on Components, Packaging, and Manufacturing Technology: Part A*, *19*(4), 486-494.

Sikka, K. K., Torrance, K. E., Scholler, C., & Salanova, P. (2000). Heat sinks with fluted and wavy fins in natural and low-velocity forced convection (Vol. 1, pp. 149-156). Communication présentée au ITHERM 2000. The Seventh Intersociety Conference on Thermal and Thermomechanical Phenomena in Electronic Systems (Cat. No. 00CH37069), IEEE.

Spalart, P., & Allmaras, S. (1992). A one-equation turbulence model for aerodynamic flows (p. 439). Communication présentée au 30th aerospace sciences meeting and exhibit.

Sparrow, E., & Kadle, D. (1986). Effect of tip-to-shroud clearance on turbulent heat transfer from a shrouded, longitudinal fin array.

Taghilou, M., & Khavasi, E. (2020). Thermal behavior of a PCM filled heat sink: The contrast between ambient heat convection and heat thermal storage. *Applied Thermal Engineering*, *174*, 115273.

Takada, J., Kimura, Y., Ogushi, T., Fujii, M., Kohara, M., & Nakao, S. (1990). Development of a new air-cooling heatsink for a high density computer system (pp. 534-539). Communication présentée au 40th Conference Proceedings on Electronic Components and Technology, IEEE.

Thakar, S. S., Nambiar, S., Chandavarkar, G. A., & Prabu, S. S. (2021). Investigation of impingement cooling on a heat sink using CFD simulation. *Materials Today: Proceedings*, *46*, 8753-8760.

Turbulence Modeling Resource. (s.d.). Repéré à https://turbmodels.larc.nasa.gov/

Vasilev, M., Abiev, R. S., & Kumar, R. (2021). Effect of circular pin-fins geometry and their arrangement on heat transfer performance for laminar flow in microchannel heat sink. *International Journal of Thermal Sciences*, *170*, 107177.

Wang, F., Lai, C., Huang, Y., & Huang, J. (2013). Alternative layouts for air distribution improvement of a computing data center. *Advanced Materials Research*, *677*, 282-285.

Wang, X.-Q., Yap, C., & Mujumdar, A. S. (2008). A parametric study of phase change material (PCM)-based heat sinks. *International Journal of Thermal Sciences*, *47*(8), 1055-1068.

Wang, Y., & Ding, G. (2008). Experimental investigation of heat transfer performance for a novel microchannel heat sink. *Journal of micromechanics and microengineering*, *18*(3), 035021.

Wirtz, R. A., Chen, W., & Zhou, R. (1994). Effect of flow bypass on the performance of longitudinal fin heat sinks.

Xia, Y., Chen, L., Luo, J., & Tao, W. (2023). Numerical investigation of microchannel heat sinks with different inlets and outlets based on topology optimization. *Applied Energy*, *330*, 120335.

Xie, X., Liu, Z., He, Y., & Tao, W. (2009). Numerical study of laminar heat transfer and pressure drop characteristics in a water-cooled minichannel heat sink. *Applied thermal engineering*, *29*(1), 64-74.

Yin, H., Gao, X., Ding, J., & Zhang, Z. (2008). Experimental research on heat transfer mechanism of heat sink with composite phase change materials. *Energy Conversion and Management*, *49*(6), 1740-1746.

You, J.-H. (2015). Copper matrix composites as heat sink materials for water-cooled divertor target. *Nuclear Materials and Energy*, *5*, 7-18.

Yu, L.-T., & Chen, C.-K. (1999). Optimization of circular fins with variable thermal parameters. *Journal of the Franklin Institute*, *336*(1), 77-95.

Yu, X., Feng, J., Feng, Q., & Wang, Q. (2005). Development of a plate-pin fin heat sink and its performance comparisons with a plate fin heat sink. *Applied thermal engineering*, *25*(2-3), 173-182.

Zhang, G., Huang, H., Sun, T., Li, N., Zhou, B., & Sun, Z. (2019). Analysis of the performance of a new developed shear stress transport model in a turbulent impinging jet flow. *Physics of Fluids*, *31*(11).

Zhang, L., Goodson, K. E., & Kenny, T. W. (2004). *Silicon microchannel heat sinks: theories and phenomena*. (S.l.) : Springer Science & Business Media.

Zhou, F., & Catton, I. (2011). Numerical evaluation of flow and heat transfer in plate-pin fin heat sinks with various pin cross-sections. *Numerical Heat Transfer, Part A: Applications*, *60*(2), 107-128.